Understanding Ion Injection and Transport in Mixed Ionic/Electronic Conductors

Lucas Quinn Flagg

A dissertation

submitted in partial fulfillment of the

requirements for the degree of

Doctor of Philosophy

University of Washington

2019

Reading Committee:

David S. Ginger, Chair

Cody Schlenker

Dan Fu

Program Authorized to Offer Degree:

Chemistry

University of Washington

Abstract

Understanding Ion Injection and Transport in Mixed Ionic/Electronic Conductors

Lucas Quinn Flagg

Chair of the Supervisory Committee:
Professor David S. Ginger
Chemistry

Materials with the ability to conduct both ionic and electronic charge have found a number of new applications recently with real potential to change the world. Each of these applications has its own design requirements, however all of these rely on the ability of the polymer to conduct ions throughout the bulk of the film. In order to expand these capabilities, deeper understanding of what affects ion injection and transport is required. Specifically, the role of the electrolyte, polymer, and processing conditions all play a role. Here we specifically isolate these effects to develop a deeper understanding of what factors control ion injection and transport in conjugated polymer mixed electronic/ionic conductors. Specifically, we show that larger, more polarizable anions are able to enter hydrophobic polymers films at a lower potential, to a greater extent, and faster. Next, we investigate the role of the polymer side-chain and find that polar side chains enhance ion uptake. Additionally, we show the polymer morphology affects performance in different ways than it does in dry films, suggesting the need for new design rules. Finally, we

show in certain cases the charge compensation process is cation dependent as well. Together these studies help develop our understanding of ion injection into semiconducting polymers.

TABLE OF CONTENTS

LIST OF FIGURES

LIST OF TABLES

ACKNOWLEDGEMENTS

I would like to acknowledge Prof. David Ginger, Dr. Rajiv Giridharagopal, Dr. Connor Bischak, Jiajie Guo, Ramses Quezada, and all the other coworkers and collaborators I have had the opportunity to work with during my PhD.

Chapter 1. Introduction

1.1 MOTIVATION

Materials that are able to effectively transport both ionic and electronic charges have seen a recent resurgence of research interest for a broad array of applications of critical importance including biosensing[1,2] and energy storage.[3,4] Other applications that require materials that can conduct both ions and electrons include actuators,[5] light-emitting electrochemical cells,[6] bioelectronics,[7,8] ion pumps,[9,10] neuromorphic computing,[11–13] and organic electrochemical transistors.[14,15] Each of these diverse applications relies in some way on the coupling between ions and electrons within the active layer of the material. For the applications mentioned above, conjugated polymers specifically designed to allow facile ion injection have proven highly effective. It may not be immediately clear how the capacity of an all polymer super capacitor relates to the sensitivity of a polymer-based glucose sensor. However, the fundament processes of ion injection and transport within conjugated polymer govern both of these processes. Despite the recent progress, the factors that control the ion injection and transport, as well as ionic to electronic coupling remain understudied. Without universal rules that define how ions will interact with a material, each application space moves forward without the understanding informed by other similar devices. Here we seek to elucidate the fundamental factors that control ion injection in conjugated polymers. To do that, we choose to use the organic electrochemical transistor (OECT) as the template application that will allow us to draw conclusions relevant to all applications of mixed conductor.

1.2 THE ORGANIC ELECTROCHEMICAL TRANSISTOR

The structure of an OECT is shown in Figure 1.1A. In an OECT a mixed conductor connects the source and drain electrode and is in direct contact with an electrolyte. The gate electrode is also in contact with the electrolyte. Application of a bias at the gate, modulates the number of electronic carriers in the organic mixed conductor, thereby changing the conductivity of the channel and modulating the current between the source and drain electrodes. Typical characterization of an OECT is known as a transfer curve, shown in Figure 1.1B, where the current between the source and drain (I_D) is plotted as a function of the applied gate voltage (V_G). The slope of the transfer curve is known as the transconductance, g_m. This transconductance value can be described by the following equation:

$$g_m = \frac{Wd}{L} \mu C^* (V_{th} - V_G) \qquad \text{Eq 1.}$$

where W is the width of the channel, d is the thickness of the active layer, L is the length of the channel, μ is the electronic carrier mobility, C^* is the volumetric capacitance, and V_{th} is the threshold voltage.[16] It is worth noting that if the active layer does not allow ion transport the thickness of the active layer no longer matters and Equation 1 collapses to the two dimensional transconductance equation for field effect transistors. Inal et al. showed that the product μC^* is the materials figure of merit of OECT applications and allows for fair and repeatable comparisons between materials.[16] Although one OECT is enough to estimate the μC* product, by varying the dimensions and therefore $\frac{Wd}{L}$ researchers can fit a number of different transistors for more accurate determination of μC*. This procedure isolates the steady state product of the electronic carrier mobility and the volumetric capacitance of the material. Depending on the desired application, the kinetics of turning a device on/off can be of critical importance. Additionally, some applications

like energy storage require materials stable enough to be cycled thousands of times; whereas, stability is much less of a concern for a one-time-use biosensor.

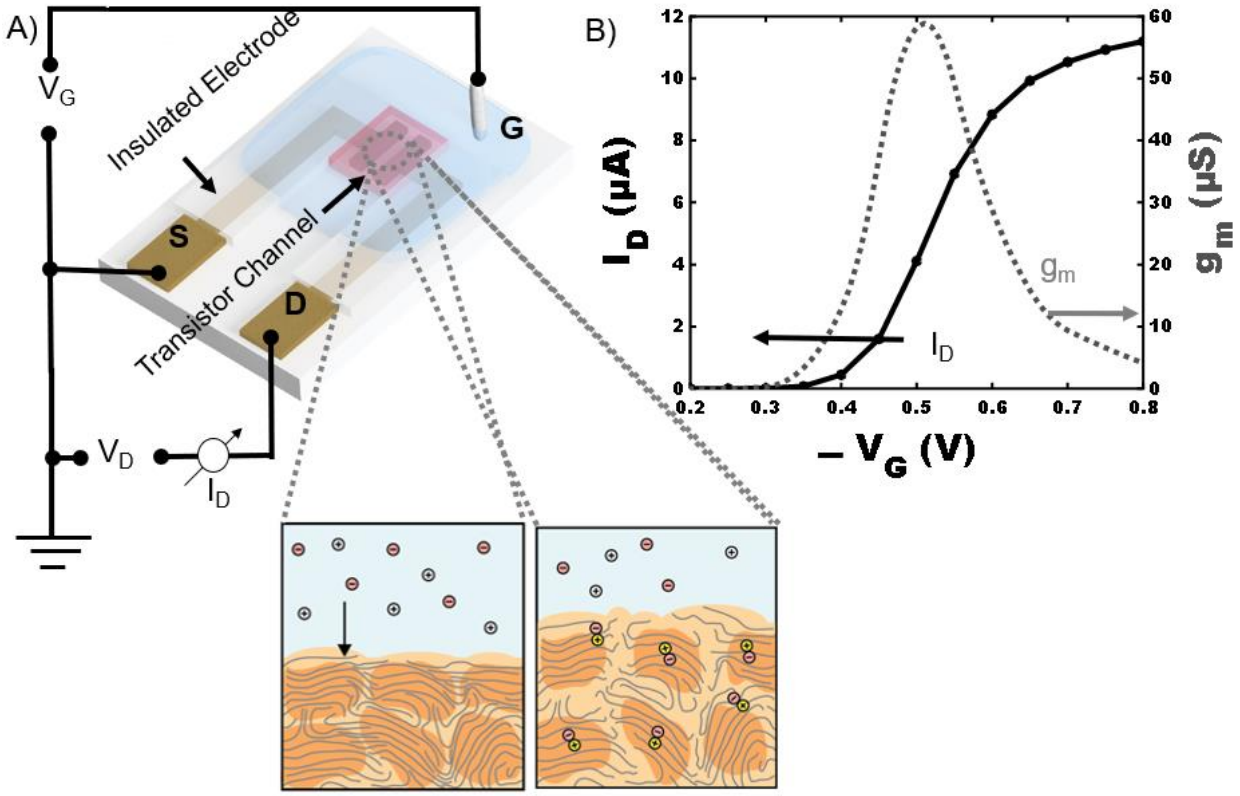

Figure 1.1 Schematic of an Organic Electrochemical Transistor A) Schematic of the device structure showing a source and drain electrode bridged by an organic mixed conductor in contact with an electrolyte. The left inset shows the "off" state where there are very few charge carriers in the active layer and the current between the source and drain is low. The right insert shows the "on" state where ions and hold are injected into the polymer creating a highly conductive active layer, which leads to high current between the source and drain electrode. B) Transfer curve of an OECT, where the current between the source and drain current is plotted against the applied gate voltage. The slope of the transfer curve is the transconductance, g_m.

In order to understand what makes organic electrochemical transistors so good for certain applications, we take a closer look at what the doping process in these materials looks like. In a conventional field effect transistor, the application of bias induces charges in the film. However,

since there is no mobile ionic species available this induced charge reaches a maximum at a the double layer capacitance of the device. By contrast, OECTs operate in contact with an electrolyte that contains mobile ions, as shown in Figure 1.2. The induced electronic charges in an OECT can be electronically compensated by an ion from solution resulting in a paired polaron (charge on the polymer backbone) and ion. This process allows the film to maintain charge neutrality during the charging process. At long times after the application of the gate bias, the number of ions and electronic charges with the film reaches steady state. In this steady state, the current between the source and drain electrode is dominated by electronic carriers flowing in the film.

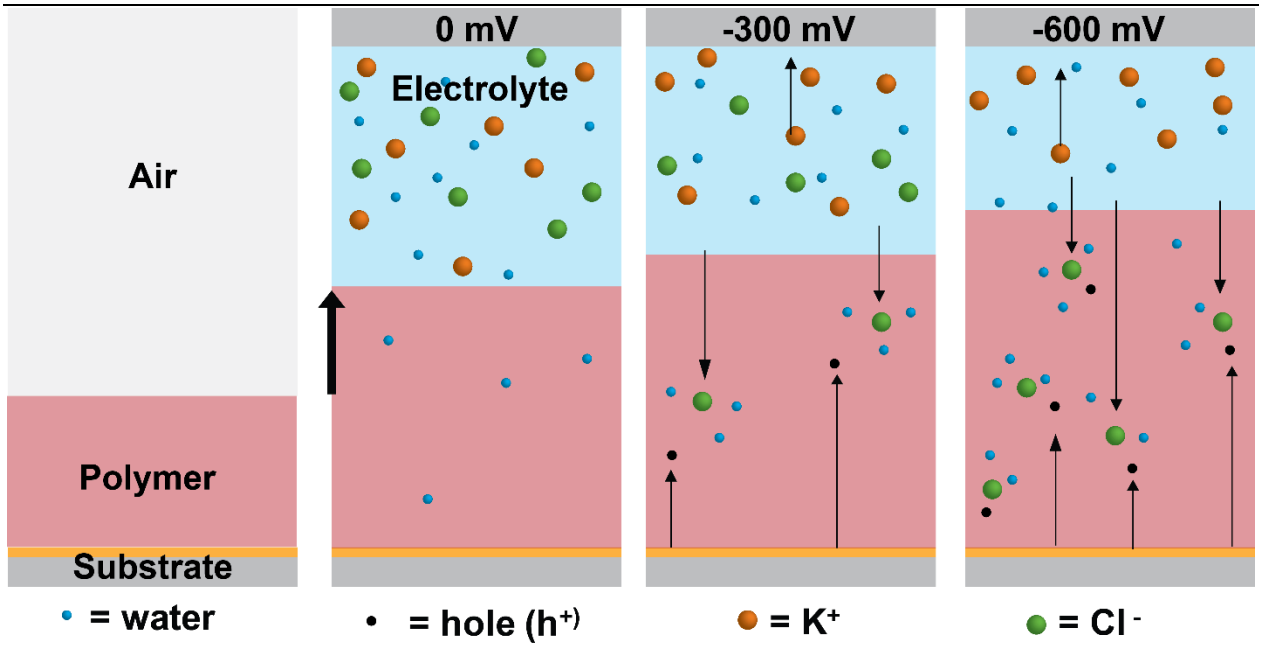

Figure 1.2 Schematic of Electrochemical Oxidation of a Mixed Conductor. In contact with electrolyte the polymer swells. Upon application of an oxidative bias, holes from the electrode are injected onto the polymer backbone. This charge is compensated by anions from solution in order maintain charge neutrality.

1.3 Ion Conducting Conjugated Polymers

Over the past 5 years there has been an explosion of the number of "good" mixed conductors reported. The general design strategy has been to use polymer backbones that have demonstrated good electronic carrier mobility in field effect transistors (FETs). Most FET polymers have alkyl side chains, which make the polymer hydrophobic and tends to disrupt ion transport. Substituting this alkyl side-chain for a more hydrophilic side-chain has proven widely successful. On nearly every polymer backbone reported so far the use of oligoethylene glycol side chains results in dramatically improved ion transport including polythiophene,[17] benzodithiophene,[18] propylenedioxythiophene,[19] bithiophene-thioenothiophene,[20] naphthalene tetracarboxylic diimide.[21,22] We illustrate two model polymers in Figure 1.3, the alkyl side-chain poly(3-hexylthiophene-2,5-diyl) (P3HT) and its glycol side-chain analogue poly(3-{[2-(2-methoxyethoxy)ethoxy]methyl}thiophene-2,5-diyl) (P3MEEMT). Other polar side chains have also been demonstrated to improve the ion transport properties of conjugated polymer including alcohols,[23] carboxylic acids,[24] amides,[25] and sulfonates.[26–28] Despite a wealth of new mixed conductors reported, the fundamental understanding of what controls ion injection and transport within this fascinating class of materials is understudied. A better understanding of the fundamental factors that control the ion injection and transport in these materials would help guide further rational synthetic design of mixed conductors.

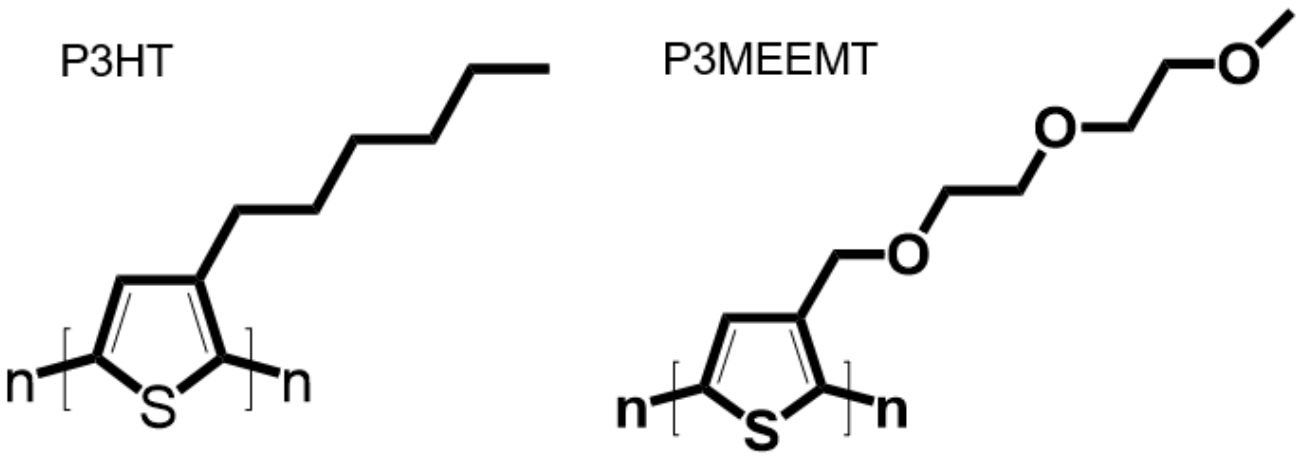

Figure 1.3 Polymer Structures Used. P3HT is a model conjugated polymer frequently used for electronic applications. P3MEEMT is a newly synthesized analogue of P3HT with an oligoethylene glycol side chain to promote ionic conduction.

1.4 SUMMARY

This dissertation describes three studies which seek to further understand the processes involved in the electrochemical doping of organic mixed ionic electronic conductors. In each case, we isolate the effect of one component of the system to gain insight into how different factors affect the system. Through this work, we develop an understanding where electrochemical doping of this class of materials depends the complex interplay of many factor including the electrolyte anion, the polymer side-chain, the polymer microstructure, and the electrolyte cation.

First, we investigate the role of the anion in the electrochemical doping of organic mixed conductors. We show that large, polarizable anions are able to enter polymer films much more easily than small, non-polarizable anions. Using OECTs, spectroelectrochemistry, and quartz crystal microbalance gravimetry we show that larger ions inject into P3HT films at a lower voltage.

Additionally, we show that even after accounting for the difference in injection voltage, larger ions inject into P3HT films faster than small anions. We show that the difference in ease of injection (both lower potentials, and faster) can be explained by the solvation of the ions. Large ions enter the film free (or nearly free) of waters. However, a small ion like chloride drags upwards of 10 waters into the film with it. We hypothesize that the inclusion of waters could explain the ion dependence of the electronic carrier mobility that we observe. Finally, we show that electrochemical strain microscopy is sensitive to the number of ions energy that enter the film at a certain bias.

Next, we investigate the anion dependence in a better ionic conductor. Again, we find that larger anions inject at a lower bias. However, the differences in kinetics are drastically reduced in P3MEEMT compared to P3HT. We use X-ray diffraction to show that this is due to swelling upon exposure to electrolyte. In P3MEEMT, which has ethylene glycol side chains, exposure to electrolyte results in an expansion in the lamellar stacking direction. Electrochemical oxidation (injection of ions) does not require further expansion. By contrast, in P3HT, exposure to electrolyte does not expand the crystal structure. Upon electrochemical oxidation, the lattice expands in the lamellar direction. We believe this difference in the inclusion of the electrolyte can explain the difference in the kinetics between the two polymers and the reduced anion dependence in P3MEEMT. Additionally, we investigate how the polymer microstructure affects OECT performance in P3MMET. Thermal annealing improves the dry transistor performance as expected; however, the annealed polymer performs worse than the unannealed film as an OECT. Since the presence of electrolyte is the difference between these two cases, we use profilometry and electrochemical quartz crystal microbalance gravimetry to investigate the swelling of these two systems. In the unannealed case we find dramatic swelling upon exposure to electrolyte and

significant water expulsion upon electrochemical doping. Annealing minimizes both the initial swelling and the need for water expulsion. To understand this further we use photoinduced force microscopy (PiFM) to image where ion uptake occurs and show that annealing the film leads to dramatic heterogeneity in ion uptake.

Lastly, we examine the role of the cation in the charge compensation that occurs during electrochemical doping of P3MMET. We find that when the anion is large, the cation plays a dramatic role in the charge compensation. In the specific case of oxidation in KPF_6, we show direct evidence for charge compensation occurring by cation expulsion first, followed by the conventional anion injection mechanism at higher doping levels. This serves as an important reminder that the cation is not just a bystander but can be actively involved in the doping process under certain conditions.

1.5 REFERENCES

(1) Stavrinidou, E.; Leleux, P.; Rajaona, H.; Khodagholy, D.; Rivnay, J.; Lindau, M.; Sanaur, S.; Malliaras, G. G. Direct Measurement of Ion Mobility in a Conducting Polymer. *Adv. Mater.* **2013**, *25*, 4488–4493. https://doi.org/10.1002/adma.201301240.

(2) Pappa, A.-M. M.; Ohayon, D.; Giovannitti, A.; Maria, I. P.; Savva, A.; Uguz, I.; Rivnay, J.; McCulloch, I.; Owens, R. M. R.; Inal, S. Direct Metabolite Detection with an N-Type Accumulation Mode Organic Electrochemical Transistor. *Sci. Adv.* **2018**, *4*, eaat0911. https://doi.org/10.1126/sciadv.aat0911.

(3) Moia, D.; Giovannitti, A.; Szumska, A. A.; Maria, I. P.; Rezasoltani, E.; Sachs, M.; Schnurr, M.; Barnes, P. R. F.; McCulloch, I.; Nelson, J. Design and Evaluation of Conjugated Polymers with Polar Side Chains as Electrode Materials for Electrochemical Energy Storage in Aqueous Electrolytes. *Energy Environ. Sci.* **2019**, *12* (4), 1349–1357. https://doi.org/10.1039/c8ee03518k.

(4) Volkov, A. V.; Sun, H.; Kroon, R.; Ruoko, T.-P.; Che, C.; Edberg, J.; Müller, C.; Fabiano, S.; Crispin, X. Asymmetric Aqueous Supercapacitor Based on P- and n-Type Conducting Polymers. *ACS Appl. Energy Mater.* **2019**. https://doi.org/10.1021/acsaem.9b00853.

(5) Smela, E.; Gadegaard, N. Volume Change in Polypyrrole Studied by Atomic Force Microscopy. *J. Phys. Chem. B* **2001**, *105*, 9395–9405. https://doi.org/10.1021/jp004126u.

(6) Tang, S.; Sandström, A.; Lundberg, P.; Lanz, T.; Larsen, C.; Van Reenen, S.; Kemerink, M.; Edman, L. Design Rules for Light-Emitting Electrochemical Cells Delivering Bright Luminance at 27.5 Percent External Quantum Efficiency. *Nat. Commun.* **2017**, *8* (1). https://doi.org/10.1038/s41467-017-01339-0.

(7) Bai, L.; Elósegui, C. G.; Li, W.; Yu, P.; Fei, J.; Mao, L. Biological Applications of Organic Electrochemical Transistors: Electrochemical Biosensors and Electrophysiology Recording. *Front. Chem.* **2019**, *7* (May), 1–16. https://doi.org/10.3389/fchem.2019.00313.

(8) Uguz, I.; Ganji, M.; Hama, A.; Tanaka, A.; Inal, S.; Youssef, A.; Owens, R. M.; Quilichini, P. P.; Ghestem, A.; Bernard, C.; et al. Autoclave Sterilization of PEDOT:PSS Electrophysiology Devices. *Adv. Healthc. Mater.* **2016**, *5* (24), 3094–3098. https://doi.org/10.1002/adhm.201600870.

(9) Isaksson, J.; Kjäll, P.; Nilsson, D.; Robinson, N.; Berggren, M.; Richter-Dahlfors, A. Electronic Control of Ca^{2+} Signalling in Neuronal Cells Using an Organic Electronic Ion Pump. *Nat. Mater.* **2007**, *6*, 673–679. https://doi.org/10.1038/nmat1963.

(10) Proctor, C. M.; Uguz, I.; Slezia, A.; Curto, V.; Inal, S.; Williamson, A.; Malliaras, G. G. An Electrocorticography Device with an Integrated Microfluidic Ion Pump for Simultaneous Neural Recording and Electrophoretic Drug Delivery In Vivo. **2018**, *1800270*, 1–6. https://doi.org/10.1002/adbi.201800270.

(11) Gkoupidenis, P.; Koutsouras, D. A.; Malliaras, G. G. Neuromorphic Device Architectures with Global Connectivity through Electrolyte Gating. *Nat. Commun.* **2017**, *8* (May), 1–8.

https://doi.org/10.1038/ncomms15448.

(12) Burgt, Y. van de; Lubberman, E.; Fuller, E. J.; Keene, S. T.; Faria, G. C.; Agarwal, S.; Marinella, M. J.; Talin, A. A.; Salleo, A. A Non-Volatile Organic Electrochemical Device as a Low-Voltage Artificial Synapse for Neuromorphic Computing. *Nat. Mater.* **2017**, *16*, 414–419. https://doi.org/10.1038/nmat4856.

(13) Keene, S. T.; Melianas, A.; Burgt, Y. Van De; Salleo, A. Mechanisms for Enhanced State Retention and Stability in Redox-Gated Organic Neuromorphic Devices. **2018**, *1800686*, 1–10. https://doi.org/10.1002/aelm.201800686.

(14) Zeglio, E.; Inganäs, O. Active Materials for Organic Electrochemical Transistors. *Adv. Mater.* **2018**, *30* (44), 1–18. https://doi.org/10.1002/adma.201800941.

(15) Moser, M.; Ponder, J. F.; Wadsworth, A.; Giovannitti, A.; McCulloch, I. Materials in Organic Electrochemical Transistors for Bioelectronic Applications: Past, Present, and Future. *Adv. Funct. Mater.* **2018**, *1807033*, 1807033. https://doi.org/10.1002/adfm.201807033.

(16) Inal, S.; Malliaras, G. G.; Rivnay, J. Benchmarking Organic Mixed Conductors for Transistors. *Nat. Commun.* **2017**, *8*, 1767. https://doi.org/10.1038/s41467-017-01812-w.

(17) Nielsen, C. B.; Giovannitti, A.; Sbircea, D. T.; Bandiello, E.; Niazi, M. R.; Hanifi, D. A.; Sessolo, M.; Amassian, A.; Malliaras, G. G.; Rivnay, J.; et al. Molecular Design of Semiconducting Polymers for High-Performance Organic Electrochemical Transistors. *J. Am. Chem. Soc.* **2016**, *138*, 10252–10259. https://doi.org/10.1021/jacs.6b05280.

(18) Giovannitti, A.; Thorley, K. J.; Nielsen, C. B.; Li, J.; Donahue, M. J.; Malliaras, G. G.; Rivnay, J.; McCulloch, I. Redox-Stability of Alkoxy-BDT Copolymers and Their Use for Organic Bioelectronic Devices. *Adv. Funct. Mater.* **2018**, *28*, 1706325. https://doi.org/10.1002/adfm.201706325.

(19) Savagian, L. R.; Österholm, A. M.; Ponder, J. F.; Barth, K. J.; Rivnay, J.; Reynolds, J. R. Balancing Charge Storage and Mobility in an Oligo(Ether) Functionalized Dioxythiophene Copolymer for Organic- and Aqueous- Based Electrochemical Devices and Transistors. *Adv. Mater.* **2018**, *30*, 1804647. https://doi.org/10.1002/adma.201804647.

(20) Giovannitti, A.; Sbircea, D.-T.; Inal, S.; Nielsen, C. B.; Bandiello, E.; Hanifi, D. A.; Sessolo, M.; Malliaras, G. G.; McCulloch, I.; Rivnay, J. Controlling the Mode of Operation of Organic Transistors through Side-Chain Engineering. *Proc. Natl. Acad. Sci.* **2016**, *113*, 12017–12022. https://doi.org/10.1073/pnas.1608780113.

(21) Giovannitti, A.; Nielsen, C. B.; Sbircea, D.-T.; Inal, S.; Donahue, M.; Niazi, M. R.; Hanifi, D. A.; Amassian, A.; Malliaras, G. G.; Rivnay, J.; et al. Erratum: N-Type Organic Electrochemical Transistors with Stability in Water. *Nat. Commun.* **2016**, *7*, 13955. https://doi.org/10.1038/ncomms13955.

(22) Giovannitti, A.; Maria, I. P.; Hanifi, D.; Donahue, M. J.; Bryant, D.; Barth, K. J.; Makdah, B. E.; Savva, A.; Moia, D.; Zetek, M.; et al. Role of the Side Chain on the Performance of N-Type Conjugated Polymers in Aqueous Electrolytes. *Chem. Mater.* **2018**, *30*, 2945–2953. https://doi.org/10.1021/acs.chemmater.8b00321.

(23) Pacheco-Moreno, C. M.; Schreck, M.; Scaccabarozzi, A. D.; Bourgun, P.; Wantz, G.; Stevens, M. M.; Dautel, O. J.; Stingelin, N. The Importance of Materials Design to Make Ions Flow: Toward Novel Materials Platforms for Bioelectronics Applications. *Adv. Mater.* **2017**, *29*, 1604446. https://doi.org/10.1002/adma.201604446.

(24) Khau, B. V; Savagian, L. R.; Keersmaecker, M. De; Gonzalez, M. A.; Reichmanis, E. Carboxylic Acid Functionalization Yields Solvent-Resistant Organic Electrochemical Transistors. **2019**. https://doi.org/10.1021/acsmaterialslett.9b00373.

(25) Koltzenburg, S.; Maskos, M.; Nuyken, O. Conjugated Electrochromic Polymers with Amide-Containing Side Chains Enabling Aqueous Electrolyte Compatibility. *Polym. Chem.* **2019**, 1–584. https://doi.org/10.1007/978-3-662-49279-6.

(26) Zeglio, E.; Eriksson, J.; Gabrielsson, R.; Solin, N.; Inganäs, O. Highly Stable Conjugated Polyelectrolytes for Water-Based Hybrid Mode Electrochemical Transistors. *Adv. Mater.* **2017**, *29* (19), 6–11. https://doi.org/10.1002/adma.201605787.

(27) Schmode, P.; Ohayon, D.; Reichstein, P. M.; Savva, A.; Inal, S.; Thelakkat, M. High-Performance Organic Electrochemical Transistors Based on Conjugated Polyelectrolyte Copolymers. *Chem. Mater.* **2019**, *31* (14), 5286–5295. https://doi.org/10.1021/acs.chemmater.9b01722.

(28) Inal, S.; Rivnay, J.; Leleux, P.; Ferro, M.; Ramuz, M.; Brendel, J. C.; Schmidt, M. M.; Thelakkat, M.; Malliaras, G. G. A High Transconductance Accumulation Mode Electrochemical Transistor. *Adv. Mater.* **2014**, *26*, 7450–7455. https://doi.org/10.1002/adma.201403150.

Chapter 2. Anion-Dependent Doping and Charge Transport in Organic Electrochemical Transistors[1]

2.1 INTRODUCTION

Electrochemical doping of conjugated polymers has numerous applications in technologies ranging from supercapacitors,[1–3] to batteries,[4] neuromorphic computers,[5] ion pumps,[6,7] actuators,[8] and high-performance biochemical sensors[9,10] for transduction of signals across the biological/digital divide. Each of these applications makes use of the flexible nature of the polymer to allow some degree of ion permeation into the semiconductor, and therefore achieve more intimate coupling between ionic and electronic charge carriers than can be achieved in inorganic materials.[11–13] As such, understanding the materials properties that control ion injection from electrolytes into organic semiconductors is a fundamental question that has the potential to affect the design and performance of these materials in a broad range of applications.

Electrochemical doping of conjugated polymer materials has been studied in a variety of contexts.[14] Historically, much early interest in doping conjugated polymers was in tuning the conductivity of the polymer from highly insulating to nearly metallic.[15,16] In this context, the polymer was doped to a certain level/conductivity at the outset and then studied or used further in that state. However, many modern applications of doped conjugated polymers take advantage of the reversibility of doping/dedoping processes in these materials. When in contact with an electrolyte, conjugated polymers will accept electronic carriers, and counterions from solution will move into the polymer matrix to electronically compensate this charge. This process is often

[1] Reproduced with permission from Flagg, L. Q.; Giridharagopal, R.; Guo, J.; Ginger, D. S. Anion-Dependent Doping and Charge Transport in Organic Electrochemical Transistors. *Chem. Mater.* **2018**, *30*, 5380–5389. Copyright 2018 American Chemical Society.

informally called doping,[17] though it is more formally electrochemical oxidation and reduction of the material accompanied by ionic charge compensation.

In the field of polymer actuators in particular, the role of the compensating ion has been studied,[18,19] mainly with the goal of optimizing the volume expansion of the film. On the other hand, the role of the counterion in electronic transport devices (e.g. OECTs) is much less studied. Many other aspects of OECT design have been shown to affect device performance including active layer thickness,[20] threshold voltage,[21] polymer side chains,[22,23] and even the counter-ion used during polymer synthesis,[24] but the nature of the dopant ion itself has been less explored. In fact, electrolyte identity is not even included among "standard" reporting metrics for these devices.[25]

In mixed electronic/ionic conduction applications, we might expect the role of the dopant ion to be important in light of the current understanding of the materials design tradeoff between electronic and ionic transport, with electronic conduction occurring predominantly in more-ordered regions and ionic conduction in more-disordered regions.[26,27] Furthermore, recent research shows that doping alters the π-π stacking distance in polymers like P3HT and therefore the electronic properties.[28–30] For OECTs specifically, this effect is especially pertinent. In many sensing geometries the dopant is the sensing or transduction target and specific chemical interactions have the potential to change the sensitivity, accuracy, and operating frequency the transistor can achieve. Here, we study the role of dopant ions in mixed ionic/electronic conduction applications of organic semiconductors using P3HT-based OECTs as a model testbed. In addition to being an important technology in their own right, OECTs enable facile measurements of electronic transport properties, and can be characterized via electronic, spectroscopic, and electrogravimetric measurements to obtain complementary information about doping levels and

ion uptake.

Herein we focus on the model organic semiconductor poly(3-hexylthiophene-2,5-diyl) (P3HT). Although P3HT is less widely used than PEDOT:PSS in OECT applications, the thiophene backbone is ubiquitous in current high performance materials,[31–33] and therefore remains an important model system for understanding OECT physics. Additionally, P3HT is perhaps the most common model for polymer transport measurements, and electrochemical doping studies of P3HT have a long history.[34–36] Furthermore, as an accumulation mode hole-transporting material, P3HT remains the active layer of choice for some applications.[37,38] We characterize P3HT OECTs in a variety of electrolytes to investigate the role of the dopant ion identity. We use spectroelectrochemistry to measure the doping level of the polymer in each electrolyte, and we measure ion-dependent OECT parameters such as transconductance and switching rates, as well as carrier mobility, as a function of potential and doping level. We study the ion uptake process by

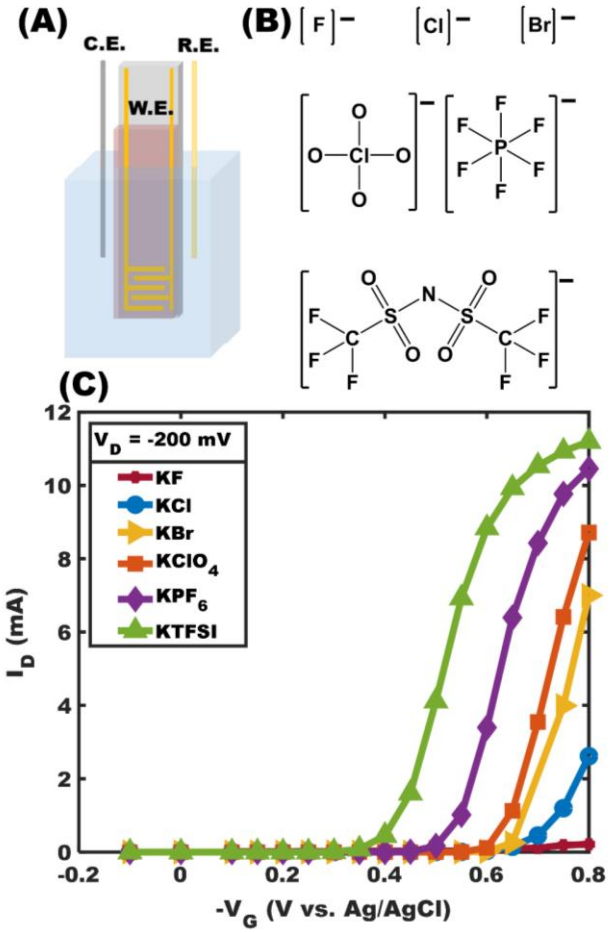

Figure 2.1 Measurement of P3HT electrochemical transistors. (A) Device geometry for OECT testing, with a platinum counter electrode (C.E.) and an Ag/AgCl reference electrode (R.E.) (B) Chemical structures of the anions of the potassium salts (left to right fluoride, chloride, bromide, perchlorate, hexafluorophosphate, bis(trifluoromethanesulfonyl)imide) used in this study (C) Characteristic transfer curves (V_D = -200 mV) with 6 different electrolytes showing increased transistor current for bulkier anions.

electrogravimetric measurements to understand the solvation of the ion within the polymer. Finally, we study the nanoscale structure-function relationship underpinning these responses by Electrochemical Strain Microscopy (ESM).

2.2 RESULTS

Transistor Characterization. Figure 2.1 A shows a schematic of the device geometry we use to study the effects of anion type on OECT performance. Briefly, we use a conventional 3-electrode electrochemical cell with a platinum counter electrode (C.E.), Ag/AgCl reference electrode (R.E.), and the polymer-coated gold interdigitated electrodes as the working electrode (W.E.). The gate bias/current is applied/recorded by the potentiostat, and the transistor source drain bias/current is applied/recorded across the pair of interdigitated electrodes by a separate source meter. Figure 2.1 B shows the structures of the anions of the potassium salts used in this study. The chemical structures show the difference in size, shape, and chemical composition of the anions studied. Anion properties such as ionic radius and polarizability, which dramatically effect hydration, are outlined in Table A.1. Figure 2.1 C shows the source drain current (I_D) of an OECT as a function of gate bias for the 6 different electrolytes at a scan rate of 0.01 Hz. The performance of the P3HT OECT clearly depends heavily on the anion in the electrolyte. The maximum source-drain current (I_D) within the bias window (V_G from +0.4 V to -0.8 V) varies with anion in the following order from least to greatest: KF, KCl, KBr, $KClO_4$, KPF_6, and KTFSI. Additional characterization of the transistors is shown in Figure A.1 and Figure A.2. Importantly, in addition to the magnitude of the drain current varying with anion type, the threshold voltage also shifts. Figure 2.1 C shows the threshold voltage from least negative to most negative is KTFSI, KPF_6, $KClO_4$, KBr, KCl, KF. We confirmed that the potential relative to Ag/AgCl is not drifting by oxidation of ferrocene (Figure A.4), meaning these shifts are indeed shifts in the threshold voltage, not drifts in the reference.

Next, we explore the origins of these ion-dependent behaviors. The source-drain current in an OECT is given by the following equation:

$$I_D = \frac{W\,t}{L}\, V_D\, \mu\, Q \qquad (1)$$

where I_D is the transistor current, W is the device width in cm, t is the film thickness in cm, L is the device length in cm, V_D is the source drain voltage in volts, μ is the average carrier mobility in the channel in $cm^2\ V^{-1}\ s^{-1}$, and Q is the average charge density in the channel in C cm^{-3}.[43] Since the geometry of the device (*W, L, t*) is not changing with electrolyte, and the source drain bias is held constant (at -200 mV) for the measurements in Figure 2.1 C, the differences in measured current must originate from a difference in either carrier density (Q), carrier mobility (μ), or both.

Spectroelectrochemistry. In order to isolate the effects of carrier (doping) density from mobility, we determine doping level self-consistently using two separate approaches: first by spectroelectrochemistry and second by coulometry. To determine carrier density via spectroelectrochemistry we make use of the fact that, when oxidized, P3HT exhibits a different

spectra than its reduced state: the absorption at the undoped polymer maximum (522 nm) decreases and absorption increases in the subband gap region (See Figure A.5 C).[44] Figure 2.2 A shows the fraction of absorption at 552 nm that is bleached as a function of gate bias for each of 6 potassium electrolytes. The bleaching is completely reversible under the conditions employed (gate biases +0.5 to -0.8 V vs. Ag/AgCl, see Figure A.6). At the highest gate bias (-0.8 V) in KTFSI solution, nearly 60% of the absorption at the neutral polymer peak is lost. The bleach magnitude as a function of electrolyte, from greatest to least, is KTFSI, KPF_6, $KClO_4$, KBr, KCl, KF, which follows the same order as the transistor current shown in Figure 2.1 C, indicating that at least some of the variation in transistor current with anion is due to the differences in injected charge density with different anions. Additionally, the gate bias where the absorption bleach begins changes with the electrolyte from lowest to highest voltage in the order: KTFSI, KPF_6, KBr,

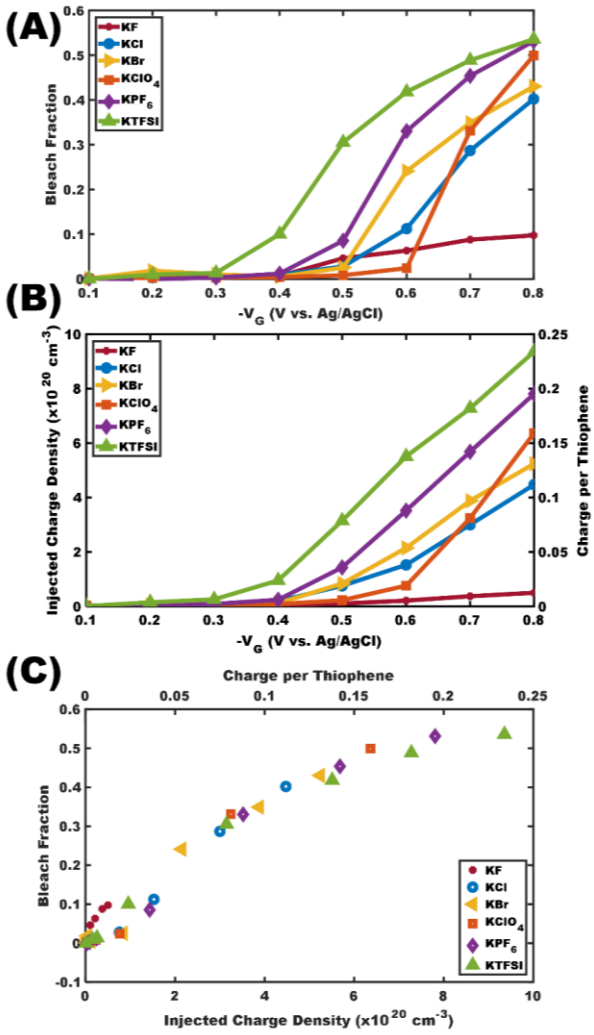

Figure 2.2 Doping level (A) Fraction of absorption at 552 nm bleached by electrochemical doping in 20 mM electrolyte as a function of gate bias for 6 different electrolytes showing anion dependent bleaching. (B) Doping density as determined by coulometry as a function of gate bias for 6 different electrolyte showing anion dependent carrier density in the film. (C) Absorption bleach verses doping density showing agreement between 2 different methods of measuring carrier density.

KCl, KF, $KClO_4$. Notably, this is similar to the ordering of the threshold voltage. We thus interpret the variation in transistor threshold voltage with counterion as reflecting the different potential required to inject ion/carrier pairs into the film.

In addition to spectroelectrochemistry, we also use coulometry to cross-check the measured doping levels in our OECTs.[39] To do so, we determine the charges consumed in the oxidation/reduction of the polymer by integrating the total gate current during the spectroelectrochemistry experiment, using a 3-electrode electrochemical cell (platinum counter electrode, Ag/AgCl reference electrode, polymer/FTO working electrode, see Figure A.5A). We calculate the steady-state carrier concentration at each gate bias for each electrolyte. Figure 2.2 B plots the results as injected carrier density versus gate bias for each of the 6 anions. These doping densities assume uniform doping profile, which is consistent with the extremely slow scan rates used herein. Both the carrier density maximum and the carrier injection onset measured by this method follow the same trend as the spectroelectrochemistry data, increasing our confidence in the determination of the doping density and trends. The comparison of these 2 methods for monitoring doping is shown in Figure 2.2 C, where the magnitude of the absorption bleach is plotted against the gate bias-induced doping density for each electrolyte. Figure 2.2 C shows that, at lower doping, the absorption bleach changes linearly with number of electronic carriers injected. At higher doping levels, the creation of bipolarons leads to deviations from the linear relationship between consumed charge and absorption at 552 nm (See Figure A.8). Thus far, we have shown that the dopant density is dependent on the chemistry of the compensating anion and conclude that charge carrier/ion injection differences are largely responsible for the differences in OECT device operation.

Mobility. However, as mentioned earlier, the difference in charge transport characteristics of OECT devices could originate from a change in carrier density, carrier mobility, or both. Since we have self-consistent measurements of the injected carrier density using both spectroelectrochemistry and coulometry, we can thus look for the effects of an anion-dependent mobility on device performance. Figure 2.3 plots the carrier mobility calculated from Eqn. 1 (using Q determined in Figure 2.2 B) as a function of carrier density for 4 different potassium electrolytes with different anions. Qualitatively, we see a very similar dependence of mobility on doping level due to electrochemical doping P3HT as previously reported in the literature,[45–47] with an initial decrease in mobility at low carrier density, followed by a sharp increase in mobility at medium doping levels, and finally a saturation at the highest doping levels. In our films the mobility curves converge and saturate near ~ 10^{-2} cm^2 V^{-1} s^{-1} which is ~10X lower than the peak mobilities reported for regioregular P3HT in thin-film transistors;[46,48] we attribute this to our use of unannealed films along with a possible difference in the regioregularity of our polymer. This saturation occurs at ~4 x 10^{20} holes cm^{-3}, in excellent agreement with previous theoretical and experimental studies of P3HT.[48–51] Figure 2.3 shows that the *onset* of the steep increase in mobility is counter ion dependent, occurring at 0.003 charges per thiophene for $KClO_4$, 0.01 charges per thiophene for KCl and KTFSI, and 0.02 charges per thiophene for KPF_6. Models of carrier

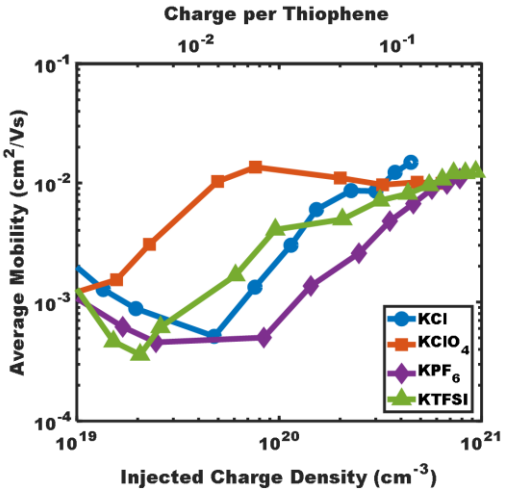

Figure 2.3 Mobility Average mobility as a function of doping density for P3HT films electrochemically doped in 4 different potassium salts. Mobility steeply increases with doping density until saturating around ~3 x 10^{-2} cm^2 V^{-1} s^{-1}.

mobility in electrochemically doped disordered organic semiconductors have attributed the region of steep increase in mobility to the overlap of neighboring Coulomb traps (which lowers the energy barrier between them, reducing the energetic disorder),[52] or to an increasing density of accessible hopping states with increased carrier density.[51,53]

Interpreting our data in the context of the Bässler model[52] would thus imply the size of the coulomb trap induced by the dopant is anion-dependent, and largest for ClO_4^- (traps begin overlapping at the lowest doping density) and smallest for PF_6^- (doping density is highest before traps begin overlapping). We further investigate this trend in Table A.2. On the other hand, interpreting our data in the context of the state-filling-model would suggest the shape of the density of states is altered by anion uptake, perhaps due to structural distortions associated with the anion size. Regardless of the cause, the data indicate that the choice of dopant anion can have a dramatic effect on electronic carrier mobility, particularly at low doping levels. We note that, while this difference at low doping levels might be particularly sensitive to intrinsic doping or charge levels in the polymer, the trend in mobility was reproduced across many devices tested with different anions in random order, suggesting the anion itself is responsible for the effect. Additionally, we point out that the trend seen in mobility rise with doping level differs from the trend seen in the threshold voltage shifts. Although we suspect hydration plays a role in both effects, these are two different processes. We hypothesize that the threshold voltage shift is related to the energy involved in injecting a dopant from the electrolyte into the film, whereas the onset of mobility increase can be attributed to influence of the dopant (and associated hydration shell) on the energetic landscape for carriers within the polymer itself.

Electrogravimetry. Having shown that both the doping density and carrier mobility vary with anion, we further investigate the electrochemical doping process using gravimetric measurements

made *in situ* with an electrochemical quartz crystal microbalance (EQCM). We apply an oxidative/reductive bias using the P3HT-coated gold pad on a QCM crystal as the working electrode in a 3 electrode cell and monitor the frequency of the crystal oscillation in time. Under bias, ions from the electrolyte move into/out of the film, changing the mass of the film which changes the resonance frequency of the circuit.[54] Using the Sauerbrey equation[55] and Faraday's law we quantitatively interpret our EQCM data with the following equation:[56]

$$\Delta f = \frac{M_w C_f Q}{n F A} \qquad (2)$$

where Δf is the frequency change in Hz , M_w is the molar mass of the dopant species in g mol^{-1}, C_f is the sensitivity factor in Hz cm^2 g^{-1} (see Figure A.9 for calibration[57]), Q is the charge consumed during the reduction/oxidation in C, n is the number of electrons transferred to induce doping (assuming n=1 in this work), F is Faraday's constant (96,485 C mol^{-1}) , and A is the area of the liquid contact electrode in cm^2. Figure A.10 shows the frequency over time of the polymer coated QCM crystal in response to a gate bias step in 4 different potassium electrolytes. In KTFSI, a gate bias of -0.8 V results in a frequency decrease of 465 Hz, but in KCl the frequency only decreases 87 Hz. Using the change in frequency in response to each gate bias step and the previously determined dopant density we calculate the apparent molar mass of the counterion entering the polymer film. The results of this analysis are shown in Table 2.1: the apparent mass of the counterion species in KCl electrolyte is 225 g/mol, 326 g/mol for $KClO_4$, 182 g/mol for KPF_6, and 218 g/mol for KTFSI. For

Anion Molecular Weight [g/mol]	Apparent mass [g/mol] potential step method (anion + n solvent)	Apparent mass [g/mol] cyclic voltammetry (anion + n solvent)
Cl^- (35.45)	225 (10.5)	217 (10.1)
ClO_4^- (99.45)	326 (12.8)	316 (12.0)
PF_6^- (144.96)	182 (2.1)	195 (2.8)
$TFSI^-$ (208.15)	218 (0.5)	223 (0.8)

Table 2.1. Apparent dopant mass during oxidation of P3HT films in various potassium electrolytes

the two smaller anions, less polarizable (Cl^- and ClO_4^-) we observe an apparent molar mass of the dopant significantly greater than the molar mass of the anhydrous anion, consistent with the ion moving into the film along with a hydration shell of ~10-13 waters during the oxidation process, consistent with previously reported doping of conjugated polymers by halide anions.[56,58] However for the large, highly polarizable anions (PF_6^- and $TFSI^-$), we measure an apparent mass that is close to the mass of the bare anion, suggesting the ion moves into the film only slightly solvated, if it is solvated at all. To confirm this finding we also performed simultaneous cyclic voltammetry and electrogravimetric measurements to determine the molar mass of the dopant as previously described in the literature.[40–42] Briefly, the change in mass is plotted against the charge consumed (integrated from the current), and the slope of the resulting plot yields the counterion mass (See Figure A.11). The results of this experiment are also summarized in Table 2.1 and yield very similar (+/- 13 g mol^{-1}) results to the potential step method of determining dopant mass. The agreement between these techniques increases our confidence in the solvation conclusions, as well as our determination of dopant density by potential steps. Determinations of counterion mass are vulnerable to artifacts due to breakdowns in permselectivity and reversibility,[56] however we have ruled these effects out with a series of control experiments (see Figure A.12).

We therefore conclude from the electrogravimetric measurements that ion chemistry has a dramatic impact on solvation during uptake, with small ions bringing in ~10 solvent molecules while larger polyatomic anions can enter into the film with few if any waters accompanying them. Literature regarding ion desolvation upon uptake into nanoporous carbon for energy storage applications may provide context for understanding these differences from consideration of solvation effects. Despite obvious differences between nanopourous carbon and a conjugated polymer matrix, especially regarding rigidity and free volume, our results in P3HT show the

identical trend in solvation to experimental observations in nanoporous carbon where smaller ions exhibit more solvation and larger ions less. Levi and coworkers use EQCM to study the solvation numbers of ions confined in carbon nanopores. They conclude that small ions enter carbon nanopores at an apparent mass significantly higher than their anhydrous mass (i.e. the small ion is highly solvated even when confined within a carbon nanopore), while larger ions enter carbon nanopores moderately solvated, and significantly bulker ions enter the film at an apparent mass very near their anhydrous mass (the large anion is nearly completely desolvated).[59–61] Thus, our data appear qualitatively consistent with EQCM studies of ion uptake in nanoporous carbon showing less solvation is expected for a larger ion of equivalent charge, matching our findings of ion solvation number during uptake in P3HT. This dramatic difference in solvation behavior likely influences the anion dependence of the injection barrier, doping density, and charge mobility in the OECTs tested and emphasizes the importance of the polymer-ion interaction in understanding and optimizing OECT materials.

Kinetics. Thus far, we have only considered the steady state operation of the OECTs (constant gate bias for >300 seconds), but the response kinetics are important for interpreting mechanism as well as for practical consideration of the sensitivity of sensors[62,63] and frequency response of OECT devices.[64,65] To investigate the kinetics of the doping and operation of our model P3HT OECTs we study the response to a gate bias step that achieves a 10% (0.1 charge per thiophene) doping ratio (-0.80, -0.75, -0.60, -0.55 V vs. Ag/AgCl for KCl, $KClO_4$, KPF_6, KTFSI respectively). Figure 2.4 A shows the normalized absorption bleach at 552 nm over time following application of the gate bias step. The P3HT shows much more rapid bleaching in the presence of the two larger, minimally hydrated anions (PF_6^- and $TFSI^-$), while the smaller, highly hydrated anions (Cl^- and ClO_4^-) yield slower bleaching kinetics. Figure 2.4 B shows the total charge consumed during the oxidation of

the film. The charge kinetics follow the same trend with the larger ions resulting in faster charge consumption. Figure 2.4 C shows the normalized frequency from the quartz crystal microbalance experiment in response to the gate bias step. The frequency change (proportional to mass change of the film) from slowest to fastest is KCl, $KClO_4$, KPF_6, and KTFSI, in good agreement with the optical bleach data.

Figure 2.4 D shows the normalized transistor current over time for the same 4 electrolytes. Smaller dopant ions (those that go in with larger solvation numbers) result in slower current modulation in the transistor, requiring more than 200 seconds to reach the steady-state transistor current. However, larger dopant anions (those that enter the film less solvated according to the electrogravimetric measurements above) achieve significantly faster gating of the transistor, reaching steady state in the first 30 seconds after the doping bias is applied. If the current modulation was limited purely by diffusion of the bare anion, we would expect the smaller anions to dope the film more quickly. We observe the opposite effect, as previously observed for ionic liquid gated semiconducting polymers,[66] illustrating the importance of the anion chemistry within the polymer matrix. It is worth noting that the dedoping process is significantly faster in *all* cases, with the current modulation occurring within the first few seconds (instead of hundreds of seconds) of the gate bias application (See Figure A.13). For most practical applications of OECT devices, faster measurements are desirable, and we show that, at least for P3HT, simply changing the

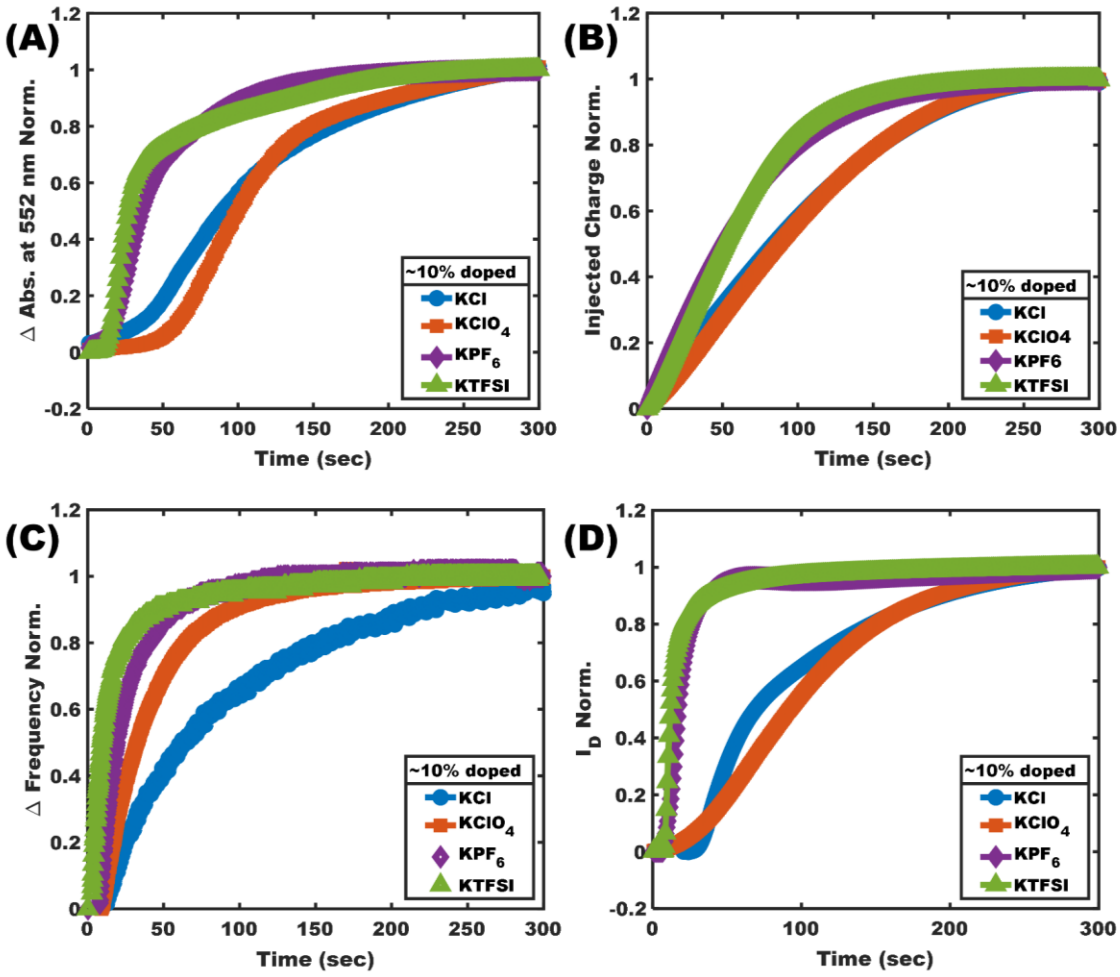

Figure 2.4 Doping kinetics (A) Shows the absorption bleach over time for 4 different ions. (B) Shows normalized charge injected into the film during a doping step. (C) Normalized frequency from QCM during a doping bias step. (D) Normalized transistor current over time for 4 different ions. For all experiments larger anions (KPF_6 and KTFSI) show relatively fast kinetics, while smaller anions (KCl and $KClO_4$) show slower kinetics.

electrolyte an OECT is operated in can improve the response speed. Additionally, different rates of charge modulation point to the possibility of separately sensing multiple anions based on their time-domain response devices as recently investigated by Pecqueur and coworkers.[67] Overall, the differences in doping kinetics highlight the differences in anion chemistry within the polymer and suggest potential applications of anion selectivity based on the time domain response of OECT materials.

Since the kinetics of these doping process are not governed by simple size-based diffusion rates (even when considering the size of the hydrated anion; see Table A.2), there must be energetic

differences in the doping process for each anion. There are 2 main energetic processes for an ion from solution entering a polymer film: 1) the energy associated with any change in solvation from its bulk water state, 2) energy associated with the polymer-ion complex formation, both ion-polymer interaction and any polymer restructuring required to make space for the dopant. For the larger, hydrophobic anions, changes in solvation are not likely a significant factor becasuse the change in the hydration state of these ions is minimal; these ions interact with water very weakly yielding low hydration numbers in bulk solution,[68–71] as well as within P3HT according to our EQCM data. For smaller anions however the energy penalty involved in changing solvation could be significant. Chloride in bulk water has a hydration number of ~6,[72] which is similar (if smaller) than the value of ~10 waters for the chloride entering the film. This difference could be due to the energy required to expand the hydration shell prior to ion sorption into the film, or the formation of larger volume/polymer swelling to accommodate the chloride allowing additional water into the film. Both effects would slow the kinetics and explain the threshold voltage shift. The second energetic component involves the favorability of the polymer-ion interaction. Intuitively it makes sense that a hydrophobic anion such as $TFSI^-$ would be more stable in a polymer matrix than in water. The literature regarding heat of sorption for the anions within a polymer is limited, but in the battery electrolyte literature poly(ethylene oxide) (PEO) is used as the archetypal solid polymer solvent.[73] In that system, we see that KCl salt cannot be dissolved by PEO, while KTFSI does dissolve in solid PEO.[74] Since the cation remains unchanged in this comparison, it could points to a significantly more favorable polymer-anion interaction for $TFSI^-$ compared to Cl^-. Recent simulations of PEO solvation of LiCl and LiTFSI confirm such interpretation, showing $TFSI^-$ has ~33 polymer-ion contacts on average whereas Cl^- only has ~12 polymer-ion contacts.[75] These 2 energetic factors could both contribute to the differences in injection barrier and kinetics (by

changing the activation energy) of these doping process, and illustrate the importance of the polymer-ion interactions in these systems.

Electrochemical Strain Microscopy. Through these classical electrochemical measurements we have shown more facile, complete, and rapid oxidation/reduction of P3HT films by bulky, polyatomic anions than halides. Given the reported materials properties tradeoff between ion uptake and electronic mobility,[76] tools that can help distinguish the nanoscale structure-function relationship are especially useful. Atomic force microscopy (AFM) provides a useful tool to probe this question and has been previously been used to study the swelling due to ion uptake in conjugated polymers.[77,78] We previously used the AFM-based method known as Electrochemical Strain Microscopy (ESM) to show that chloride ion uptake occurs preferentially in the softer (less crystalline) areas of a P3HT film.[27] With this technique, we apply an AC bias to an AFM cantilever in contact with the polymer film in

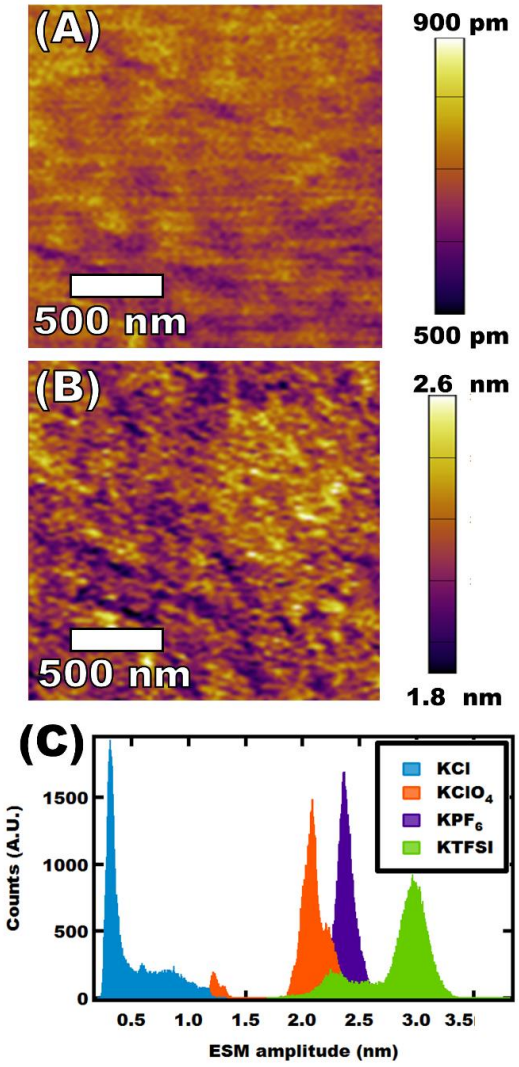

Figure 2.5 Anion dependence of ESM (A) 2 µm x 2 µm ESM image taken in 20 mM KCl at 500 mV AC drive voltage and 0 mV DC offset showing an average ESM amplitude of 0.75 nm. (B) ESM image in 20 mM KTFSI on the same area of the film as in A showing an average ESM amplitude of 2.0 nm. (C) Histogram of ESM amplitude at 700 mV AC drive and -700 mV DC offset in 4 different potassium electrolytes.

electrolyte solution, inducing oxidation/reduction, and concomitant counterion uptake/expulsion, which results in the swelling/deswelling of the polymer. We monitor the swelling at the tip-sample contact resonance as the ESM amplitude. Figure 2.5 A shows an ESM image taken in 20 mM KCl at 500 mV AC drive voltage. The average amplitude of the ESM response is 747 pm with a standard deviation of 19 pm. Figure 2.5 B shows an ESM image take under the same conditions on the same area of the film (see Figure A.14 for correlated topography) in 20 mM KTFSI. In this image the average ESM amplitude is 2000 pm with a standard deviation of 114 pm. Our measured amplitudes correspond to a total swelling of 0.5-1.5 percent, which is in reasonable agreement with recent XRD measurements showing a 3.3 percent expansion of the P3HT crystal structure when gated with an ionic liquid,[29] especially given known issues with quantitative interpretation of ESM amplitudes.[79] To minimize potential artifacts,[80,81] we use the same AFM tip to image samples while only changing the electrolyte for images shown in Figure 2.5. From the uptake images shown in Figure 2.5 A and Figure 2.5 B, it appears that the heterogeneity in ion uptake previously observed with Cl^- dopants[27] is even more pronounced in KTFSI solution. This suggests the nanoscale polymer structure becomes an even more important design consideration with larger dopant anions. Figure 2.5 C shows a histogram of 4 ESM images taken in different electrolytes. Interestingly, the average ESM amplitude from least to greatest is KCl, $KClO_4$, KPF_6, and KTFSI. This trend makes sense in the context of the doping level and doping kinetics data presented above. Since the ESM experiments were conducted under the same drive conditions, we expect those ions that exhibit the fastest kinetics and deepest doping levels show the largest amplitude changes. This trend is exactly what is observed: the ESM swelling amplitudes follow the same trends as the doping level and doping rate curves. We believe this technique will prove especially useful as the field begins to employ OECT polymers and structures with increasingly complex nanoscale

morphologies.[82]

2.3 Conclusions

In summary, we have studied partially amorphous polythiophene-based organic electrochemical transistors that we operated in a variety of different potassium salts with different anions. We observed that the anion type affects both the transistor current and the threshold voltage, with larger molecular anions resulting in lower threshold voltages and greater transistor currents. We studied the anion-dependent doping process by spectroelectrochemistry and coulometry and found that we could achieve higher doping levels (great numbers of electrochemically injected holes) with larger anions like PF_6^-, and TFSI compared to Cl^- and ClO_4^-. Additionally, we found that the mobility of the electronic carriers within the film is dopant anion-dependent, especially at low doping levels. By electrogravimetric measurements we found that smaller, slightly polarizable anions enter the polymer film with a solvation shell of ~10 waters while the larger, highly polarizable anions are able to enter the film with fewer/no waters. Furthermore, we show the doping rate is significantly faster for large, minimally hydrated anions compared to small, highly hydrated anions. We propose that these differences can be attributed to different activation energies for the doping process depending on anion/polymer chemistry. Future experiments to explore the temperature dependence of the doping process to further clarify this are under way. Finally, we show the uptake of anions on the nanoscale is strongly anion-dependent and that ESM can be a valuable technique for understanding the structure-function relationship for novel OECT materials with complex morphologies.

Although P3HT is not a material that demonstrates record transconductance, this study is valuable for clearly demonstrating the importance of favorably tailoring the ion-polymer interaction for future mixed ionic/electronic materials. These results highlight the importance of

electrolyte identity in OECT characterization, especially for repeatable inter-lab comparisons, and design of novel OECT materials.

2.4 METHODS

Materials: Materials including potassium fluoride (KF, Sigma-Aldrich, anhydrous >99.9%), potassium chloride (KCl, Sigma-Aldrich, >99%), potassium bromide (KBr, Sigma-Aldrich, >99.9%), potassium perchlorate ($KClO_4$, Sigma-Aldrich, >99%), potassium hexafluorophosphate (KPF_6, Sigma-Aldrich, >99.5%), potassium bis(trifluoromethanesulfonyl)imide (KTFSI, Sigma-Aldrich, 97%), chlorobenzene (CB, Sigma-Aldrich, >99.8%), poly(3-hexylthiophene-2,5-diyl) regioregular (P200), (P3HT, Rieke Metals, ~54-70 kDa), fluorine-doped tin oxide coated glass (FTO, Sigma-Aldrich 7 Ω/cm^{-1}), and indium tin oxide coated glass (ITO, Thin Film Devices) were purchased from the suppliers noted. Prior to use, the potassium salts were dried in a vacuum oven at 30° C overnight. Deionized water was degassed prior to dissolving potassium salts to a concentration of 20 mM, confirmed by Inductively Coupled Plasma – Optical Emission Spectrophotometer (Perkin Elmer Optima 8300) measurements shown in Table A.3.

Sample Fabrication: P3HT was dissolved in chlorobenzene at 25 mg/mL and stirred at 45° C for 3 hours at 800 RPM. All samples were spin coated onto plasma cleaned (2 min) substrates from room temperature solution in a nitrogen filled glovebox to a thickness of ~140 nm. Films were used as cast, without annealing leading to partially amorphous films. The ion uptake behavior reported herein is likely dominated by these amorphous regions.[27] All samples were initially stressed by 3 cyclic voltammetry curves prior to measurement. Plasma cleaning of all substrates was performed by a Harrick PDC-32G plasma cleaner.

Electrochemical Doping: Gate bias and current were applied/monitored using a potentiostat (MetroOhm Autolab PGSTAT204, Nova 2.1). For all experiments the film substrate was used as

the source/working electrode, a platinum wire was used as the counter electrode, and a leak-free Ag/AgCl electrode (EDAQ ET072) was used as the reference electrode. Steady-state measurements were taken by application of a gate bias for >300 seconds, followed by complete dedoping of the polymer by application of a +0.4 V gate bias for >300 seconds. Gate-bias-doping steps were applied in random order to avoid any systematic errors due to any irreversible processes, though good reversibility was observed (at the biases used, see below). Determination of charge consumed during a doping step was calculated by integration of the current with respect to time as described by Tang and coworkers.[39] Further details are included in A.7.

UV-Vis: Absorption spectra were taken on fluoride-doped tin oxide coated glass (FTO, Sigma-Aldrich, 7 Ω/sq) with an Agilent 8453 spectrophotometer.

Quartz crystal microbalance: Electrogravimetric measurements were performed using 1 inch-diameter gold-coated AT quartz-crystal (Stanford Research Systems, 5 MHz) substrates on an SRS QCM200 instrument. Previous EQCM studies have shown ~100 nm thick conducting polymer films exhibit negligible change in the circuit resistance as a function of potential and that the frequency shift is therefore a direct measure of mass change within the polymer layer.[40–42]

OECT devices: OECTs were made on commercial interdigitated electrodes (NanoSPR) with a channel length (electrode spacing) of 20 μm and a total width of 19 mm (19 interdigitated pairs 1 mm each). The source drain bias/current was applied/read by a Keithley 237 high voltage source measure unit controlled by custom LabView software.

Electrochemical Strain Microscopy: ESM experiments were performed on an Asylum Research Cypher-ES using MikroMasch tapping mode tips (~75 kHz, ~ 2.8 N/m) in a nitrogen environment. The ESM amplitude at the contact resonance was monitored by Dual Amplitude Resonant Frequency Tracking (DART) mode with an 8 KHz width. AC drive bias ranged from 300 mV to

700 mV in experiments presented here and the DC tip voltage was varied from 300 mV to -700 mV.

2.5 Acknowledgements

This paper is based primarily on work supported by the National Science Foundation, NSF DMR-1607242. We gratefully acknowledge the Alvin L. and Verla R. Kwiram endowed fund at the University of Washington for supporting early stages of this research. The authors thank Michael Enright for assistance with ICP, Jarred Olsen for discussions regarding ion desolvation in nanoporous carbon, and Prof. Erin Ratcliff for discussions regarding P3HT doping. Part of this work was conducted at the Molecular Analysis Facility, a National Nanotechnology Coordinated Infrastructure site at the University of Washington that is supported in part by the National Science Foundation (grant ECC-1542101), the University of Washington, the Molecular Engineering & Sciences Institute, the Clean Energy Institute and the National Institutes of Health.

2.6 References

(1) Ma, G.; Feng, E.; Sun, K.; Peng, H.; Li, J.; Lei, Z. A Novel and High-Effective Redox-Mediated Gel Polymer Electrolyte for Supercapacitor. *Electrochim. Acta* **2014**, *135*, 461–466.

(2) Wang, K.; Wu, H.; Meng, Y.; Wei, Z. Conducting Polymer Nanowire Arrays for High Performance Supercapacitors. *Small* **2014**, *10*, 14–31.

(3) Chen, S.-M.; Ramachandran, R.; Mani, V.; Saraswathi, R. Recent Advancements in Electrode Materials for the High-Performance Electrochemical Supercapacitors: A Review. *Int. J. Electrochem. Sci* **2014**, *9*, 4072–4085.

(4) Mike, J. F.; Lutkenhaus, J. L. Electrochemically Active Polymers for Electrochemical Energy Storage: Opportunities and Challenges. *ACS Macro Lett.* **2013**, *2*, 839–844.

(5) Li, S. Z.; Zeng, F.; Chen, C.; Liu, H. Y.; Tang, G. S.; Gao, S.; Song, C.; Lin, Y. S.; Pan, F.; Guo, D. Synaptic Plasticity and Learning Behaviours Mimicked through Ag Interface Movement in an Ag/Conducting Polymer/Ta Memristive System. *J. Mater. Chem. C* **2013**, *1*, 5292–5298.

(6) Isaksson, J.; Kjäll, P.; Nilsson, D.; Robinson, N.; Berggren, M.; Richter-Dahlfors, A. Electronic Control of Ca^{2+} Signalling in Neuronal Cells Using an Organic Electronic Ion Pump. *Nat. Mater.* **2007**, *6*, 673–679.

(7) Jonsson, A.; Sjöström, T. A.; Tybrandt, K.; Berggren, M.; Simon, D. T. Chemical Delivery Array with Millisecond Neurotransmitter Release. *Sci. Adv.* **2016**, *2*, e1601340.
(8) Smela, E. Conjugated Polymer Actuators for Biomedical Applications. *Adv. Mater.* **2003**, *15*, 481–494.
(9) Leleux, P.; Rivnay, J.; Lonjaret, T.; Badier, J. M.; Bénar, C.; Hervé, T.; Chauvel, P.; Malliaras, G. G. Organic Electrochemical Transistors for Clinical Applications. *Adv. Healthc. Mater.* **2015**, *4*, 142–147.
(10) Simon, D. T.; Gabrielsson, E. O.; Tybrandt, K.; Berggren, M. Organic Bioelectronics: Bridging the Signaling Gap between Biology and Technology. *Chem. Rev.* **2016**, *116*, 13009–13041.
(11) Rivnay, J.; Owens, R. M.; Malliaras, G. G. The Rise of Organic Bioelectronics. *Chem. Mater.* **2014**, *26*, 679–685.
(12) Someya, T.; Bao, Z.; Malliaras, G. G. The Rise of Plastic Bioelectronics. *Nature* **2016**, *540*, 379–385.
(13) Panzer, M. J.; Frisbie, C. D. Exploiting Ionic Coupling in Electronic Devices: Electrolyte-Gated Organic Field-Effect Transistors. *Adv. Mater.* **2008**, *20*, 3176–3180.
(14) Lüssem, B.; Keum, C. M.; Kasemann, D.; Naab, B.; Bao, Z.; Leo, K. Doped Organic Transistors. *Chem. Rev.* **2016**, *116*, 13714–13751.
(15) Chiang, C. K.; Fincher, C. R.; Park, Y. W.; Heeger, A. J.; Shirakawa, H.; Louis, E. J.; Gau, S. C.; MacDiarmid, A. G. Electrical Conductivity in Doped Polyacetylene. *Phys. Rev. Lett.* **1977**, *39*, 1098–1101.
(16) Heeger, A. J. Semiconducting and Metallic Polymers: The Fourth Generation of Polymeric Materials. *Curr. Appl. Phys.* **2001**, *1*, 247–267.
(17) Pron, A.; Gawrys, P.; Zagorska, M.; Djurado, D.; Demadrille, R. Electroactive Materials for Organic Electronics: Preparation Strategies, Structural Aspects and Characterization Techniques. *Chem. Soc. Rev.* **2010**, *39*, 2577–2632.
(18) Martinez, J. G.; Otero, T. F.; Jager, E. W. H. Electrochemo-Dynamical Characterization of Polypyrrole Actuators Coated on Gold Electrodes. *Phys. Chem. Chem. Phys.* **2016**, *18*, 827–836.
(19) Zama, T.; Hara, S.; Takarshima, W.; Keiichi, K. Comparison of Conducting Polymer Actuators Based on Polypyrrole Doped with BF_4^-, PF_6^-, $CF_3S0_3^-$, and $CI0_4^-$. *Bull. Chem. Soc. Japan.* **2005**, *78*, 506–511.
(20) Rivnay, J.; Leleux, P.; Ferro, M.; Sessolo, M.; Williamson, A.; Koutsouras, D. A.; Khodagholy, D.; Ramuz, M.; Strakosas, X.; Owens, R. M.; et al. High-Performance Transistors for Bioelectronics through Tuning of Channel Thickness. *Sci. Adv.* **2015**, *1*, e1400251.
(21) Kergoat, L.; Herlogsson, L.; Piro, B.; Pham, M. C.; Horowitz, G.; Crispin, X.; Berggren, M. Tuning the Threshold Voltage in Electrolyte-Gated Organic Field-Effect Transistors. *Proc. Natl. Acad. Sci.* **2012**, *109*, 8394–8399.
(22) Giovannitti, A.; Sbircea, D.-T.; Inal, S.; Nielsen, C. B.; Bandiello, E.; Hanifi, D. A.; Sessolo, M.; Malliaras, G. G.; McCulloch, I.; Rivnay, J. Controlling the Mode of Operation of Organic Transistors through Side-Chain Engineering. *Proc. Natl. Acad. Sci.* **2016**, *113*, 12017–12022.
(23) Pacheco-Moreno, C. M.; Schreck, M.; Scaccabarozzi, A. D.; Bourgun, P.; Wantz, G.; Stevens, M. M.; Dautel, O. J.; Stingelin, N. The Importance of Materials Design to Make Ions Flow: Toward Novel Materials Platforms for Bioelectronics Applications. *Adv.*

Mater. **2017**, *29*, 1604446.
(24) Schmidt, M. M.; ElMahmoudy, M.; Malliaras, G. G.; Inal, S.; Thelakkat, M. Smaller Counter Cation for Higher Transconductance in Anionic Conjugated Polyelectrolytes. *Macromol. Chem. Phys.* **2017**, *219*, 1700374.
(25) Inal, S.; Malliaras, G. G.; Rivnay, J. Benchmarking Organic Mixed Conductors for Transistors. *Nat. Commun.* **2017**, *8*, 1767.
(26) Rivnay, J.; Inal, S.; Collins, B. A.; Sessolo, M.; Stavrinidou, E.; Strakosas, X.; Tassone, C.; Delongchamp, D. M.; Malliaras, G. G. Structural Control of Mixed Ionic and Electronic Transport in Conducting Polymers. *Nat. Commun.* **2016**, *7*, 11287.
(27) Giridharagopal, R.; Flagg, L. Q.; Harrison, J. S.; Ziffer, M. E.; Onorato, J.; Luscombe, C. K.; Ginger, D. S. Electrochemical Strain Microscopy Probes Morphology-Induced Variations in Ion Uptake and Performance in Organic Electrochemical Transistors. *Nat. Mater.* **2017**, *16*, 737–742.
(28) Kawai, T.; Nakazono, M.; Yoshino, K. Effects of Doping on the Crystal Structure of Poly(3-Alkylthiophene). *J. Mater. Chem.* **1992**, *2*, 903–906.
(29) Guardado, J. O.; Salleo, A. Structural Effects of Gating Poly(3-Hexylthiophene) through an Ionic Liquid. *Adv. Funct. Mater.* **2017**, *27*, 1701791.
(30) Thelen, J. L.; Wu, S. L.; Javier, A. E.; Srinivasan, V.; Balsara, N. P.; Patel, S. N. Relationship between Mobility and Lattice Strain in Electrochemically Doped Poly(3-Hexylthiophene). *ACS Macro Lett.* **2015**, *4*, 1386–1391.
(31) Giovannitti, A.; Thorley, K. J.; Nielsen, C. B.; Li, J.; Donahue, M. J.; Malliaras, G. G.; Rivnay, J.; McCulloch, I. Redox-Stability of Alkoxy-BDT Copolymers and Their Use for Organic Bioelectronic Devices. *Adv. Funct. Mater.* **2018**, *28*, 1706325.
(32) Giovannitti, A.; Nielsen, C. B.; Sbircea, D.-T.; Inal, S.; Donahue, M.; Niazi, M. R.; Hanifi, D. A.; Amassian, A.; Malliaras, G. G.; Rivnay, J.; et al. Erratum: N-Type Organic Electrochemical Transistors with Stability in Water. *Nat. Commun.* **2016**, *7*, 13955.
(33) Nielsen, C. B.; Giovannitti, A.; Sbircea, D. T.; Bandiello, E.; Niazi, M. R.; Hanifi, D. A.; Sessolo, M.; Amassian, A.; Malliaras, G. G.; Rivnay, J.; et al. Molecular Design of Semiconducting Polymers for High-Performance Organic Electrochemical Transistors. *J. Am. Chem. Soc.* **2016**, *138*, 10252–10259.
(34) Duong, D. T.; Wang, C.; Antono, E.; Toney, M. F.; Salleo, A. The Chemical and Structural Origin of Efficient P-Type Doping in P3HT. *Org. Electron. physics, Mater. Appl.* **2013**, *14*, 1330–1336.
(35) Jacobs, I. E.; Moulé, A. J. Controlling Molecular Doping in Organic Semiconductors. *Adv. Mater.* **2017**, *29*, 1703063.
(36) Enengl, C.; Enengl, S.; Pluczyk, S.; Havlicek, M. Doping-Induced Absorption Bands in P3HT : Polarons and Bipolarons **. **2016**, *17*, 3836–3844.
(37) White, S. P.; Dorfman, K. D.; Frisbie, C. D. Operating and Sensing Mechanism of Electrolyte-Gated Transistors with Floating Gates: Building a Platform for Amplified Biodetection. *J. Phys. Chem. C* **2016**, *120*, 108–117.
(38) Seshadri, P.; Manoli, K.; Schneiderhan-Marra, N.; Anthes, U.; Wierzchowiec, P.; Bonrad, K.; Di Franco, C.; Torsi, L. Low-Picomolar, Label-Free Procalcitonin Analytical Detection with an Electrolyte-Gated Organic Field-Effect Transistor Based Electronic Immunosensor. *Biosens. Bioelectron.* **2018**, *104*, 113–119.
(39) Tang, H.; Zhu, L.; Harima, Y.; Yamashita, K. Chronocoulometric Determination of Doping Levels of Polythiophenes: Influences of Overoxidation and Capacitive Processes.

Synth. Met. **2000**, *110*, 105–113.
(40) Hillman, A.; Daisley, S. J. S.; Bruckenstein, S.; Robert Hillman, A.; Daisley, S. J. S.; Bruckenstein, S. Solvent Effects on the Electrochemical P-Doping of PEDOT. *Phys. Chem. Chem. Phys.* **2007**, *9*, 2379–2388.
(41) Hillman, A. R.; Daisley, S. J.; Bruckenstein, S. Ion and Solvent Transfers and Trapping Phenomena during N-Doping of PEDOT Films. *Electrochim. Acta* **2008**, *53*, 3763–3771.
(42) Hillman, A. R.; Daisley, S. J.; Bruckenstein, S. Kinetics and Mechanism of the Electrochemical P-Doping of PEDOT. *Electrochem. commun.* **2007**, *9*, 1316–1322.
(43) Newman, C. R.; Frisbie, C. D.; Da Silva Filho, D. A.; Brédas, J. L.; Ewbank, P. C.; Mann, K. R. Introduction to Organic Thin Film Transistors and Design of N-Channel Organic Semiconductors. *Chem. Mater.* **2004**, *16*, 4436–4451.
(44) Wang, C.; Duong, D. T.; Vandewal, K.; Rivnay, J.; Salleo, A. Optical Measurement of Doping Efficiency in Poly(3-Hexylthiophene) Solutions and Thin Films. *Phys. Rev. B - Condens. Matter Mater. Phys.* **2015**, *91*, 085205.
(45) Jiang, X.; Harima, Y.; Yamashita, K.; Tada, Y.; Ohshita, J.; Kunai, A. Doping-Induced Change of Carrier Mobilities in Poly(3-Hexylthiophene) Films with Different Stacking Structures. *Chem. Phys. Lett.* **2002**, *364*, 616–620.
(46) Harima, Y.; Kunugi, Y.; Yamashita, K.; Shiotani, M. Determination of Mobilities of Charge Carriers in Electrochemically Anion-Doped Polythiophene Film. *Chem. Phys. Lett.* **2000**, *317*, 310–314.
(47) Shimotani, H.; Diguet, G.; Iwasa, Y. Direct Comparison of Field-Effect and Electrochemical Doping in Regioregular Poly(3-Hexylthiophene). *Appl. Phys. Lett.* **2005**, *86*, 10–13.
(48) Paulsen, B. D.; Frisbie, C. D. Dependence of Conductivity on Charge Density and Electrochemical Potential in Polymer Semiconductors Gated with Ionic Liquids. *J. Phys. Chem. C* **2012**, *116*, 3132–3141.
(49) Ukai, S.; Ito, H.; Marumoto, K.; Kuroda, S. I. Electrical Conduction of Regioregular and Regiorandom Poly(3- Hexylthiophene) Doped with Iodine. *J. Phys. Soc. Japan* **2005**, *74*, 3314–3319.
(50) Jiang, X.; Patil, R.; Harima, Y.; Ohshita, J.; Kunai, A. Influences of Self-Assembled Structure on Mobilities of Charge Carriers in π-Conjugated Polymers. *J. Phys. Chem. B* **2005**, *109*, 221–229.
(51) Yoon, C. O.; Reghu, M.; Moses, D.; Heeger, A. J.; Cao, Y.; Chen, T. A.; Wu, X.; Rieke, R. D. Hopping Transport in Doped Conducting Polymers in the Insulating Regime near the Metal-Insulator Boundary: Polypyrrole, Polyaniline and Polyalkylthiophenes. *Synth. Met.* **1995**, *75*, 229–239.
(52) Arkhipov, V. I.; Emelianova, E. V.; Heremans, P.; Bässler, H. Analytic Model of Carrier Mobility in Doped Disordered Organic Semiconductors. *Phys. Rev. B* **2005**, *72*, 235202.
(53) Friedlein, J. T.; Rivnay, J.; Dunlap, D. H.; McCulloch, I.; Shaheen, S. E.; McLeod, R. R.; Malliaras, G. G. Influence of Disorder on Transfer Characteristics of Organic Electrochemical Transistors. *Appl. Phys. Lett.* **2017**, *111*, 023301.
(54) Deakin, M. R.; Buttry, D. A. Electrochemical Applications of the Quartz Crystal Microbalance. *Anal. Chem.* **1989**, *61*, 1147A–1154A.
(55) Sauerbrey, G. Verwendung von Schwingquarzen Zur Wägung Dünner Schichten Und Zur Mikrowägung. *Zeitschrift für Phys.* **1959**, *155*, 206–222.
(56) Zhang, L.; Andrew, T. L. Deposition Dependent Ion Transport in Doped Conjugated

Polymer Films: Insights for Creating High-Performance Electrochemical Devices. *Adv. Mater. Interfaces* **2017**, *4*, 1700873.
(57) Bruckenstein, S.; Shay, M. Experimental Aspects of Use of the Quartz Crystal Microbalance in Solution. *Electrochim. Acta* **1985**, *30*, 1295–1300.
(58) Meana-Esteban, B.; Sundfors, F.; Espíndola, P.; Kvarnström, C.; Heinze, J.; Ivaska, A. Correlation between Conductance and Mass Changes during P-Doping of 2-Methoxynaphthalene Films. *Electrochim. Acta* **2008**, *53*, 7988–7994.
(59) Levi, M. D.; Levy, N.; Sigalov, S.; Salitra, G.; Aurbach, D.; Maier, J. Electrochemical Quartz Crystal Microbalance (EQCM) Studies of Ions and Solvents Insertion into Highly Porous Activated Carbons. *J. Am. Chem. Soc.* **2010**, *132*, 13220–13222.
(60) Levi, M. D.; Sigalov, S.; Salitra, G.; Elazari, R.; Aurbach, D. Assessing the Solvation Numbers of Electrolytic Ions Confined in Carbon Nanopores under Dynamic Charging Conditions. *J. Phys. Chem. Lett.* **2011**, *2*, 120–124.
(61) Tsai, W.-Y.; Taberna, P.-L.; Simon, P. Electrochemical Quartz Crystal Microbalance (EQCM) Study of Ion Dynamics in Nanoporous Carbons. *J. Am. Chem. Soc.* **2014**, *136*, 8722–8728.
(62) Wang, N.; Liu, Y.; Fu, Y.; Yan, F. AC Measurements Using Organic Electrochemical Transistors for Accurate Sensing. *ACS Appl. Mater. Interfaces* **2017**, Article ASAP 10.1021/acsami.7b07668.
(63) Gualandi, I.; Tonelli, D.; Mariani, F.; Scavetta, E.; Marzocchi, M.; Fraboni, B. Selective Detection of Dopamine with an All PEDOT:PSS Organic Electrochemical Transistor. *Sci. Rep.* **2016**, *6*, 35419.
(64) Morozovska, A. N.; Eliseev, E. A.; Bravina, S. L.; Ciucci, F.; Svechnikov, G. S.; Chen, L. Q.; Kalinin, S. V. Frequency Dependent Dynamical Electromechanical Response of Mixed Ionic-Electronic Conductors. *J. Appl. Phys.* **2012**, *111*, 0104107.
(65) Friedlein, J. T.; Donahue, M. J.; Shaheen, S. E.; Malliaras, G. G.; McLeod, R. R. Microsecond Response in Organic Electrochemical Transistors: Exceeding the Ionic Speed Limit. *Adv. Mater.* **2016**, 8398–8404.
(66) Lee, J.; Kaake, L. G.; Cho, J. H.; Zhu, X.-Y.; Lodge, T. P.; Frisbie, D. Ion Gel-Gated Polymer Thin-Film Transistors: Operating Mechanism and Characterization of Gate Dielectric Capacitance, Switching Speed, and Stability. *J. Phys. Chem. B* **2009**, *113*, 8972–8981.
(67) Pecqueur, S.; Guérin, D.; Vuillaume, D.; Alibart, F. Cation Discrimination in Organic Electrochemical Transistors by Dual Frequency Sensing. *Org. Electron. physics, Mater. Appl.* **2018**, *57*, 232–238.
(68) Ghatee, M. H.; Zolghadr, A. R. Local Depolarization in Hydrophobic and Hydrophilic Ionic Liquids/Water Mixtures: Car-Parrinello and Classical Molecular Dynamics Simulation. *J. Phys. Chem. C* **2013**, *117*, 2066–2077.
(69) Smiechowski, M. Anion–water Interactions of Weakly Hydrated Anions: Molecular Dynamics Simulations of Aqueous $NaBF_4$ and $NaPF_6$. *Mol. Phys.* **2016**, *114*, 1831–1846.
(70) Śmiechowski, M.; Gojlo, E.; Stangret, J. Ionic Hydration in LiPF6, $NaPF_6$, and KPF_6 Aqueous Solutions Derived from Infrared HDO Spectra. *J. Phys. Chem. B* **2004**, *108*, 15938–15943.
(71) Katayanagi, H.; Nishikawa, K.; Shimozaki, H.; Miki, K.; Westh, P.; Koga, Y. Mixing Schemes in Ionic Liquid - H_2O Systems: A Thermodynamic Study. *J. Phys. Chem. B* **2004**, *108*, 19451–19457.

(72) Soper, A. K.; Weckström, K. Ion Solvation and Water Structure in Potassium Halide Aqueous Solutions. *Biophys. Chem.* **2006**, *124*, 180–191.
(73) Orädd, G.; Edman, L.; Ferry, A. Diffusion: A Comparison between Liquid and Solid Polymer LiTFSI Electrolytes. *Solid State Ionics* **2002**, *152–153*, 131–136.
(74) Bruce, P. G. Coordination Chemsistry in the Solid State. *Philos. Trans. R. Soc. A Math. Phys. Eng. Sci.* **1996**, *354*, 415–436.
(75) Savoie, B. M.; Webb, M. A.; Miller, T. F. Enhancing Cation Diffusion and Suppressing Anion Diffusion via Lewis-Acidic Polymer Electrolytes. *J. Phys. Chem. Lett.* **2017**, *8*, 641–646.
(76) Rivnay, J.; Inal, S.; Salleo, A.; Owens, R. M.; Berggren, M.; Malliaras, G. G. Organic Electrochemical Transistors. *Nat. Rev. Mater.* **2018**, *3*, 17086.
(77) Skompska, M.; Szkurlat, A.; Kowal, A.; Szklarczyk, M. Spectroelectrochemical and AFM Studies of Doping-Undoping of Poly(3-Hexylthiophene) Films in Propylene Carbonate and Aqueous Solutions of $LiClO_4$. *Langmuir* **2003**, *19*, 2318–2324.
(78) Smela, E.; Gadegaard, N. Volume Change in Polypyrrole Studied by Atomic Force Microscopy. *J. Phys. Chem. B* **2001**, *105*, 9395–9405.
(79) Labuda, A.; Proksch, R. Quantitative Measurements of Electromechanical Response with a Combined Optical Beam and Interferometric Atomic Force Microscope. *Appl. Phys. Lett.* **2015**, *106*, 253103.
(80) Li, J.; Li, J.-F.; Yu, Q.; Chen, Q. N.; Xie, S. Strain-Based Scanning Probe Microscopies for Functional Materials, Biological Structures, and Electrochemical Systems. *J. Mater.* **2015**, *1*, 3–21.
(81) Johann, F.; Hoffmann, Á.; Soergel, E. Impact of Electrostatic Forces in Contact-Mode Scanning Force Microscopy. *Phys. Rev. B - Condens. Matter Mater. Phys.* **2010**, *81*, 094109.
(82) Giovannitti, A.; Maria, I. P.; Hani, D.; Donahue, M. J.; Bryant, D.; Barth, K. J.; Makdah, B. E.; Savva, A.; Moia, D.; Reid, O. G.; et al. Role of the Side Chain on the Performance of N-Type Conjugated Polymers in Aqueous Electrolytes. *Chem. Mater.* **2018**, *30*, 2945–2953.

Chapter 3. Polymer Crystallinity Controls Water Uptake in Glycol Side Chain Polymer Organic Electrochemical Transistors[2]

3.1 INTRODUCTION

Conjugated polymers have recently exhibited a surge of new applications that utilize their mixed electronic/ionic conduction properties, including bioelectronics,[1–5] thermoelectrics,[6] electrochromics,[7,8] supercapacitors and solid state batteries,[9–11] neuromorphic computing,[12] and all organic logic circuits.[13] Specifically for bioelectronics, conjugated polymers have been used for ion pumps for drug delivery,[14,15] for highly sensitive analyte-specific detectors,[16–18] and for recording electrophysiological activity.[19] For many of these bioelectronics applications, organic electrochemical transistors (OECTs) have emerged as a promising platform for transducing small changes in ion concentrations to large changes in electrical current.[20] During OECT operation, a gate bias applied to solution induces electrochemical doping of the polymer active layer – i.e. electronic charges are injected from the substrate into the polymer and ions from solution move into the polymer matrix to electronically compensate the injected electronic charge. This doping process results in modulation of the channel conductivity and therefore the current between the source and drain electrodes (I_D) varies.[20–22] In addition to their use in bioelectronics applications, OECTs also provide a convenient model platform to study the mixed conduction properties of conjugated polymers.

Inal and colleagues recently proposed using the product of the electronic carrier mobility (μ) and the volumetric capacitance (C*) as the figure of merit for the steady-state efficiency of mixed

[2] Reproduced with permission from Flagg, L. Q.; Bischak, C. G.; Onorato, J. W.; Rashid, R. B.; Luscombe, C. K.; Ginger, D. S. Polymer Crystallinity Controls Water Uptake in Glycol Side-Chain Polymer Organic Electrochemical Transistors. *J. Am. Chem. Soc.* **2019**, *141*, 4345–4354. Copyright 2019 American Chemical Society.

electronic/ionic conductor materials.[23] This value can be extracted from Equation 1 by measuring the transconductance (g_m) of OECTs, where the channel width (W), length (L), and film thickness (d), as well as the gate bias (V_G) and threshold voltage (V_T) are known.

$$g_m = \frac{W\,d}{L}\,\mu\,C^*\,(V_T - V_G) \quad (1)$$

The product μC* is an intrinsic property of the OECT active layer and thus allows for the separation of the device geometry from materials properties, improving the comparison of different OECT active layer materials. In both depletion mode and accumulation mode OECT materials, a design trade-off between the carrier mobility and volumetric capacitance has been reported.[24–26] To a first approximation, high electronic mobility can be viewed as the result of a well-ordered, more crystalline film morphology,[27] which tends to inhibit bulk ionic transport and storage. On the other hand, a high C* is achieved in disordered and highly amorphous film morphologies that allow for high ion mobility, but typically poor electronic mobility.[25] Recently, this trade-off was directly observed by Giridharagopal et al., showing that ion uptake occurs preferentially in softer, presumably amorphous, regions of a hydrophobic conjugated polymer film.[28] Despite the challenge of balancing electronic and ionic transport properties, a number of high-performing OECT materials exist today, with μC* values approaching 300 F cm^{-1} V^{-1} s^{-1}.[23,29]

Poly(3,4-ethylenedioxythiophene) polystyrene sulfonate (PEDOT:PSS) is the most widely used OECT material due to its commercial availability and high performance (relatively high μ and moderate C*, resulting in μC* of 50 F cm^{-1} V^{-1} s^{-1}).[23] However, PEDOT:PSS operates in depletion mode rather than accumulation mode, which is undesirable for some applications because of the poor on/off ratio at low bias. Additionally, composite systems like PEDOT:PSS lack the synthetic flexibility of a single-phase system, and can exhibit a lower maximum capacitance (though

composites may confer other advantages). As a result, there is currently much interest in developing new single-phase polymers that operate in accumulation mode. Much of the work aimed at developing new accumulation mode materials has focused on side-chain engineering for more efficient ion uptake and transport. Early work on electrolyte-gated organic transistors showed that carboxylic acid capped side chains resulted in significantly higher transistor currents compared to the alkyl side chain analogue in both solid polyelectrolyte[30] and aqueous environments.[31] Further work on aqueous electrolyte-gated organic transistors showed that increasing the fraction of alcohol capped side chains versus alkyl side chains results in both faster and greater magnitude of ion uptake.[32] These results were attributed largely to the more hydrophilic polymer leading to more facile ion uptake within the bulk of the film. More recently, ethylene glycol-based side chain polymers have shown very promising ion uptake and transport properties in both p-type and n-type polymers in aqueous electrolytes. OECT performance enhancement using oligoethylene glycol side chains is generalizable to a number of different conjugated backbones including polythiophene,[33] benzo dithiophene,[34] propylenedioxythiophenes,[35] and bithiophene–thienothiophene.[29] Additionally, ethylene glycol side chains have been shown to increase OECT performance compared to their alkyl analogues in n-type polymers based on naphthalene tetracarboxylic diimide.[36,37] In each of these instances, the presence of ethylene glycol side chains improves both the steady-state characteristics (transconductance) and the switching kinetics of OECTs. Well-designed polymers now function as single phase, accumulation mode OECTs with volumetric capacitances approaching the theoretical limit of approximately 400 F cm^{-3} in aqueous environments.[38,39]

While side chain engineering in accumulation-mode OECTs has greatly increased volumetric capacitances,[40] many of these molecularly designed polymers still suffer from low mobilities.[23]

Decades of research into organic field- effect transistors (OFETs) has yielded clear design rules for improving electronic mobility in dry polymers: (1) minimize the energetic disorder along the polymer chain by designing a rigid, planar conjugated backbone that maximizes orbital overlap with adjacent chains, and (2) ensure a nanoscale morphology that results in well-connected crystalline domains.[41] For many OFET polymers, thermal annealing is used to increase the crystallinity, and thereby electronic mobility.[42–44] Unlike OFETs, OECTs operate in an aqueous environment and it is, therefore, unclear whether increased crystallinity will impact the mobility the same way when the polymer is hydrated. It is important to note that none of the reported ethylene glycol side chain polymers reported to date have been annealed at sufficiently high temperatures to cause a significant polymer reorganization.[29,33,35,37] To establish design rules for optimizing the mobility of OECTs, there is thus a need for an updated understanding of electronic transport in hydrated polymer systems to account for the interaction between the polymer, the polymer morphology, the solvent (water in the case of bioelectronics), and the dopant ion. The importance of such interactions are highlighted by recent papers where the OECT performance depends on the identity of the dopant ion and its hydration shell.[45,46] Recent work also examined the role of water on the electronic transport properties and found reduced mobility in a more hydrated film.[47–49] As the number of applications that require mixed electronic/ionic conducting materials continues to grow, updated materials design rules will be extremely important.

Here, we report the synthesis and performance of poly(3-{[2-(2-methoxyethoxy)ethoxy]methyl}thiophene-2,5-diyl) (P3MEEMT), a new high-efficiency material for OECTs with ethylene glycol-based side chains that has $\mu C^* = 49.1 \pm 5.0$ F cm^{-1} V^{-1} s^{-1} in 100 mM KCl, comparable to state-of-the-art OECT active layer materials.[23] We use P3MEEMT as a model system to investigate how the side-chain impacts OECT performance and anion injection,

and compare its electrochemical doping properties to those of poly(3-hexylthiophene-2,5-diyl) (P3HT), a similar polythiophene derivative with alkyl-based side chains. We find a similar anion-dependent threshold voltage shift in P3MEEMT as previously observed in P3HT.[45] We also find that the anion injection kinetics are much faster in P3MEEMT compared to P3HT and depend less on the anion identity. We propose that the origin of the difference in doping kinetics between P3MEEMT and P3HT stems from how water affects the crystal structure of each material. Using grazing incidence X-ray diffraction (GIXRD), we find that the crystal lattice of P3MEEMT readily expands and hydrates in solution, allowing ions to move readily throughout the material, whereas the crystal lattice of P3HT expands to accommodate the charge compensating anions only upon electrochemically-driven ion injection.

In addition, we investigate how the degree of crystallinity impacts P3MEEMT OECT performance. Surprisingly, we find that highly crystalline P3MEEMT has a lower OECT mobility compared to amorphous P3MEEMT, yet the OFETs fabricated with P3MEEMT show the reverse trend: the mobility is much higher for crystalline P3MEEMT than amorphous P3MEEMT. We attribute these differences in OECT mobility to the effect of hydration on the connectivity of crystalline domains within the film. Using electrochemical quartz crystal microbalance gravimetry (E-QCM), we find that the amorphous P3MEEMT film swells more upon hydration and expels more water upon electrochemical doping compared to crystalline P3MEEMT. Although crystalline P3MEEMT swells less, we hypothesize that the swelling that does occur disrupts percolation pathways between crystalline regions and significantly lowers the OECT mobility. We support this hypothesis with photoinduced force microscopy (PiFM) of doped P3MEEMT and find a higher degree of dopant heterogeneity in the crystalline film. This observation points to potentially disconnected regions in the crystalline film that, when hydrated, lower the overall mobility.

3.2 Results and Discussion

P3MEEMT OECT Device Performance and Anion Dependence. **Figure 3.1 A** shows the molecular structures of P3MEEMT and P3HT. Both polymers have the same polythiophene backbone, but P3MEEMT has ethylene glycol-based side chains and P3HT has alkyl side chains. Polymer synthesis is described in the Supporting Information and **Figure B.1** shows a ^{1}H NMR spectra. **Figure 3.1 B** shows the geometry used for device testing. Briefly, flexible polyethylene terephthalate (PET) substrates were prepatterned with transistor electrodes of varying dimensions, the polymer active layer was then deposited, followed by the application of an insulating masking layer. **Figure 3.1 C** shows transfer curves (representative output curves shown in **Figure B.2**) for an OECT with a P3MEEMT active layer in both 0.1 M potassium chloride (KCl) and 0.1 M potassium hexafluorophosphate (KPF_6) electrolytes. The maximum current (light blue line) achieved within the potential window is 5 times higher in KPF_6 than in KCl (light red line), resulting in a significantly higher transconductance (dotted lines) in KPF_6. We attribute much of this difference to a 126 mV ± 25 mV decrease in the threshold voltage in KPF_6 compared to in KCl (**Figure B.3**). We use the oxidation of ferrocene to verify the observed shift in threshold voltage is largely due to more facile oxidation of the polymer in KPF_6, not differences in the potential of the gate electrode (**Figure B.4**). This behavior follows the same trend as previously observed in hydrophobic P3HT[45] and in the record mixed conductor, p(g2T-TT).[46] Together these results point to anion-dependent threshold voltage shift as a general principle of OECT operation, regardless of hydrophilicity of the polymer. In general, larger, more polarizable anions with a lower surface charge density require a smaller driving force to inject into the semiconducting polymer. This phenomenon could stem from competition between ion hydration and semiconductor polymer doping, as the observed trend for doping appears to

follow the Hofmeister series.[50] More chaotropic ions tend to dope the polymer more easily than more kosmotropic ions in both P3MEEMT and P3HT. It is worth noting that hydrolysis of certain polyatomic anions can decrease the pH of the solution and have strong effect on the polymer doping.[46] However, we do not measure significant acid formation and control experiments indicate that the small pH difference between KPF_6 and KCl do not result in a large shift in oxidation potential (**Figure B.5**).

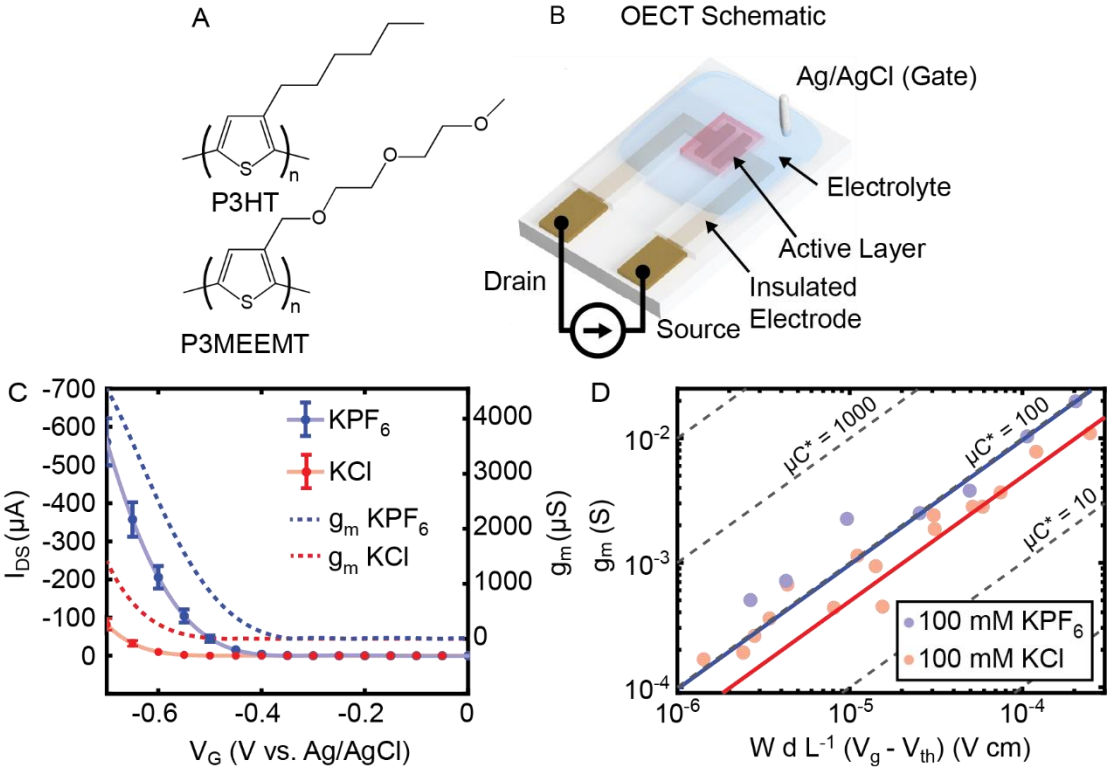

Figure 3.1 (A) Molecular structures of poly(3-{[2-(2-methoxyethoxy)ethoxy]methyl}thiophene-2,5-diyl) (P3MEEMT) and poly(3-hexylthiophene-2,5-diyl) (P3HT), (B) OECT device structure and testing schematic. (C) Transfer curves at VD = 600 mV averaged from 6 transistors (W = 200 µm, L = 20 µm, thickness 80 nm) in 100 mM KCl (red) and 100 mM KPF6 (blue). Dotted lines show the transconductance in each electrolyte on the right axis. (D) Determination of µC* by plotting the maximum transconductance against the geometric parameters. Solid lines indicate fits.

To determine the µC* product of P3MEEMT, we use Equation 1, which relates the measured transconductance to the µC*, junction dimensions, polymer thickness, threshold voltage, and operating voltage. By plotting the transconductance measured on a variety of transistor

geometries against these geometric parameters, we can solve for μC*, as shown in **Figure 3.1 D**. In 100 mM KCl, we obtain a μC* value of 49.1 ± 5.0 F cm^{-1} V^{-1} s^{-1}. This μC* is similar to that reported for typical PEDOT:PSS[23] and 5 times greater than that of P3HT (μC* = 10.4 ± 3.1 F cm^{-1} V^{-1} s^{-1}) (**Figure B.6**). To ensure that our values of μC* are consistent with previously-established OECT benchmarks, we compare our devices to lithographically defined parylene peel-off method of Malliaras et al.[25] (**Figure B.7**) and find that our measured μC* matches at high gate biases (Vg <= -0.5 V). This relatively high μC* of P3MEEMT places it among the best performing OECT materials, while its similarity in structure to P3HT allows us to directly explore how the side chain affects OECT device performance. The blue line in **Figure 3.1 D** shows the μC* when the devices are tested in 100 mM KPF_6, resulting in an even higher μC* of 96.7 ± 10.2 F cm^{-1} V^{-1} s^{-1}. We measure the volumetric capacitance of P3MEEMT films in both electrolytes by electrochemical impedance spectroscopy (EIS) and find that C* nearly doubles to 294 F cm^{-3} in KPF_6 compared to KCl (C* ~= 175 F cm^{-3} in KCl) (**Figure B.8**). Therefore, we attribute the increase in μC* with changing ion type almost entirely to an increase in capacitance, implying that the electronic carrier mobility is less dependent on the identity of the of dopant, at least at the highest doping levels, consistent with previous reports.[45] This result also suggests that, within the electrochemical window of water, approximately twice as many sites are available for doping when using PF_6^- anions as a Cl^-. The maximum theoretical capacitance for this polymer is approximately 400 F cm^{-3},[39] so we conclude that in PF_6^- most of the possible sites for charge storage are occupied at a gate bias of 0.7 V.

P3HT and P3MEEMT Doping Kinetics. We next investigate how the polymer side chain and anion affect charge injection kinetics. **Figure 3.2 A** shows how the absorption spectrum changes over time with electrochemical doping using spectroelectrochemistry for P3HT and

P3MEEMT with either Cl^- or PF_6^- as the anion (V_G = 0.7 V and 0.5 s between spectra). In all cases, the magnitude of the main absorption peak decreases with time and a redshifted polaron peak grows in. For both P3MEEMT and P3HT, using PF_6^- as the anion results in larger decrease in the main absorption peak and a larger increase in the polaron peak, indicating a higher degree of doping compared to using Cl^-, consistent with our C* measurements and device data above. Additionally, doping kinetics in P3MEEMT with both anions is approximately 150 times faster than those of P3HT.

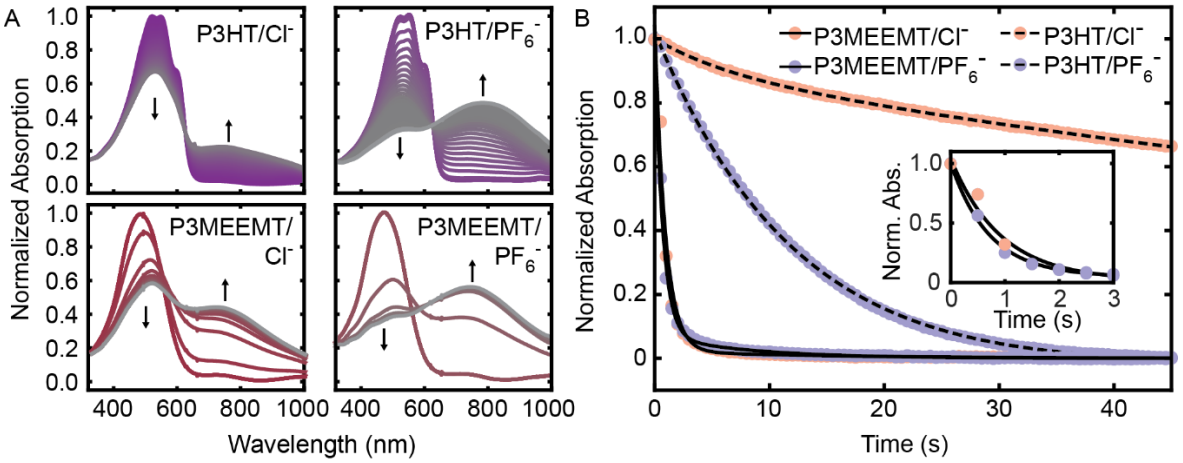

Figure 3.2 (A) UV-Vis spectra of P3HT and P3MEEMT upon electrochemical doping at 0.7 V in 100 mM solutions of KCl and KPF6. The main absorption decreases with increased doping levels and the polaron peak grows in. (B) Comparison of the doping kinetics of P3MEEMT and P3HT in 100 mM solutions of KCl and KPF6 at 0.5 V for doping with PF6- and 0.7 V for Cl-. The kinetics traces of P3MEEMT with Cl- and PF6- overlap significantly, as shown in the inset with the corresponding fits.

Figure 3.2 B plots the decrease in absorption of the main absorption peak for P3HT and P3MEEMT for both anions as a function of time and the corresponding biexponential fits. Here, we account for the threshold voltage shift between the Cl^- and PF_6^- anions by comparing doping kinetics measured at 0.7 V for Cl^- and 0.5 V for PF_6^-. Even after accounting for this difference, the doping kinetics in P3HT are ~15 times slower for Cl^- (145.3 +/- 2.1 s) than for PF_6^- (10.4 +/- 3.1 s). However, we observe more similar doping kinetics between Cl^- (0.82 +/- 0.03 s) and PF_6^- (0.71 +/- 0.02 s) in P3MEEMT although doping with PF_6^- is still slightly faster. We observe

similar results if we compare ion injection kinetics at 0.5 V for P3MEEMT and 0.7 V for P3HT (**Figure B.9**). The spectroelectrochemistry results suggest that the speed of electrochemical doping depends strongly on the side chain chemistry. The ethylene glycol-based side chains allow ions to inject much faster into the film than the alkyl side chains, presumably due to the hydrophilic nature of the ethylene glycol-containing polymer. Additionally, although the timescale of ion injection depends on the anion in P3HT, the choice of anion for P3MEEMT does not appear to influence charge injection rates nearly as significantly.

P3HT and P3MEEMT Structural Changes Upon Hydration and Doping. To explain the differences in ion uptake kinetics between P3MEEMT and P3HT, we next investigate how hydration and electrochemical doping influence the crystal structures of P3MEEMT and P3HT. The GIXRD pattern of P3MEEMT is very similar to that of P3HT (**Figure B.10**), yet P3MEEMT has a larger lamellar spacing (1.9 nm versus 1.6 nm) because of its slightly longer side chains. We observe a high degree of preferential orientation of P3MEEMT with the lamellar spacing occurring in the out-of-plane direction and π-π stacking occurring in the in-plane direction, which is similar to P3HT (**Figure B.11**). **Figure 3.3 A** shows how the lamellar spacing of P3MEEMT changes upon hydration and doping using GIXRD. The π-π stacking distance does not change significantly upon hydration (**Figure B.12**). This distance, however, decreases from 3.76 Å to 3.63 Å upon doping (**Figure B.13**), which is similar to changes observed in P3HT.[51,52] We note that the lattice expansion upon hydration is fully reversible, unlike in other systems where doping leads to irreversible structural changes (**Figure B.14**).[52] By measuring GIXRD patterns dry and in water, we quantify how much the lattice spacing of P3MEEMT changes upon hydration. We find a shift of the (100) peak of P3MEEMT to lower 2θ representing ~5% lattice expansion in water. We find a similar smaller shift (~2% lattice expansion) in dry P3MEEMT

upon electrochemical doping with PF_6^- (0.7 V). These shifts demonstrate that the lattice of P3MEEMT expands readily in solution to accommodate water and ions in the absence of an electrochemical bias. This 5% expansion in water is much larger than that required to accommodate the dopants without water present, demonstrating that the crystalline regions of P3MEEMT are hydrated in solution. We perform the same measurements on P3HT and find no change in the lamellar spacing in water, yet a significant shift of 7% in the (100) peak occurs upon electrochemical doping with PF_6^- (0.7 V) (**Figure 3.3 B**). The GIXRD data for P3HT suggests that the crystal lattice does not expand spontaneously in water and only expands upon electrochemical doping.

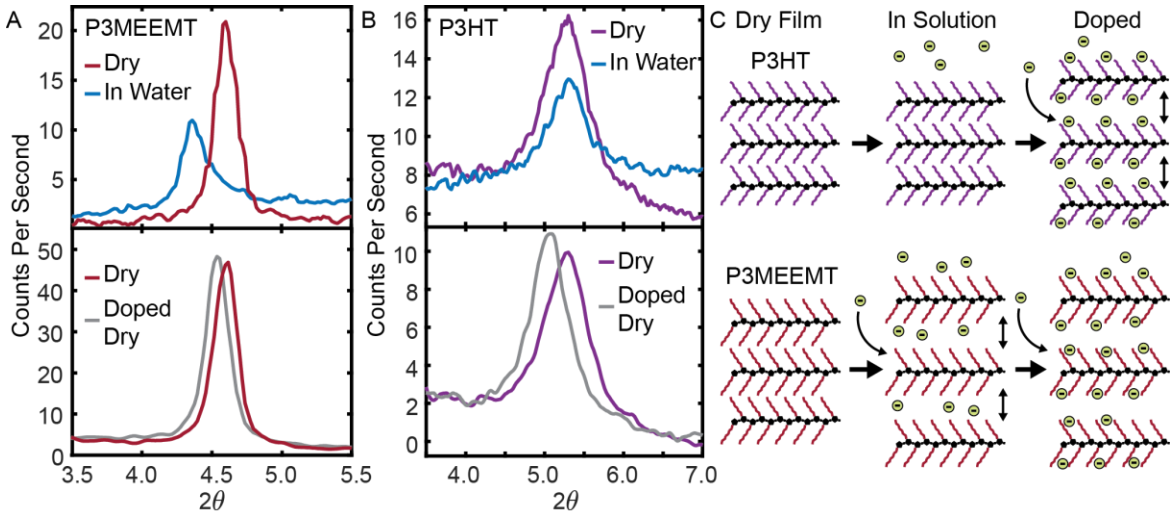

Figure 3.3 Grazing incidence X-ray diffraction (GIXRD) of P3MEEMT and P3HT. (A) GIXRD of P3MEEMT dry and in water (top) and dry after doping at 0.5 V in 100 mM KPF6 (bottom). (B) GIXRD of P3HT dry and in deionized water (top) and dry and doped at 0.5 V in 100 mM KPF6 (bottom). (C) Schematic depicting structural changes in P3HT and P3MEEMT in solution and upon electrochemical doping. P3MEEMT exhibits a lattice expansion in solution, whereas the P3HT lattice only expands upon electrochemical doping. The green circles with minus signs are the anions. Water molecules and cations are not shown for clarity.

The structural changes in P3MEEMT and P3HT explain the differences in doping kinetics. **Figure 3.3 C** shows a schematic of doping in crystalline regions of P3HT and P3MEEMT. In the case of P3HT, the crystal lattice spacing does not expand appreciably in solution, but expands by 7% along the (100) axis upon electrochemical doping. In contrast, P3MEEMT exhibits an

expansion of the crystal lattice by 5% when placed in solution, yet does not expand further to accommodate the anions when a voltage is applied. Because of the difference in structural changes between P3HT and P3MEEMT, we can now explain the difference in kinetics between the two polymers. We propose that P3HT exhibits slower charge injection kinetics because the anion must inject into the polymer from solution and displace the hydrophobic side-chains when a potential is applied. On the other hand, in P3MEEMT, the crystalline regions are hydrated and already contain solvated ions. Therefore, when the potential is turned on, ions are already nearby the polymer backbone and the lattice is already expanded, making the doping kinetics much faster. Additional anions can then easily enter the P3MEEMT film through expanded, hydrated ethylene glycol channels.

Controlling Crystallinity with Thermal Annealing. Having shown high volumetric capacitance in the ethylene glycol side chain polymer, we next thermally anneal P3MEEMT in an attempt to increase its mobility and, therefore, its μC* value. **Figure 3.4 A** shows the GIXRD spectra for P3MEEMT unannealed and annealed at three temperatures (125 °C, 145 °C, and 165 °C) for 20 min. As the annealing temperature increases, the degree of crystallinity increases, as demonstrated by the increase in intensity of the lamellar spacing (100) peak and (010) in-plane π-π stacking peak (**Figure B.15**). A Scherrer analysis of the GIXRD linewidths predict a mean size of the crystalline domains of 39 nm (± 2 nm) in the (100) direction and 6.2 nm (± 0.4 nm) in the (010) direction (**Figure B.16**). We measure the μC* for unannealed P3MEEMT and P3MEEMT annealed at three temperatures and find that it decreases with annealing temperature (**Figure 3.4 B**) from 52.9 ± 3.4 (F cm^{-1} V^{-1} s^{-1}) to 20.9 ± 1.1 (F cm^{-1} V^{-1} s^{-1}) in 100 mM KCl (μC* determination for each annealing temperature shown in **Figure B.17**). To investigate whether μ or C* changes most significantly with crystallinity, we measure the C* for each

sample with electrochemical impedance spectroscopy (EIS) with fits shown in **Figure B.18**. We observe little dependence of C* on crystallinity (**Figure 3.4 C**), which implies that the number of sites available to both electronic charges and dopant ions is equal in amorphous and crystalline regions of the film. The constant C* with annealing is consistent with our GIXRD results showing hydrated crystalline regions in P3MEEMT, and has been observed in other polymers as well.[53] Since C* does not change significantly with annealing, we conclude OECT mobility must decrease with increased crystallinity. We directly measure the carrier mobility using the impedance matching method,[54] and find the mobility in the linear regime for the unannealed polymer to be 0.19 ± 0.05 cm^2 V^{-1} s^{-1} and a mobility in the annealed polymer of 0.13 ± 0.04 cm^2 V^{-1} s^{-1}. In **Figure 3.4 D**, we estimate carrier mobility at each annealing temperature by dividing the μC* product by the C* obtained with EIS. In good agreement with the direct mobility measurement, we estimate the expected mobility of unannealed, amorphous P3MEEMT to be 0.19 ± 0.03 cm^2 V^{-1} s^{-1} and the annealed, most crystalline P3MEEMT to be 0.09 ± 0.01 cm^2 V^{-1} s^{-1}. To check that this decrease in the mobility did not originate from the PET substrate degrading during annealing, we measured annealed and unannealed OECTs on glass substrates and observed the same trend (**Figure B.19**). To investigate the origin of the decrease in mobility, we perform conductive atomic force microscopy (cAFM) measurements. As expected and in contradiction to our OECT mobility results, dry, crystalline P3MEEMT is ~10 times more conductive in the vertical direction than unannealed P3MEEMT in its undoped, dry state (**Figure B.20**). To further confirm the enhanced conductivity of dry crystalline P3MEEMT, we fabricated and tested organic field effect transistors (OFETs) and found a higher mobility in the annealed sample (**Figure B.21**). Although initially counterintuitive, this difference in OFET mobility and OECT mobility is similar to findings by Giovannitti et. al., in which the polymer with greater dry

field effect mobility and nearly equivalent volumetric capacitance performed significantly worse as an OECT.[36] Both of these experiments suggest that changes in the polymer in its hydrated or doped state can have a detrimental effect on electronic transport. Here, we speculate that the more crystalline polymer, while having a higher dry mobility is more susceptible to disruption of intergrain conductivity due to water uptake.

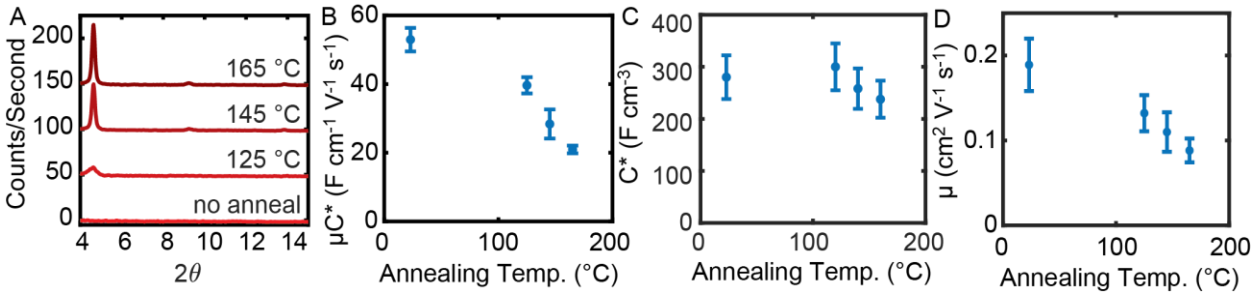

Figure 3.4 (A) GIXRD of polymer annealed at 4 temperatures showing increased crystallinity at higher temperature annealing, offset by 50 counts per second. (B) μC* product as a function of annealing temperature showing decreased value at increasing annealing temperature and crystallinity. (C) Volumetric capacitance as a function of annealing temperature showing that crystallinity has limited effect on capacitance in this polymer. (D) Electronic carrier mobility calculated by dividing the μC* product by the measured C*, showing a decreasing OECT mobility in more crystalline films.

Anion- and Crystallinity-Dependent Hydration. The difference in how the mobility scales with crystallinity in an OECT versus OFET could stem from the fact that OECTs operate in solution, while OFETs operate in a dry state. To investigate the role of polymer and dopant hydration in crystalline versus non-crystalline films of P3MEEMT we perform electrochemical quartz crystal microbalance measurements (EQCM). We measure both the unannealed P3MEEMT film and the most crystalline P3MEEMT film, annealed at 165 °C. First, we compare the initial hydration state without bias of the polymer films without bias and find by both QCM with dissipation monitoring (QCM-D) (**Figure B.22**) and AFM profilometery that the annealed film swells less in solution than the unannealed film (**Figure B.23**). Next, we apply a typical cyclic voltammetry (CV) bias sweep from 0.0 V to 0.7 V to -0.5 V versus Ag/AgCl

(shown in **Figure 3.5 A**). During the voltage sweeps, we record both the current (**Figure 3.5 B)** and frequency of the quartz oscillator, which we convert to a change in mass using the Sauerbrey equation (**Figure 3.5 C**).[55]

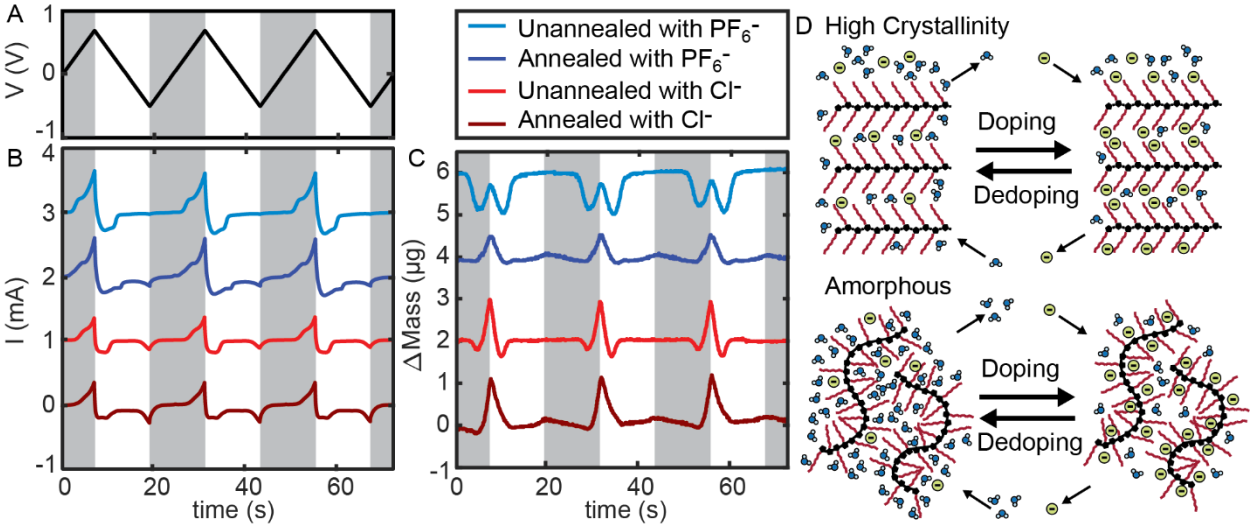

Figure 3.5 Electrochemical quartz crystal microbalance (E-QCM) measurement of annealed and unannealed P3MEEMT with 100 mM KCl and KPF6. (A) Voltage versus time plot from three consecutive cyclic voltammetry (CV) measurements. (B) Recorded current offset by 1 mA and (C) mass change offset by 2 μg during the CV measurements. (D) Schematic showing doping and dedoping of crystalline and amorphous P3MEEMT. The higher crystallinity case has fewer bound waters undoped and therefore expels fewer waters upon doping compared to the unannealed film. Grey shading indicates that the voltage is increasing.

We find that the shape of the current curves upon doping and dedoping is similar for all four cases. The total current is higher with PF_6^- rather than Cl^- as the anion, which is consistent with a higher threshold voltage for doping with Cl^-. We also see similar levels of charge injection for annealed and unannealed P3MEEMT with both anion, which is consistent with our earlier observation that C* does not depend on crystallinity for P3MEEMT.

Although the plots of current versus time do not change significantly with increased crystallinity, the plots of mass change versus time change dramatically. In unannealed P3MEEMT with PF_6^- as the dopant, we observe a significant initial decrease in the mass as the voltage increases and the film begins to dope, followed by a small increase in mass upon further

doping. As the voltage decreases, we observe a decrease in mass as the film dedopes and then a larger increase back to the initial mass, which we attribute to a rehydration of the film. We observe a similar shape in the change in mass versus time plot of unannealed P3MEEMT with Cl^- as the anion. For the unannealed films we observe a small decrease in mass followed by a large increase upon doping and a large decreases and then small increase in mass upon dedoping. We note that the observed decrease in mass upon doping in both cases could be cations and water leaving the film.[56,57]

The observed trends are explained in a schematic in **Figure 3.5 D**. In the annealed case, the P3MEEMT thin film swells moderately in solution and has some waters incorporated prior to biasing (**Figure B.24**). Therefore, the large increase in mass upon doping is associated with anion injection (Cl^- or PF_6^-) into the film. We note that in the mass increase region the apparent molar mass of the Cl^- dopant is 223 ± 13 g/mol, implying that Cl^- enters the polymer with a solvation shell of approximately 10 waters, while the molar mass of the PF_6^- dopant is less than the mass of a bare PF_6^-, implying more water is expelled from the film upon doping. (**Figure B.17**). In the unannealed case, the film swells much more in solution and has many waters incorporated initially. Upon applying a bias, more water leaves the film as the polymer is oxidized and doped by the anion. This picture is consistent with PF_6^- being a relatively hydrophobic and chaotropic ion: more waters leave the film upon PF_6^- injection, compared to Cl^- injection, which is more kosmotropic and binds more strongly to surrounding waters. This anion dependence is consistent with previous QCM studies on polyelectrolytes with multiple different ionic species.[58]

We have shown by QCM that there are major differences in how water interacts with the annealed and unannealed films, namely 1) much greater water uptake in the unannealed film

prior to doping and 2) significantly more water expulsion upon doping in the unannealed film. Despite having more water present, the more amorphous film demonstrates a higher OECT mobility. Based on our GIXRD data, we know that crystalline regions of the polymer swell in water, yet the π-π stacking distance does not change upon hydration. Therefore, changes in the amorphous regions that connect the crystalline regions or the changes in packing along the lamellar direction must be responsible for the decrease in mobility upon hydration of the film. To investigate this hypothesis, we next examine the nanoscale dopant distribution in crystalline and amorphous P3MEEMT with PiFM.[59]

PiFM of Crystalline and Amorphous P3MEEMT. To investigate the spatial distribution of dopants in amorphous and crystalline P3MEEMT, we perform PiFM on P3MEEMT films doped with PF_6^-. By detecting the P-F stretch as a function of spatial location in the film, we map the location of PF_6^- dopants with nanoscale spatial resolution. **Figure 3.6 A** shows the PiFM spectra of doped and undoped regions of a P3MEEMT film. Upon doping the film, the PiFM spectrum changes and a new peak we assign to the PF_6^- stretch appears at 843 cm^{-1}. The location of this peak, if not the lineshape,[60] is consistent with previous Fourier transform infrared (FTIR) spectroscopy and attenuated total reflectance (ATR) FTIR studies.[61] In addition to the emergence of the PF_6^- peak at 843 cm^{-1}, other changes in the PiFM spectrum result from doping the thiophene backbone.

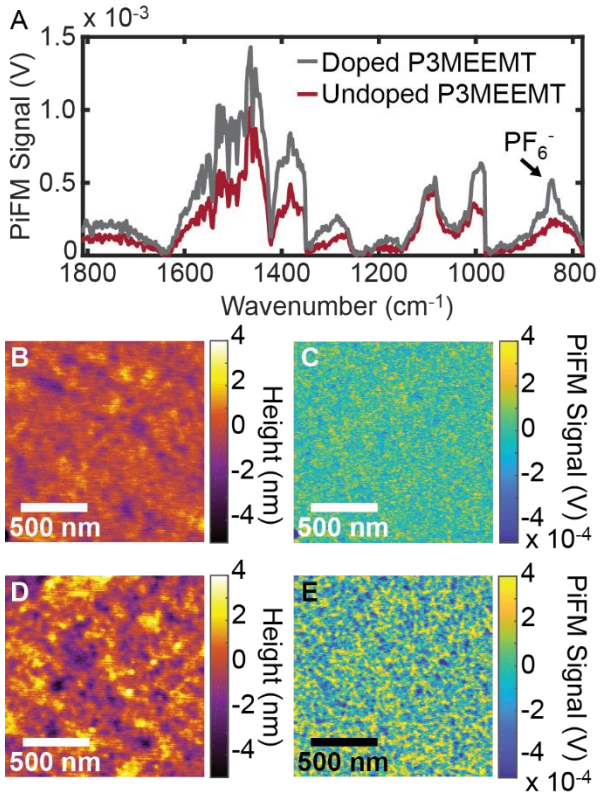

Figure 3.6 Photoinduced force microscopy (PiFM) of annealed and unannealed P3MEEMT thin films doped with PF6-. (A) PiFM spectrum of doped and undoped P3MEEMT showing the peak corresponding to the P-F stretch of PF6-. (B) Topography image of unannealed P3MEEMT doped with PF6-. (C) Flattened PiFM image of unannealed P3MEEMT doped with PF6-. (D) Topography image of annealed P3MEEMT doped with PF6-. (E) Flattened PiFM image of annealed P3MEEMT doped with PF_6^-.

We compare PiFM images of the P-F stretch of PF_6^- in crystalline and amorphous films of P3MEEMT. **Figure 3.6 B** and **Figure 3.6 C** show the topography and PiFM images of an unannealed, amorphous P3MEEMT thin film, respectively, whereas **Figure 3.6 D** and **Figure 3.6 E** show the topography and PiFM images of an annealed, crystalline P3MEEMT thin film, respectively. PiFM images of undoped films have no PiFM contrast and are shown in **Figure B.25**. The PiFM image of the amorphous P3MEEMT film shows a relatively homogenous distribution of dopants in the film with no distinct features. In contrast, the PiFM image of the annealed P3MEEMT film is much more heterogeneous and shows distinct features of higher PF_6^- anion concentration. A Fourier transform of this image shows characteristic feature sizes of ~ 40

nm in the annealed film, which demonstrates a heterogeneous distribution of the anions that we hypothesize leads to bottlenecks in charge transport (**Figure B.26).**

The heterogeneity in dopant concentration suggests that the film consists of small crystallites with a high anion concentration linked by lower density amorphous regions with a lower anion concentration. When submerged in an aqueous environment, we hypothesize that amorphous regions that link crystalline region swell significantly, disrupting electronic connectivity between the crystalline regions of the film. Such morphology could cause a disruption of electronic transport, similar to that seen as a function of molecular weight in P3HT where lower molecular weight polymers exhibit lower mobility despite being more crystalline.[62] This effect has been explained by the lack of "tie chains" that allow for intrachain connections between different crystallite domains.[63,64] This lack of tie chains was even observed as a function of annealing where annealing at higher temperatures resulted in decreasing carrier mobility.[65] If true, in the future it may be possible to control the morphology of films made from polymers like P3MEEMT (perhaps through molecular weight) to better preserve the mobility upon annealing.

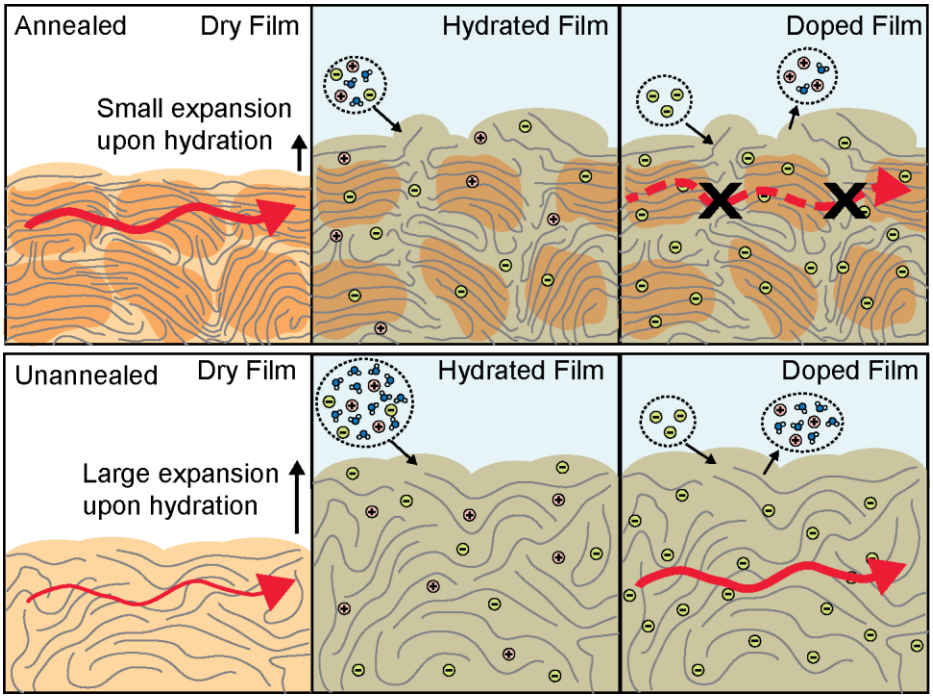

Figure 3.7 Schematic unifying the results from GIXRD, E-QCM, AFM, EIS, OFET, OECT, and mobility measurements on annealed and unannealed P3MEEMT. The red arrows indicate charge carrier migration through the film. In the dry state, the annealed film is more crystalline and has a higher mobility compared to the unannealed sample. When hydrated, the unannealed film swells more and uptakes more electrolyte solution. The annealed sample swells in both crystalline and amorphous regions. Upon electrochemical doping, a similar number of charges per volume dope both samples. The unannealed sample loses more waters/cations and has a higher mobility than the annealed sample. We attribute this lower mobility in the annealed P3MEEMT to a heterogeneity in film swelling. Amorphous regions between the crystalline regions swell more, disconnecting crystalline regions of the film.

We summarize our comparison of annealed and unannealed P3MEEMT in **Figure 3.7**. In the dry state, GIXRD shows that the annealed P3MEEMT films is more crystalline than the unannealed film and OFET measurements demonstrate that the annealed film has a higher mobility. When the film is hydrated, the unannealed film expands more, as shown with AFM profilometery of the hydrated samples, and QCM data shows that the unannealed film uptakes more waters. GIXRD of the annealed film shows that crystalline regions of the film also expand when hydrated. Upon electrochemical doping, EIS data shows that a similar number of charges dope the annealed and unannealed films. Furthermore, E-QCM shows that the unannealed film loses more waters upon electrochemical doping than the annealed sample, and mobility and OECT measurements show a higher mobility in the unannealed film than the annealed film. We hypothesize that the change in mobility stems from the effect of water intercalation on the electronic connectivity of the polymer film. In the case of the annealed film, we attribute the change in mobility to the swelling of amorphous regions that connect the crystalline regions of the film. When the film is hydrated, this heterogeneity in swelling prevents charge carriers from moving as easily between the crystalline regions of the film.

3.3 CONCLUSIONS

Our comparative study of P3MEEMT and P3HT highlights the importance of the anion in many aspects of OECT operation. First, larger, more hydrophobic anions shift the threshold voltage in OECT active layer polymers with both hydrophilic and hydrophobic sidechains, which

indicates that this anion-dependent threshold voltage shift is a general principle of OECT operation. Larger, chaotropic ions with a smaller surface charge density, like PF_6^-, can more easily inject into the active layer polymer than smaller, kosmotropic ions with high surface charge densities, like Cl^-, regardless of the side chain functionality. Second, our E-QCM data show that the anion has a significant impact on polymer hydration upon doping. Compared to doping with Cl^-, electrochemically doping the polymer with PF_6^- expels more water from the polymer active layer. Therefore, the choice of anion could have a profound effect on the packing density and molecular-level organization upon doping.

We additionally demonstrate that P3MEEMT, a polythiophene derivative with ethylene glycol-based side chains, is a promising OECT active layer material for accumulation mode transistors with a μC* that rivals state-of-the-art OECT materials. We observe faster doping kinetics in P3MEEMT than in P3HT, which stems from structural changes in P3MEEMT upon hydration. The crystalline lattice of P3MEEMT expands in solution, allowing ions to access even densely-packed crystalline regions of the film. In comparison, the P3HT lattice only expands upon electrochemical doping, requiring the anions to displace alkyl side chains, and thus slowing down ion injection kinetics compared to those of P3MEEMT.

By increasing the crystallinity of P3MEEMT, we demonstrate that OECT mobility decreases, whereas OFET mobility increases. We explain this difference by investigating the role of water in both amorphous and crystalline P3MEEMT. We find that crystalline and amorphous P3MEEMT have very different hydration dynamics upon electrochemical doping. We hypothesize that the hydration of the film disrupts the regions that link crystalline domains, thereby significantly decreasing the mobility in crystalline P3MEEMT. This hypothesis is supported by PiFM imaging, which maps the presence of anion within the film and reveals a

large degree of dopant heterogeneity in crystalline P3MEEMT compared to amorphous P3MEEMT.

Our data demonstrates that the presence of water can be a double-edged sword for OECT operation that must be considered when designing new active layers for efficient OECTs. Readily hydrated crystal lattices can facilitate ion transport, allowing for faster anion injection kinetics and better access for anion into tightly-packed crystalline regions. Yet, polymer hydration can also interrupt the connectivity between crystalline regions of the polymer, significantly decreasing the charge-carrier mobility. Because of the presence of water, many of the design principles established over the last thirty years to optimize OFETs must be adapted before applying them to OECTs. Overall, our data paints a complex picture of how operating in solution and relying on anion intercalation impacts the design principles for highly efficient OECTs. The complex interplay between ion transport, charge transport, side chain chemistry, steady-state hydration, and hydration dynamics upon electrochemical doping have a profound impact on OECT operation. By understanding these challenges, it may be possible to tailor the morphology of future OECT materials so that they benefit from improved order in the same way that OFET performance improves with increased polymer crystallinity. For high C* polymers, improving the electronic carrier mobility by an order of magnitude, the same amount that FET mobility can be improved by annealing, would provide a clear path to achieving μC* products of 3000 F cm^{-1} V^{-1} s^{-1}. Such a material would prove invaluable for the growing number of applications that rely on efficient mixed electronic/ionic conduction.

3.4 METHODS

Materials. P3HT (Ossila Ltd), chlorobenzene (Aldrich), KPF6 (Aldrich), KCl (Aldrich), ferrocene (Aldrich). N-bromosuccinimide (NBS) was purchased from Sigma-Aldrich and

recrystallized from water before use. Diethylene glycol monomethyl ether was purchased from Sigma-Aldrich and distilled onto freshly activated molecular sieves before use. Anhydrous solvents were used for all reactions. THF was dried using a PureSolv solvent purification system. Dichloromethane (DCM) (Aldrich) was dried using an SP-1 Stand Alone Solvent Purification System. All other reagents were purchased from Sigma-Aldrich and used as received.

Polymer synthesis and characterization. All reactions were performed under air-free conditions using standard Schlenk techniques. All reaction glassware was dried overnight in an oven at 120 °C prior to use. 2,5-dibromo-3-methoxyethoxyethoxymethylthiophene was synthesized according to modified literature procedures.1 Following monomer synthesis, P3MEEMT was synthesized using Kumada Catalyst Transfer Polymerization (KCTP). The produced polymer was characterized via size-exclusion chromatography (SEC), using a Malvern Viscotek TDA 305 GPC equipped with a UV detector. CHCl3 was used as an eluent at a temperature of 30 °C and a flow rate of 1 mL/min. Molecular weight information was determined relative to polystyrene standards. 1H NMR was performed using either a 300 MHz Bruker AV-300 or a 500 MHz Bruker AV-500 instrument at 25 °C.

2,5-dibromo-3-thiophenemethanol Synthesis

To a 3-neck flask 3-thiophenemethanol (3.77 mL, 40 mmol) and 36.4 mL THF was added. The solution was degassed with nitrogen bubbling for 15 minutes. Following bubbling, recrystallized NBS (total: 14.15 g, 79.5 mmol) was added to the reaction in 5 equal portions. The reaction was then stirred overnight at room temperature. The reaction was then filtered, and THF was removed using rotary evaporation. The residue was then purified using column chromatography

with a 4:1 ratio of hexanes to ethyl acetate, resulting in a white solid in 90% yield. 1H NMR (300 MHz, CDCl3): δ 7.03 (s, 1H), 4.60 (s, 2H), and 1.95 (br, 1H).

2,5-dibromo-3-thiophenemethylbromide Synthesis

To a round-bottom flask, 2,5-dibromo-3-thiophenemethanol (9.0 g, 33.5 mmol) and 165 mL of DCM was added. The flask was cooled to 0 °C for 20 min, then PBr3 (3.20 mL, 34.25 mmol) was added dropwise over 15 min. The reaction was then stirred for 5 h at room temperature. The reaction was quenched with the addition of 100 mL of 10% NaHCO3 solution. The product was extracted with DCM, washed with brine, dried with MgSO4 and filtered. The solvent was then removed, and the product was stored at -20 C overnight, after which a white solid was collected in 93% yield. 1H NMR (300 MHz, CDCl3): δ 7.00 (s, 1H), 4.36 (s, 2H).

2,5-dibromo-3-[2-(2-methoxyethoxy)ethoxymethyl]thiophene Synthesis

Diethylene glycol monomethyl ether (3.5 mL, 30 mmol) and 100 mL of THF were added to a 3-neck flask equipped with an addition funnel. NaH (1.32 g, 33 mmol) was added quickly in one portion allowed to react for 10 min. 2,5-dibromo-3-thiophenemethylbromide (9.65 g, 29 mmol) was dissolved in 25 mL of THF, then added to the addition funnel, from which it was added dropwise over a period of 15 min. The reaction was stirred at room temperature overnight. The reaction mixture was filtered over Celite and the product washed through with THF. Solvent was removed using rotary evaporation, and the residue purified via column chromatography in a 3:2 mixture of hexanes to ethyl acetate. The product was collected in 87% yield as a pale yellow oil. The product was stored at -20 °C away from light. 1H NMR (300 MHz, CDCl3) δ 7.0 (s, 1H), 4.43 (s, 2H), 3.65 (m, 6H), 3.57 (m, 2H), 3.39 (s, 3H).

P3MEEMT Polymerization and Characterization

To a Schlenk flask, 2,5-dibromo-3-[2-(2-methoxyethoxy)ethoxymethyl]thiophene (0.37 g, 1.0 mmol) was added, then degassed under high-vacuum for 30 min. The flask was placed under nitrogen, and 10 mL of THF was added. The flask was cooled to 0 °C, and i-PrMgCl (2.0 M in THF, 0.5 mL, 1.0 mmol) was added dropwise over 10 min. The flask was allowed to warm to room temperature, then stirred for 1 h. The flask was then heated to 45 °C, and Ni(dppp)Cl2 (4.334 mg, 0.008 mmol) was added in one portion. The polymerization was stirred at 45 °C for 2 h, then quenched with 1 mL of 5 M HCl. The polymer was precipitated into 400 mL of MeOH and poured over a filter to collect. The polymer was purified with successive Soxhlet extractions using hexanes then MeOH and collected using CHCl3. The polymer was again precipitated into MeOH, filtered, and dried overnight in a vacuum oven. 1H NMR (500 MHz, CDCl3) δ 7.25 (s, 1H), 4.67 (s, 2H), 3.75 (s, 4H), 3.67 (m, 2H), 3.57 (m, 2H), 3.37 (s, 3H). Đ = 2.0, Mn = 11 kg/mol.

Sample Preparation. For all following experiments, polymers were dissolved at a concentration of 20 mg/mL in chlorobenzene overnight and stirred at 50 °C. Solutions were then spin coated onto substrates at 1000 rpm RPM for 60 seconds. Subsequent annealing (if any) was performed in a nitrogen environment. All electrolytes were made with degassed Milli-Q water.

OECT device fabrication and measurement. OECT substrates are comprised of polyethyelene terephthalate (PET) substrates with lithographically-patterned gold (Nano Terra Inc.) to have a length of 20 µm and a width between 50 and 2000 µm. A P3HT or P3MEEMT layer is spin-coated onto the OECT substrate (thickness between 70 and 150 nm) and removed from all regions except for at the electrode junctions. A nitrocellulose layer (Sally Hansen, Insta-Dri Top

Coat) is then applied to the exposed electrodes to insulate the electrodes from the electrolyte. Devices are measured in degassed 100 mM solution of KPF6 or KCl. Transfer curves were taken by varying VG from -0.7 to 0.4 V vs. Ag/AgCl with a fixed VDS of -0.6 V and a step size of 0.05 V with 10 seconds between each step using two Keithley source measure units and custom Labview software. All devices were cycles 3 times prior to measurement for reproducibility. Threshold voltage was calculated by extracting the x-intercept of the linear fit of the sqrt(IDS) vs VG plots. Mobility was measured using the impedance matching method previously reported.2 Briefly, a DC gate voltage offset is applied along with a sinusoidal gate voltage wave (10 mV). The resulting gate and drain current transients are recorded to extract the amplitude and phase shift of the resulting sine waves. Matching the gate and drain current impedances yields the hole/electron transit time in the channel (τe) by the following relation in the frequency (f) domain: $\Delta I_G(f) = 2\pi f \tau_e \ \Delta I_D(f)$. The OECT mobility (μ) can then be estimated from the hole/electron transit time in the channel by the equation $\mu = \frac{L^2}{\tau_e V_D}$ where L is the channel length and VD is the drain voltage.

OFET device fabrication and measurement. OFETs were fabricated in back-gate, top-contact geometry, using a doped p-type silicon <100> wafer with a 300 nm thick thermal oxide layer (University Wafer Inc.). P3MEEMT was spin coated onto the substrates as described above. Gold source and drain electrodes with (thickness = 50 nm) of gold were thermally evaporated onto the samples with a width of 1000 μm and a length of 10 μm. Transistors were tested in a nitrogen atmosphere using an HP 4145B Semiconductor Parameter Analyzer and custom LabVIEW acquisition software.

Ion injection kinetics spectroelectrochemistry and cyclic voltammetry (CV). Ion injection kinetics were measured with a MetroOhm Autolab PGSTAT204 with NOVA Software (version 2.1) and an Agilent 8453 spectrometer. P3MEEMT was spin-coated onto fluoride-doped tin oxide-coated glass (FTO, Sigma-Aldrich, 7 Ω/sq). The film substrate was used as the working electrode and was submerged in a cuvette containing degassed 100 mM KPF6 or 100 mM KCl. A Pt wire was used as the counter electrode (Aldrich) and an Ag/AgCl electrode (eDAQ) was used as the reference electrode. UV-Vis measurements were collected with an integration time of 0.1 s/spectrum or 0.5 s/spectrum as the film was electrochemically doped. CVs were performed at a scan rate of 100 ms/step for 0.01 V steps. pH was measured with a Veernier pH sensor.

Grazing Incidence X-ray diffraction (XRD). GIXRD of thin films of P3HT and P3MEEMT on ITO/glass or glass substrates were measured using a Bruker D8 Discover with a Pilatus 100K large-area 2D detector (Cu Kα radiation at 50000 mW). For measuring samples in water, 10 µL of deionized water was pipetted onto the sample and then covered with a thin layer of polyimide film (~25 µm). The electrochemically doped samples were measured dry. To prepare the electrochemically-doped samples, thin films on ITO/glass were electrochemically doped in 100 mM KPF6 or KCl at 0.5 or 0.7 V, rinsed with deionized water, and dried with N2 prior to measuring. For in-plane scans, the polymer was drop cast on a Si substrate or Si coated with 50 nm Au and the 2θ scan was acquired at psi = 70°. 1D data in- and out-of-plane was obtained through a polar integration of the acquired 2D data (Figures B10-16).

Electrochemical impedance spectroscopy for C* determination (EIS). EIS measurements were performed on gold-coated glass substrates with a defined area of 0.0015 cm2 with a DC offset of

0.1-0.7 V. Capacitance was determined using $C \sim 1/(2\pi f \mathrm{Im}(Z))$, where f is the frequency and Z is the complex impedance, and calculated based on a fit to Randles circuit R(R||C). Fitting was performed with the Metrohm NOVA software.

Electrochemical quartz crystal microbalance (E-QCM) Electrogravimetric measurements were performed using a QCM200 (Stanford Research Systems) on 5 MHz gold-coated AT quartz crystals. Biases were applied with a potentiostat (MetroOhm Autolab PGSTAT204) in a three-electrode cell, with the polymer coated crystal face as the working electrode, a platinum wire counter electrode, and a Ag/AgCl pellet electrode as the reference electrode. The change in frequency was converted to a change in mass using the Sauerbrey equation, which assumes a rigid film.

Quartz crystal microbalance with dissipative monitoring (QCM-D). QCM-D measurements were performed using a Q-sense analyzer (QE401, Biolin Scientific AB, Sweden). For the hydrated measurements, degassed 100 mM KCl solution was pumped over the surface of the polymer at a rate of 100 µL min-1.

Conductive atomic force microscopy (cAFM) and AFM step height measurements. cAFM and AFM step height measurements were performed on an Asylum Research Cypher-ES instrument. cAFM measurements used a gold-coated contact mode AFM probes (Budget Sensors, ContGB-G) in a nitrogen environment. A -500 mV bias was applied to the tip and current was collected as the tip was scanned across the surface. AFM step height measurements used 75 kHz

HQ:NSC18/Pt MikroMasch tips with 100 µl of Milli-Q water pipetted on the sample for hydrated film heights.

Photoinduced force microscopy (PiFM). PiFM images were acquired with a Molecular Vista Vistascope coupled to a LaserTune QCL operating in sideband mode using 325 kHz HQ:NSC15/Pt MikroMasch tips. Images of the P-F stretching mode of the PF6- counterions were collected with the laser tuned to 843 cm-1 at 1 s/line at 256 x 256 pixel with a field-of-view of 1.5 x 1.5 µm. PiFM spectra were acquired on doped and undoped regions of dry P3MEEMT films with a 10 s integration time.

3.5 Acknowledgements

This paper is based primarily on work supported by the National Science Foundation, NSF DMR-1607242, as well as through NSF DMREF Award Number 1629369. C. G. B. is a Washington Research Foundation Postdoctoral Fellow. The authors would like to acknowledge Franziska E. Muckel for assistance with OFET fabrication, Jonathan Rivnay for assistance with mobility measurement, and Rajiv Giridharagopal for fruitful discussions. Part of this work was conducted at the Molecular Analysis Facility, a National Nanotechnology Coordinated Infrastructure site at the University of Washington that is supported in part by the National Science Foundation (grant ECC-1542101), the University of Washington, the Molecular Engineering & Sciences Institute, the Clean Energy Institute and the National Institutes of Health.

3.6 References

(1) Inal, S.; Rivnay, J.; Suiu, A. O.; Malliaras, G. G.; McCulloch, I. Conjugated Polymers in Bioelectronics. *Acc. Chem. Res.* **2018**, *51*, 1368–1376. https://doi.org/10.1021/acs.accounts.7b00624.

(2) Someya, T.; Bao, Z.; Malliaras, G. G. The Rise of Plastic Bioelectronics. *Nature* **2016**, *540*, 379–385. https://doi.org/10.1038/nature21004.
(3) Rivnay, J.; Owens, R. M.; Malliaras, G. G. The Rise of Organic Bioelectronics. *Chem. Mater.* **2014**, *26*, 679–685. https://doi.org/10.1021/cm4022003.
(4) Arbring Sjöström, T.; Berggren, M.; Gabrielsson, E. O.; Janson, P.; Poxson, D. J.; Seitanidou, M.; Simon, D. T. A Decade of Iontronic Delivery Devices. *Adv. Mater. Technol.* **2018**, *3*, 1700360. https://doi.org/10.1002/admt.201700360.
(5) Smela, E. Conjugated Polymer Actuators for Biomedical Applications. *Adv. Mater.* **2003**, *15*, 481–494. https://doi.org/10.1002/adma.200390113.
(6) Wang, H.; Ail, U.; Gabrielsson, R.; Berggren, M.; Crispin, X. Ionic Seebeck Effect in Conducting Polymers. *Adv. Energ* **2015**, *5*, 1500044. https://doi.org/10.1002/aenm.201500044.
(7) Ponder, J. F.; Österholm, A. M.; Reynolds, J. R. Conjugated Polyelectrolytes as Water Processable Precursors to Aqueous Compatible Redox Active Polymers for Diverse Applications: Electrochromism, Charge Storage, and Biocompatible Organic Electronics. *Chem. Mater.* **2017**, *29* (10), 4385–4392. https://doi.org/10.1021/acs.chemmater.7b00808.
(8) Savagian, L. R.; Österholm, A. M.; Shen, D. E.; Christiansen, D. T.; Kuepfert, M.; Reynolds, J. R. Conjugated Polymer Blends for High Contrast Black-to-Transmissive Electrochromism. *Adv. Opt. Mater.* **2018**, *6*, 1800594. https://doi.org/10.1002/adom.201800594.
(9) Österholm, A. M.; Ponder, J. F.; Kerszulis, J. A.; Reynolds, J. R. Solution Processed PEDOT Analogues in Electrochemical Supercapacitors. *ACS Appl. Mater. Interfaces* **2016**, *8*, 13492–13498. https://doi.org/10.1021/acsami.6b02434.
(10) Zhou, Y.; Xu, H.; Lachman, N.; Ghaffari, M.; Wu, S.; Liu, Y.; Ugur, A.; Gleason, K. K.; Wardle, B. L.; Zhang, Q. M. Advanced Asymmetric Supercapacitor Based on Conducting Polymer and Aligned Carbon Nanotubes with Controlled Nanomorphology. *Nano Energy* **2014**, *9*, 176–185. https://doi.org/10.1016/j.nanoen.2014.07.007.
(11) Malti, A.; Edberg, J.; Granberg, H.; Khan, Z. U.; Andreasen, J. W.; Liu, X.; Zhao, D.; Zhang, H.; Yao, Y.; Brill, J. W.; Engquist, I. An Organic Mixed Ion – Electron Conductor for Power Electronics. *Adv. Sci.* **2016**, *3*, 1500305. https://doi.org/10.1002/advs.201500305.
(12) Burgt, Y. van de; Lubberman, E.; Fuller, E. J.; Keene, S. T.; Faria, G. C.; Agarwal, S.; Marinella, M. J.; Talin, A. A.; Salleo, A. A Non-Volatile Organic Electrochemical Device as a Low-Voltage Artificial Synapse for Neuromorphic Computing. *Nat. Mater.* **2017**, *16*, 414–419. https://doi.org/10.1038/nmat4856.
(13) Sun, H.; Vagin, M.; Wang, S.; Crispin, X.; Forchheimer, R.; Berggren, M.; Fabiano, S. Complementary Logic Circuits Based on High-Performance n-Type Organic Electrochemical Transistors. *Adv. Mater.* **2018**, *30*, 1704916. https://doi.org/10.1002/adma.201704916.
(14) Williamson, A.; Rivnay, J.; Kergoat, L.; Jonsson, A.; Inal, S.; Uguz, I.; Ferro, M.; Ivanov, A.; Sjöström, T. A.; Simon, D. T.; Berggren, M.; Malliaras, G. G.; Bernard, C. Controlling Epileptiform Activity with Organic Electronic Ion Pumps. *Adv. Mater.* **2015**, *27*, 3138–3144. https://doi.org/10.1002/adma.201500482.
(15) Uguz, I.; Proctor, C. M.; Curto, V. F.; Pappa, A. M.; Donahue, M. J.; Ferro, M.; Owens, R. M.; Khodagholy, D.; Inal, S.; Malliaras, G. G. A Microfluidic Ion Pump for In Vivo Drug Delivery. *Adv. Mater.* **2017**, *29*, 1701217. https://doi.org/10.1002/adma.201701217.

(16) Wustoni, S.; Savva, A.; Sun, R.; Bihar, E.; Inal, S. Enzyme-Free Detection of Glucose with a Hybrid Conductive Gel Electrode. *Adv. Mater. Interfaces* **2018**, *6*, 1800928. https://doi.org/10.1002/admi.201800928.
(17) Macchia, E.; Romele, P.; Manoli, K.; Ghittorelli, M.; Magliulo, M.; Kovács-Vajna, Z. M.; Torricelli, F.; Torsi, L. Ultra-Sensitive Protein Detection with Organic Electrochemical Transistors Printed on Plastic Substrates. *Flex. Print. Electron.* **2018**, *3*, 034002. https://doi.org/10.1088/2058-8585/aad0cb.
(18) Pappa, A.-M. M.; Ohayon, D.; Giovannitti, A.; Maria, I. P.; Savva, A.; Uguz, I.; Rivnay, J.; McCulloch, I.; Owens, R. M. R.; Inal, S. Direct Metabolite Detection with an N-Type Accumulation Mode Organic Electrochemical Transistor. *Sci. Adv.* **2018**, *4*, eaat0911. https://doi.org/10.1126/sciadv.aat0911.
(19) Khodagholy, D.; Doublet, T.; Quilichini, P.; Gurfinkel, M.; Leleux, P.; Ghestem, A.; Ismailova, E.; Hervé, T.; Sanaur, S.; Bernard, C.; Malliaras, G. G. In Vivo Recordings of Brain Activity Using Organic Transistors. *Nat. Commun.* **2013**, *4*, 1575. https://doi.org/10.1038/ncomms2573.
(20) Rivnay, J.; Inal, S.; Salleo, A.; Owens, R. M.; Berggren, M.; Malliaras, G. G. Organic Electrochemical Transistors. *Nat. Rev. Mater.* **2018**, *3*, 17086. https://doi.org/10.1038/natrevmats.2017.86.
(21) White, H. S.; Kittlesen, G. P.; Wrighton, M. S. Chemical Derivatization of an Array of Three Gold Microelectrodes with Polypyrrole: Fabrication of a Molecule-Based Transistor. *J. Am. Chem. Soc.* **1984**, *106*, 5375–5377. https://doi.org/10.1021/ja00330a070.
(22) Strakosas, X.; Bongo, M.; Owens, R. M. The Organic Electrochemical Transistor for Biological Applications. *J. Appl. Polym. Sci.* **2015**, *132*, 1–14. https://doi.org/10.1002/app.41735.
(23) Inal, S.; Malliaras, G. G.; Rivnay, J. Benchmarking Organic Mixed Conductors for Transistors. *Nat. Commun.* **2017**, *8*, 1767. https://doi.org/10.1038/s41467-017-01812-w.
(24) Stavrinidou, E.; Leleux, P.; Rajaona, H.; Khodagholy, D.; Rivnay, J.; Lindau, M.; Sanaur, S.; Malliaras, G. G. Direct Measurement of Ion Mobility in a Conducting Polymer. *Adv. Mater.* **2013**, *25*, 4488–4493. https://doi.org/10.1002/adma.201301240.
(25) Rivnay, J.; Inal, S.; Collins, B. A.; Sessolo, M.; Stavrinidou, E.; Strakosas, X.; Tassone, C.; Delongchamp, D. M.; Malliaras, G. G. Structural Control of Mixed Ionic and Electronic Transport in Conducting Polymers. *Nat. Commun.* **2016**, *7*, 11287. https://doi.org/10.1038/ncomms11287.
(26) Inal, S.; Rivnay, J.; Leleux, P.; Ferro, M.; Ramuz, M.; Brendel, J. C.; Schmidt, M. M.; Thelakkat, M.; Malliaras, G. G. A High Transconductance Accumulation Mode Electrochemical Transistor. *Adv. Mater.* **2014**, *26*, 7450–7455. https://doi.org/10.1002/adma.201403150.
(27) Tseng, H. R.; Phan, H.; Luo, C.; Wang, M.; Perez, L. A.; Patel, S. N.; Ying, L.; Kramer, E. J.; Nguyen, T. Q.; Bazan, G. C.; Heeger, A. J. High-Mobility Field-Effect Transistors Fabricated with Macroscopic Aligned Semiconducting Polymers. *Adv. Mater.* **2014**, *26*, 2993–2998. https://doi.org/10.1002/adma.201305084.
(28) Giridharagopal, R.; Flagg, L. Q.; Harrison, J. S.; Ziffer, M. E.; Onorato, J.; Luscombe, C. K.; Ginger, D. S. Electrochemical Strain Microscopy Probes Morphology-Induced Variations in Ion Uptake and Performance in Organic Electrochemical Transistors. *Nat. Mater.* **2017**, *16*, 737–742. https://doi.org/10.1038/nmat4918.

(29) Giovannitti, A.; Sbircea, D.-T.; Inal, S.; Nielsen, C. B.; Bandiello, E.; Hanifi, D. A.; Sessolo, M.; Malliaras, G. G.; McCulloch, I.; Rivnay, J. Controlling the Mode of Operation of Organic Transistors through Side-Chain Engineering. *Proc. Natl. Acad. Sci.* **2016**, *113*, 12017–12022. https://doi.org/10.1073/pnas.1608780113.

(30) Laiho, A.; Herlogsson, L.; Forchheimer, R.; Crispin, X.; Berggren, M. Controlling the Dimensionality of Charge Transport in Organic Thin-Film Transistors. *PNAS* **2011**, *108*, 15069–15073. https://doi.org/10.1073/pnas.1107063108.

(31) Toss, H.; Suspène, C.; Piro, B.; Yassar, A.; Crispin, X.; Kergoat, L.; Pham, M. C.; Berggren, M. On the Mode of Operation in Electrolyte-Gated Thin Film Transistors Based on Different Substituted Polythiophenes. *Org. Electron. physics, Mater. Appl.* **2014**, *15*, 2420–2427. https://doi.org/10.1016/j.orgel.2014.06.017.

(32) Pacheco-Moreno, C. M.; Schreck, M.; Scaccabarozzi, A. D.; Bourgun, P.; Wantz, G.; Stevens, M. M.; Dautel, O. J.; Stingelin, N. The Importance of Materials Design to Make Ions Flow: Toward Novel Materials Platforms for Bioelectronics Applications. *Adv. Mater.* **2017**, *29*, 1604446. https://doi.org/10.1002/adma.201604446.

(33) Nielsen, C. B.; Giovannitti, A.; Sbircea, D. T.; Bandiello, E.; Niazi, M. R.; Hanifi, D. A.; Sessolo, M.; Amassian, A.; Malliaras, G. G.; Rivnay, J.; McCulloch, I. Molecular Design of Semiconducting Polymers for High-Performance Organic Electrochemical Transistors. *J. Am. Chem. Soc.* **2016**, *138*, 10252–10259. https://doi.org/10.1021/jacs.6b05280.

(34) Giovannitti, A.; Thorley, K. J.; Nielsen, C. B.; Li, J.; Donahue, M. J.; Malliaras, G. G.; Rivnay, J.; McCulloch, I. Redox-Stability of Alkoxy-BDT Copolymers and Their Use for Organic Bioelectronic Devices. *Adv. Funct. Mater.* **2018**, *28*, 1706325. https://doi.org/10.1002/adfm.201706325.

(35) Savagian, L. R.; Österholm, A. M.; Ponder, J. F.; Barth, K. J.; Rivnay, J.; Reynolds, J. R. Balancing Charge Storage and Mobility in an Oligo(Ether) Functionalized Dioxythiophene Copolymer for Organic- and Aqueous- Based Electrochemical Devices and Transistors. *Adv. Mater.* **2018**, *30*, 1804647. https://doi.org/10.1002/adma.201804647.

(36) Giovannitti, A.; Nielsen, C. B.; Sbircea, D.-T.; Inal, S.; Donahue, M.; Niazi, M. R.; Hanifi, D. A.; Amassian, A.; Malliaras, G. G.; Rivnay, J.; McCulloch, I. Erratum: N-Type Organic Electrochemical Transistors with Stability in Water. *Nat. Commun.* **2016**, *7*, 13955. https://doi.org/10.1038/ncomms13955.

(37) Giovannitti, A.; Maria, I. P.; Hanifi, D.; Donahue, M. J.; Bryant, D.; Barth, K. J.; Makdah, B. E.; Savva, A.; Moia, D.; Zetek, M.; Barnes, P. R. F.; Reid, O. G.; Inal, S.; Rumbles, G.; Malliaras, G. G.; Nelson, J.; Rivnay, J.; McCulloch, I. Role of the Side Chain on the Performance of N-Type Conjugated Polymers in Aqueous Electrolytes. *Chem. Mater.* **2018**, *30*, 2945–2953. https://doi.org/10.1021/acs.chemmater.8b00321.

(38) Peng, C.; Zhou, X.; Chen, G. Z.; Moggia, F.; Fages, F.; Brisset, H.; Roncali, J. Internally Referenced Analysis of Charge-Transfer Reactions in a New Ferrocenyl Bithiophenic Conducting Polymer through Cyclic Voltammetry. *Chem. Commun.* **2008**, *48*, 6606–6608. https://doi.org/10.1039/b817101g.

(39) Proctor, C. M.; Rivnay, J.; Malliaras, G. G. Understanding Volumetric Capacitance in Conducting Polymers. *J. Polym. Sci. Part B Polym. Phys.* **2016**, *54*, 1433–1436. https://doi.org/10.1002/polb.24038.

(40) Sun, H.; Gerasimov, J.; Berggren, M.; Fabiano, S. N-Type Organic Electrochemical Transistors: Materials and Challenges. *J. Mater. Chem. C* **2018**, *6*, 11778–11784. https://doi.org/10.1039/C8TC03185A.

(41) Paterson, A. F.; Singh, S.; Fallon, K. J.; Hodsden, T.; Han, Y.; Schroeder, B. C.; Bronstein, H.; Heeney, M.; McCulloch, I.; Anthopoulos, T. D. Recent Progress in High-Mobility Organic Transistors: A Reality Check. *Adv. Mater.* **2018**, *30*, 1801079. https://doi.org/10.1002/adma.201801079.
(42) Cho, S.; Lee, K.; Yuen, J.; Wang, G.; Moses, D.; Heeger, A. J.; Surin, M.; Lazzaroni, R.; Yuen, J.; Wang, G.; Moses, D.; Heeger, A. J. Poly (3-Hexylthiophene) Films Thermal Annealing-Induced Enhancement of the Field-Effect Mobility of Regioregular Poly (3-Hexylthiophene) Films. *J. Appl. Phys.* **2006**, *100*, 114503. https://doi.org/10.1063/1.2400796.
(43) Sirringhaus, H.; Brown, P. J.; Friend, R. H.; Nielsen, M. M.; Bechgaard, K.; Spiering, A. J. H. Two-Dimensional Charge Transport in Conjugated Polymers. *Nature* **1999**, *401*, 685–688.
(44) Nielsen, C. B.; Turbiez, M.; Mcculloch, I. Recent Advances in the Development of Semiconducting DPP-Containing Polymers for Transistor Applications. *Adv. Mater.* **2013**, *25*, 1859–1880. https://doi.org/10.1002/adma.201201795.
(45) Flagg, L. Q.; Giridharagopal, R.; Guo, J.; Ginger, D. S. Anion-Dependent Doping and Charge Transport in Organic Electrochemical Transistors. *Chem. Mater.* **2018**, *30*, 5380–5389. https://doi.org/10.1021/acs.chemmater.8b02220.
(46) Cendra, C.; Giovannitti, A.; Savva, A.; Venkatraman, V.; McCulloch, I.; Salleo, A.; Inal, S.; Rivnay, J. Role of the Anion on the Transport and Structure of Organic Mixed Conductors. *Adv. Funct. Mater.* **2018**, *29*, 1807034. https://doi.org/10.1002/adfm.201807034.
(47) Zhang, S.; Kumar, P.; Nouas, A. S.; Fontaine, L.; Tang, H.; Cicoira, F. Solvent-Induced Changes in PEDOT:PSS Films for Organic Electrochemical Transistors. *APL Mater.* **2015**, *3*, 014911. https://doi.org/10.1063/1.4905154.
(48) Kim, S. M.; Kim, C. H.; Kim, Y.; Kim, N.; Lee, W. J.; Lee, E. H.; Kim, D.; Park, S.; Lee, K.; Rivnay, J.; Yoon, M. H. Influence of PEDOT:PSS Crystallinity and Composition on Electrochemical Transistor Performance and Long-Term Stability. *Nat. Commun.* **2018**, *9*, 3858. https://doi.org/10.1038/s41467-018-06084-6.
(49) Savva, A.; Cendra, C.; Giugni, A.; Torre, B.; Surgailis, J.; Ohayon, D.; Giovannitti, A.; McCulloch, I.; Di Fabrizio, E.; Salleo, A.; Rivnay, J.; Inal, S. The Influence of Water on the Performance of Organic Electrochemical Transistors. *Chem. Mater.* **2019**, *31*, 927–937. https://doi.org/10.1021/acs.chemmater.8b04335.
(50) Hofmeister, F. Zur Lehre von Der Wirkung Der Salze. *Arch. für Exp. Pathol. und Pharmakologie* **1888**, *24*, 247–260. https://doi.org/10.1007/BF01918191.
(51) Thomas, E. M.; Brady, M. A.; Nakayama, H.; Popere, B. C.; Segalman, R. A.; Chabinyc, M. L. X-Ray Scattering Reveals Ion-Induced Microstructural Changes During Electrochemical Gating of Poly(3-Hexylthiophene). *Adv. Funct. Mater.* **2018**, *28*, 1803687. https://doi.org/10.1002/adfm.201803687.
(52) Guardado, J. O.; Salleo, A. Structural Effects of Gating Poly(3-Hexylthiophene) through an Ionic Liquid. *Adv. Funct. Mater.* **2017**, *27*, 1701791. https://doi.org/10.1002/adfm.201701791.
(53) Sivaraman, P.; Mishra, S. P.; Bhattacharrya, A. R.; Thakur, A.; Shashidhara, K.; Samui, A. B. Effect of Regioregularity on Specific Capacitance of Poly (3-Hexylthiophene). *Electrochim. Acta* **2012**, *69*, 134–138. https://doi.org/10.1016/j.electacta.2012.02.085.
(54) Rivnay, J.; Ramuz, M.; Leleux, P.; Hama, A.; Huerta, M.; Owens, R. M. Organic

Electrochemical Transistors for Cell-Based Impedance Sensing. *Appl. Phys. Lett.* **2015**, *106*, 043301. https://doi.org/10.1063/1.4906872.
(55) Sauerbrey, G. Verwendung von Schwingquarzen Zur Wägung Dünner Schichten Und Zur Mikrowägung. *Zeitschrift für Phys.* **1959**, *155*, 206–222.
(56) Wang, S.; Li, F.; Easley, A. D.; Lutkenhaus, J. L. Real-Time Insight into the Doping Mechanism of Redox-Active Organic Radical Polymers. *Nat. Mater.* **2018**, *18*, 69–76. https://doi.org/10.1038/s41563-018-0215-1.
(57) Zhang, L.; Andrew, T. L. Deposition Dependent Ion Transport in Doped Conjugated Polymer Films: Insights for Creating High-Performance Electrochemical Devices. *Adv. Mater. Interfaces* **2017**, *4*, 1700873. https://doi.org/10.1002/admi.201700873.
(58) Kou, R.; Zhang, J.; Wang, T.; Liu, G. Interactions between Polyelectrolyte Brushes and Hofmeister Ions: Chaotropes versus Kosmotropes. *Langmuir* **2015**, *31*, 10461–10468. https://doi.org/10.1021/acs.langmuir.5b02698.
(59) Nowak, D.; Morrison, W.; Wickramasinghe, H. K.; Jahng, J.; Potma, E.; Wan, L.; Ruiz, R.; Albrecht, T. R.; Schmidt, K.; Frommer, J.; Sanders, D. P.; Park, S. Nanoscale Chemical Imaging by Photoinduced Force Microscopy. *Sci. Adv.* **2016**, *2*. https://doi.org/10.1126/sciadv.1501571.
(60) Kong, J.; Giridharagopal, R.; Harrison, J. S.; Ginger, D. S. Identifying Nanoscale Structure-Function Relationships Using Multimodal Atomic Force Microscopy, Dimensionality Reduction, and Regression Techniques. *J. Phys. Chem. Lett.* **2018**, *9*, 3307–3314. https://doi.org/10.1021/acs.jpclett.8b01003.
(61) Enengl, S.; Enengl, C.; Stadler, P.; Neugebauer, H.; Sariciftci, N. S. Spectroelectrochemical Studies on Quinacridone by Using Poly(Vinyl Alcohol) Coating as Protection Layer. *ChemPhysChem* **2015**, *16*, 2206–2210. https://doi.org/10.1002/cphc.201500165.
(62) Kline, R. J.; Mcgehee, M. D. Morphology and Charge Transport in Conjugated Polymers Morphology and Charge Transport in Conjugated Polymers. *J. Macromol. Sci. Part C Polym. Rev.* **2006**, *46*, 27–45. https://doi.org/10.1080/15321790500471194.
(63) Coropceanu, V.; Cornil, J.; Da Silva Filho, D. A.; Olivier, Y.; Silbey, R.; Bredas, J.-L. Charge Transport in Organic Semiconductors. *Chem. Rev.* **2007**, *107*, 926–952. https://doi.org/10.1021/cr050140x.
(64) Gu, K.; Snyder, C. R.; Onorato, J.; Luscombe, C. K.; Bosse, A. W.; Loo, Y. Assessing the Huang–Brown Description of Tie Chains for Charge Transport in Conjugated Polymers. *ACS Macro Lett.* **2018**, *7*, 1333–1338. https://doi.org/10.1021/acsmacrolett.8b00626.
(65) Zen, A.; Pflaum, J.; Hirschmann, S.; Zhuang, W.; Jaiser, F.; Asawapirom, U.; Rabe, J. P.; Scherf, U.; Neher, D. Effect of Molecular Weight and Annealing of Poly(3-Hexylthiophene)s on the Performance of Organic Field-Effect Transistors. *Adv. Funct. Mater.* **2004**, *14*, 757–764. https://doi.org/10.1002/adfm.200400017.

Chapter 4. P-Type Electrochemical Doping Can Occur by Cation Expulsion in a High Performing Polymer for Organic Electrochemical Transistors

4.1 INTRODUCTION

Conjugated polymers with the ability to conduct both electrons and ions have seen surging interest as active materials for a applications including neuromorphic computing,[1–3] electrochemical energy storage,[4,5] bioelectronics,[6–10] and thermoelectrics.[11,12] Each of these applications rely in some way on the coupling between the ionic and electronic charge in the mixed conductor. In organic electrochemical transistors (OECTs), this coupling allows ionic charges to compensate for injected electronic charges, allowing much greater modulation of the channel conductivity compared to organic field effect transistors (OFETs). A wide variety of mixed conductors capable of such volumetric ion transport exist and the nuances of each type have been reviewed by Rivnay and co-workers.[13] Here, we study the simplest system of a homogenous, single phase, p-type (hole-conducting) material. The conventional understanding of electrochemical oxidation (doping) of this type of system is that an external bias induces injection of holes into the polymer film, which is accompanied by injection of anions from the electrolyte to maintain charge neutrality.[14] This can be described as follows:

$$\boldsymbol{P^0}_{(s)} + \boldsymbol{A^-}_{(aq)} \rightleftharpoons \boldsymbol{P^+(A^-)}_{(s)} + \boldsymbol{e^-} \qquad \text{(Eq 1.)}$$

where P0 is the neutral polymer species, A- is an anion from solution, P+(A-) is a positive polymer polaron (radical cation)/anion pair within the bulk of the polymer film, and e- is an electron removed from the polymer by the external circuit. For charge compensation of this type to occur, the material must allow facile electronic and ionic movement throughout the bulk of the film.

Initial work in the mixed conductor field showed that increased swelling in the presence of electrolyte leads to higher ionic conductivity.[15–17] Thus the design of modern organic mixed conductors is largely based upon substituting hydrophilic side chains, which promote hydration and ion transport, onto polymer backbones and small molecules[18] known to have high electronic conductivity. This strategy has proven very successful, as polymers with polar side chains including alcohols,[19] carboxylic acids,[20] amides,[21] sulfonates,[22–24] and most commonly oligoethylene glycol,[25–32] display dramatically enhanced ion transporting properties while maintaining their good electronic properties.

The development of these high performing polymers has led to a wealth of recent papers and reviews regarding OECTs for biosensing. In all of the recent literature, the ionic charge compensation during oxidation of p-type polymers is almost universally described as anion injection into the film, 33–38 despite cation ejection being equivalent from the perspective of maintaining charge neutrality. Since most of the best-performing mixed conductors display significant swelling (on the order of 20-100%[16,18,28,39] with some polymers displaying swelling up to 1000%),[40] it is reasonable to assume that all components of the electrolyte (solvent molecules, anion, and cation) can be present in the polymer film in its neutral, hydrated state. With cations in close proximity to the polymer backbone, it seems possible that these cations are involved in the charge compensation during doping. In fact, this mechanism of charge compensation has been recently observed in organic radical polymers for battery applications.[41] Previous examples of p-type doping by cation expulsion can also be found in electrochemical cycling of electropolymerized polypyrrole, although this is often a result of the one of the ions being rendered immobile by being trapped in the polymer network during the polymerization.[42–45] Additionally, a recent review on mixed ionic/electronic conductors speculates that cation ejection may play a role

in charge compensation in modern OECT materials.13 Despite the growing number of applications that utilize mixed conductors, the exact mechanism of charge compensation during electrochemical doping is rarely been investigated.

Here, we carefully examine the doping mechanism in poly(3-{[2-(2-methoxyethoxy)ethoxy]methyl}thiophene-2,5-diyl) (P3MEEMT), a model p-type mixed conductor (structure in Figure 4.1 A) which has figures of merit comparable to state-of-the-art materials.39 We present direct evidence that charge compensation can occur by cation expulsion during the electrochemical oxidation of P3MEEMT. We use electrochemical quartz microbalance (EQCM) to show that during the early stages of doping the polymer film loses mass, implying substantial cation expulsion before the conventional doping mechanism of anion injection begins to dominate. We verify this result by directly measuring ion concentrations in the polymer film using glow discharge optical emission spectroscopy (GDOES). We show that prior to bias there are both cations and anions present within the polymer film. At low doping levels, the concentration of electrolyte cations within the film rapidly decreases upon application of an oxidative potential. Further doping/oxidation leads to an increase in the number of electrolyte-derived anions within the polymer film. After the bias is removed, the numbers of cations and anions return to their initial states. This set of measurements provide insight into the mechanism of charge compensation that occurs in the model mixed conductor P3MEEMT.

4.2 Results and Discussion

Figure 2.1 A shows a schematic of the EQCM experiment which is further explained in the supporting information. We perform cyclic voltammetry (CV) on a polymer-coated quartz crystal and simultaneously measure the current injected into the polymer film as well as the oscillator

frequency of the crystal. Integrating the current against time allows us to calculate the total charge delivered. Using the Sauebrey equation and the thin film approximation we calculate the change in mass of the polymer film based on the change in frequency46 (calibration in Figure C.1). The top panel in Figure 4.1 B shows the bias applied to the working electrode (relative to Ag/AgCl) during one cycle. We sweep the voltage between 0.8 and -0.5 V at 50 mV/s (repeated cycles and other scan rates are shown in Figure C.2). The middle panel of Figure 4.1 B shows the total charge injected into the film as a function of time in two different 20 mM aqueous chloride salts: potassium chloride (KCl) (blue), tetrabutylammonium chloride (TBACl) (orange). Despite drastically different cations, the charge injection behavior in the chloride salts is qualitatively very similar. The onset of oxidation begins at 0.35 V and the total magnitude of charge injected is 2.0 mC for KCl and 1.6 mC for TBACl. In the lower panel of Figure 4.1 B we display the change in mass over time during the same bias sweep. Again, the chloride salts behave qualitatively similarly despite the drastically different cations. At the start of the bias sweep, there is a very slight mass loss of <0.2 µg/cm2. As the bias ramp continues to increase the film consistently gains mass, resulting in an oxidized mass 2.7 µg/cm2 greater than the original neutral mass in KCl and 2.2 µg/cm^2 greater in TBACl. At the completion of the oxidation/reduction cycle the film mass returns to the original mass in both electrolytes.

In Figure 4.2 C, we perform a similar experiment in two electrolytes with a larger, more polarizable anion, potassium hexafluorophosphate (KPF6) (purple), and tetrabutylammonium hexafluorophosphate (TBAPF6) (green). Again, the top panel shows the bias applied. The middle panel shows the charge injected into the polymer film. When cycled in KPF_6, the onset of oxidation (0.2 V) is lower than in the chloride salts and significantly more charge is injected (4.8 mC). This increase in injected charge is consistent with previous reports that larger anions inject at a lower

potential and to a greater extent than smaller anions.[39,47,48] However, when we attempt to oxidize the film in $TBAPF_6$, there is a shift to a higher onset of oxidation (0.45 V) and the magnitude of charge injected is greatly reduced (0.9 mC). These cation-dependent differences between oxidation of the film in different electrolytes are also reflected in the lower panel of Figure 4.1 C, where the change in mass displayed. When oxidizing the film in a $TBAPF_6$ electrolyte, there is no detectable mass loss. Interestingly, despite injecting much less charge overall, the mass gain in $TBAPF_6$ is over 13 $\mu g/cm^2$ (~5x more mass gain than with other salts). Despite sharing the same anion, the mass change during oxidation in KPF_6 is dramatically different from that of $TBAPF_6$, or indeed from any of the chloride salts. Upon initial application of an oxidative bias, the film mass consistently decreases until it reaches a minimum 2.9 $\mu g/cm^2$ below the original film mass. From that point on, the mass increases until the oxidative bias is removed. During the dedoping process the film first loses mass and then gains mass back to its original neutral mass. The presence of these obvious minima in the mass verses time trace indicate that there is a moment during the cycle where the rate of mass gain matches the rate of mass loss, resulting in no net mass change.

From this data we conclude that under certain condition the electrochemical oxidation of P3MEEMT is in fact cation dependent. When the anion is chloride, which tends to enter the polymer film highly hydrated,[47,49] the identity of the cation does not strongly affect the electrochemical doping process. We further confirm this result with EQCM measurements in 2 other chloride salts (see Figure C.3) and show that the identity of the cation does not significantly change any of the properties we measure (current, mass, stiffness, dopant molar mass). On the contrary, when the anion is $PF6^-$, the identity of the cation has a dramatic effect on the oxidation behavior of the polymer. In the case of a very large cation paired with $PF6^-$, there is never any mass loss due to cation expulsion (likely because the large cation never enters the film), and the

mass gain upon anion injection is 5 times greater than any of the other salts. But in the case of a smaller cation paired with the $PF6^-$ anion, electrochemical oxidation results in an evolving process of mass transfer both out of, and eventually into, the polymer film.

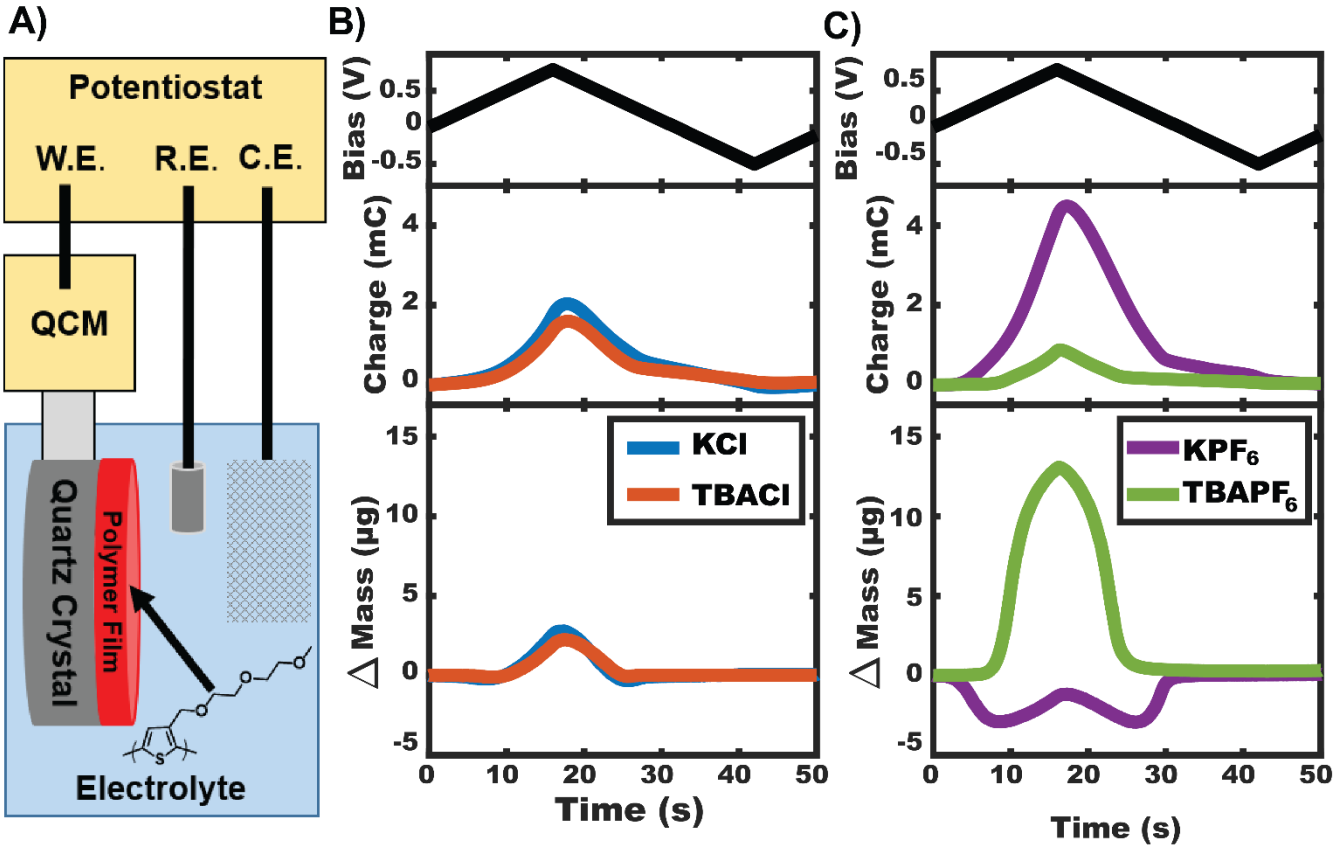

Figure 4.1: Electrochemical Quartz Crystal Microbalance gravimetry. A) Schematic showing the measurement setup. A polymer film-coated quartz crystal serves as the working electrode, a platinum mesh is used as the counter electrode and an Ag/AgCl puck is used as the reference electrode. B) Shows the bias applied, charge injected into the polymer, and the change in mass of the polymer film during a cyclic voltammetry scan in 2 different chloride-based electrolytes KCl (blue) and TBACl (orange). C) Shows the bias applied, charge injected into the polymer, and the change in mass of the polymer film during a cyclic voltammetry scan in 2 different $PF6^-$ based electrolytes: KPF_6 (purple) and $TBAPF_6$ (green).

In Figure 4.2 we more closely examine the complex mass changes that occur during the oxidation and reduction of the P3MEEMT film in KPF_6. The upper panel shows change in mass as a function

of bias applied at a sweep rate of 50 mV/s. To help with the discussion, we divide the cyclic voltammetry sweep into 4 regions. In region I, holes are injected (oxidation) into the polymer film yet the polymer is losing mass. In region II, holes are injected (oxidation) and the film is gaining mass. In region III, holes are extracted from the film (reduction) and the film loses mass. In region IV, holes are extracted from the film (reduction) yet the film gains mass. The mass behavior in regions II and III are consistent with the conventional understanding of charge compensation during electrochemical oxidation/reduction of p-type polymers: anions move into/out of the film to electronically compensate for the injected charge. However, the doping in region I and dedoping in region IV are quite surprising. Even though injected holes need to be electronically compensated, the film overall loses mass throughout region I. From a charge balance perspective, the two ways to compensate for the injected hole are K^+ cations leaving the film or $PF6^-$ anions entering the film (charged salt complexes i.e. $K(PF_6)^{2-}$ may also play a role, but we deem this is unlikely at the modest 20 mM concentrations used).[50] Solvent molecules represent the other mobile species that could account for mass changes, but since the solvent is neutral it does not compensate charge. Mass loss during polymer oxidation similar to what we see in region I, has most frequently been attributed to field-driven solvent expulsion due to structural changes in the polymer.[51–54] While in other systems the mass loss region has been attributed to cation ejection.[41] However, since EQCM only provides information about net mass transfer into or out of the film, we need more information to confirm which mobile species are associated with the observed mass loss and better understand the doping mechanism.

To identify the presence of the cation and/or anion within the film at different stages of oxidation we use glow discharge optical emission spectroscopy (GDOES). Complete experimental details of the GDOES experiment are included in the SI. Briefly, we begin a cyclic voltammetry cycle to

electrochemically dope the films. At the desired oxidation state, we remove the film from the electrolyte solution, and quickly rinse it three times in deionized water. The doping state of the polymer is maintained through the wash step as evidenced by the fact that the color change associated with electrochemical oxidation remains unchanged even after rinsing (Figure C.4). We then use GDOES to analyze the elemental content of each film. The lower panel of Figure 4.2 shows the integrated GDOES signal normalized to the sulfur content in the polymer. The supporting information includes details on the normalization used (Figure C.5), the relative instrumental sensitivity to potassium and phosphorous (Figure C.6), and the raw GDOES spectra (Figure C.7). The phosphorous signal (orange) originates from the $PF6^-$ anion, and the potassium signal (blue) comes from the K^+ cation. At zero applied bias, the data indicate the presence of both cations and anions within the film. We note that we do not observe any ions in the film after submerging in KCl or $TBAPF_6$ electrolyte (Figure C.8). As the oxidation of the film begins (region I), we observe a decrease in the cation content within the film. When the mass reaches a minimum, at the interface between region I and region II, all the cation has been eliminated from the film and we observe an increase in the anion content within the film. In region II, we observed continuous increase in anion content within the film and no detectable cations present. As we begin to dedope the film in region III, the anion content decreases. Finally, after a full oxidation/reduction cycle the film returns to a neutral state that contains both anions and cations. These data provided direct evidence that cations exist inside the film in its neutral state and that cation ejection plays a role in charge compensation during the doping process.

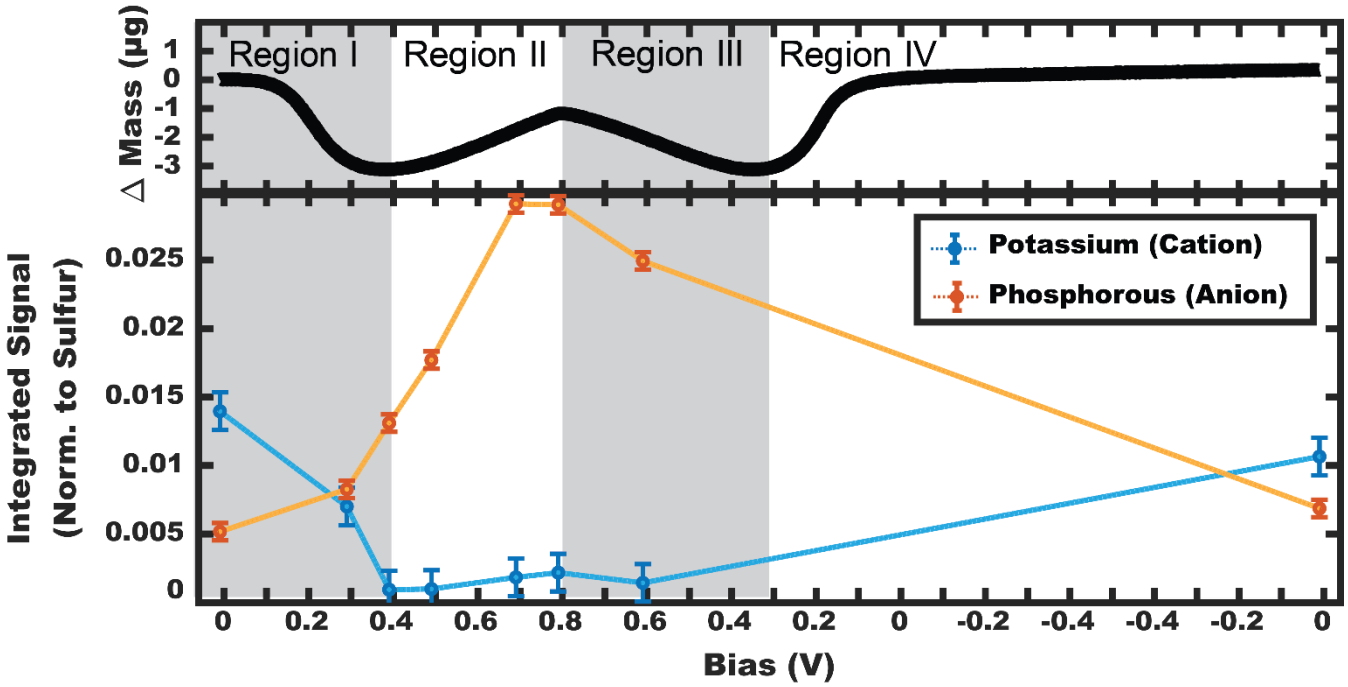

Figure 4.2: Glow Discharge Optical Emission Spectroscopy (GDOES) as a function of applied bias. Upper panel shows mass change as a function of bias when P3MEEMT is oxidized in 20 mM KPF_6. The lower panel shows the integrated GDOES signal normalized to the sulfur signal for the potassium in the cation (blue) and the phosphorous in the anion (orange) at a variety of different oxidation states.

Together, the presented data leads us to propose the following doping mechanism for electrochemical oxidation of P3MEEMT in 20 mM KPF_6. First, contact with the electrolyte leads to dramatic swelling and hydration of the film as shown in Figure 4.3 B. In Figure 4.3 C we show that initial application of an oxidative bias (and hole injection into the polymer) causes ejection of cations, as well as large amounts of solvent to be expelled from the film (see Figure C.9 and Figure C.10 for discussion of solvent transport). As the cation concentration in the film is depleted, anions begin injecting into the film until these two processes balance resulting in the minimum in the mass trace. Finally, once all the cation (and likely some solvent) has been ejected from the film, the charge compensation proceeds purely by the conventionally described anion injection

mechanism (shown in Figure 4.3 D). Dedoping (reduction) follows this same process in reverse. First anions are ejected, and then cations and solvent are injected to end back at the initial state.

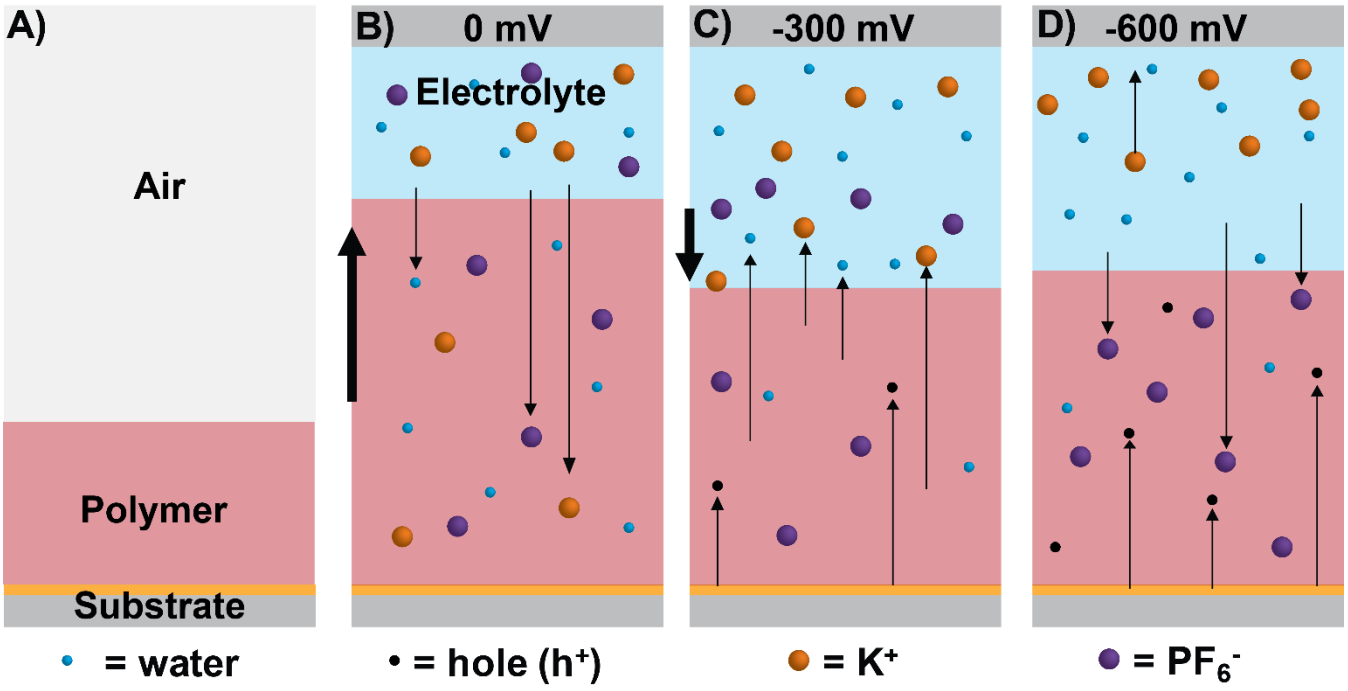

Figure 4.3: Scheme illustrating the mechanism of electrochemical oxidation. A) Shows the polymer on a conductive substrate in air. B) Shows the initial (no bias) swelling of the film due to hydration which includes transport of water, cations, and anions, across the polymer electrolyte interface. C) Shows the doping process in region I, where solvent and cations are ejected from the film. D) Shows the doping process in region II, where anions are injected into the polymer film.

By contrast we believe that electrochemical oxidation of P3MEEMT in KCl proceeds by the following mechanism (illustrated in Figure C.11). First, hydration of the film only includes solvent, but few if any ions migrate into the neutral polymer. Upon initial application of bias, there is a mass loss 10x smaller than in KPF6, which we attribute to the expulsion of a small number of cations (below the detection limit of GDOES) and/or expulsion of solvent. Additional doping then results in mass gain due to anion injection. We believe this mechanism applies to all the chloride

salts we studied. Despite the large anion, we hypothesize oxidation in $TBAPF_6$ proceeds by a similar mechanism because the TBA cations are too bulky to enter the film.

4.3 Conclusion

In summary, we electrochemically oxidized P3MEEMT in a variety of electrolytes and studied the process of charge compensation in these polymer films that can simultaneously transport electronic and ionic charges. We find that the mechanism of charge compensation is sensitive to the chemical nature of both the anion and cation, even for materials such as P3MEEMT that are hydrated upon exposure to water.39 We find that, when $PF6^-$ is the anion, even the cation identity can affect the doping process. Indeed, mass changes and atomic emission spectroscopy taken during electrochemical doping with KPF_6, show that K^+ is expelled from the film in the initial stages of oxidation, suggesting that, at least in some cases, expulsion of cations can be used to provide the initial charge compensation mechanism. These results are an important reminder of the fact that the cation is not always an inactive bystander but can play a significant role in the electrochemical oxidation process, even for p-type mixed ionic/electronic conductors. These results underscore the opportunity to further tailor the performance of organic mixed conductors in a range of applications through a better understanding of how ions interact with the polymer matrix, as well as with electronic charges, in organic semiconductors. We speculate that differences in both charge balance, and accompanying solvent mass, may be one reason why electronic charge carrier mobilities in OECTs can be so sensitive to counterion chemistry.[47]

4.4 METHODS

Materials: All salts (KCl, NaCl, CsCl, TBACl, KPF_6, $TBAPF_6$) were purchased from Sigma Aldrich and dried in a vacuum oven before use. Chlorobenzene was also purchased from Sigma Aldrich and used as received. N-bromosuccinimide was recrystallized from water prior to use. Tetrahydrofuran (THF) and dichloromethane (DCM) were dried and deoxygenated on a PureSolv solvent purification system. All other reagents were used as received from Sigma Aldrich.

Polymer Synthesis and Characterization:

All reactions were performed under nitrogen using standard Schlenk line techniques, and all glassware was dried overnight at 120 °C prior to use. 2,5-dibromo-3-methoxyethoxyethoxymethylthiophene was synthesized using a modified literature procedure.[1] NMR was performed using either a 300 MHz Bruker AV-300 or a 500 MHz Bruker AV-500 at 25 °C. The synthesized polymer's molecular weight was characterized using size exclusion chromatography (SEC), on a Malvern Viscotek TDA 305 GPC coupled to a UV-detector. Samples were run at 30 °C using $CHCl_3$ at a flow rate of 1 mL/min as an eluent.

Monomer Synthesis:

3-thiophenemethanol (3.77 mL, 40 mmol) and 36.4 mL of THF were added to a 3-neck flask, and then degassed by nitrogen bubbling for 15 minutes. Then, recrystallized NBS (total: 14.15 g, 79.5 mmol) was added to the reaction quickly, across 5 equivalent portions, recapping the reaction in between each addition. The reaction was stirred overnight, then filtered, and the solvent removed using rotary evaporation. The residue was purified using column chromatography with a hexanes to ethyl acetate mixture of 4:1. The product was collected as a

white solid in 90% yield. ^{1}H NMR (300 MHz, $CDCl_3$): δ 7.03 (s, 1H), 4.60 (s, 2H), and 1.95 (br, 1H).

2,5-dibromo-3-thiophenemethanol (9.0 g, 33.5 mmol) and 165 mL of DCM were added to a round bottom flask, then cooled over ice for 20 minutes. PBr_3 (3.20 mL, 34.25 mmol) was added dropwise over the course of 15 minutes, then the reaction was allowed to warm to room temperature. The reaction was stirred for 5 hours at room temperature, then quenched with 100 mL of 10% $NaHCO_3$ solution. Allow bubbling to subside, then extract the product with DCM, wash with brine, and dry over $MgSO_4$. The solvent was removed through rotary evaporation, and the product was placed in the freezer overnight at -20 °C, after which it was recovered as a white solid in 93% yield. ^{1}H NMR (300 MHz, $CDCl_3$): δ 7.00 (s, 1H), 4.36 (s, 2H).

To a 3-neck flask equipped with an addition funnel, diethylene glycol monomethyl ether (3.5 mL, 30 mmol) and 100 mL of THF were added. To this, NaH (1.32 g, 33 mmol) was added in on portion, and allowed to react for 10 minutes. During this time, 2,5-dibromo-3-thiophenemethylbromide (9.65 g, 29 mmol) was dissolved in 25 mL of THF, and added to the addition funnel. It was then added dropwise over the course of 15 minutes, and the reaction was stirred overnight at room temperature, resulting in the formation of a significant amount of salt precipitate. The reaction mixture was filtered over a thin pad of Celite to remove salt, and the product was washed through with excess THF. The THF was removed through rotary evaporation, and the product was purified using a column run with a 3:2 mixture of hexanes:ethyl acetate. The recovered product was a pale yellow oil and was collected in 87% yield, and was stored at -20 °C and away from light. ^{1}H NMR (300 MHz, $CDCl_3$) δ 7.0 (s, 1H), 4.43 (s, 2H), 3.65 (m, 6H), 3.57 (m, 2H), 3.39 (s, 3H).

Polymer Synthesis:

2,5-dibromo-3-methoxyethoxyethoxymethylthiophene (372 mg, 1 mmol) was added to a Schlenk flask, then degassed under high vacuum for 30 minutes. Then 10 mL of THF was added, and the mixture was cooled to 0 °C, and *i*-PrMgCl (2.0 M in THF, 0.5 mL, 1.0 mmol) was added dropwise over 10 minutes, stirring vigorously. The flask was allowed to warm to room temperature and stirred for 1 hour. To begin the polymerization, the flask was heated to 45 °C, and then Ni(dppp)Cl_2 (4.334 mg, 0.008 mmol) was added rapidly in one portion, after which the polymerization was left to stir vigorously at 45 °C for 2 hours. The polymerization was quenched with the addition of HCl (5 M, 1.0 mL), and the polymer was precipitated into 400 mL of MeOH. The resultant precipitate was allowed to settle briefly, then collected over a filter. The collected solid was then purified using successive Soxhlet extractions with hexanes and MeOH, and then collected using chloroform. The chloroform was removed, and the polymer was redissolved into THF, then precipitated into MeOH and collected over a filter. ^{1}H NMR (500 MHz, $CDCl_3$) δ 7.25 (s, 1H), 4.67 (s, 2H), 3.75 (s, 4H), 3.67 (m, 2H), 3.57 (m, 2H), 3.37 (s, 3H). $Đ$ = 2.0, M_n = 11 kg/mol.

Sample Preparation:

The polymer was dissolved in chlorobenzene at 20 mg/mL concentration and stirred at 800 rpm overnight at room temperature. Films were created by depositing 60 µL of solution onto QCM crystals or ITO substrates (for GDOES) and spinning for 60 seconds at 1000 rpm (thickness ~80 nm). All electrolytes were made at 20 mM concentration in Milli-Q water.

Electrochemical Quartz Crystal Microbalance (EQCM) Gravimetry:

Electrogravimetric measurements were made using 1 in. diameter gold-coated AT quartz crystals (Stanford Research Systems) on an SRS QCM200 instrument. The electrochemical potential was applied in a 3-electrode cell with the polymer coated QCM crystal serving as the working electrode, a platinum mesh serving as the counter electrode (Aldrich), and an Ag/AgCl puck electrode (A-M Systems, Inc.) serving as the reference electrode. A potentiostat (MetroOhm Autolab PGSTAT204) was used to apply the bias, record the current, and simultaneously record the oscillator frequency and series resonance resistance from the EQCM. The apparent molar mass of the dopant species is calculated from the slope of a change in mass versus injected charge plot as described by Zhang et al.[2] Previous EQCM studies have shown that thin (~100 nm) conducting polymer films on the quartz crystals do not cause a significant deviation from the rigid film approximation; therefore, it can be assumed that the frequency shifts measured here are a direct measure of mass changes in the polymer layer.[3–5]

Glow Discharge Optical Emission Spectroscopy (GDOES):

We prepared samples for GDOES at the desired doping level by using polymer coated ITO substrates as the working electrode in the same 3-electrode cell as mentioned above. During a cyclic voltammetry scan, we removed the polymer film from solution at the desired oxidation state. Once removed from solution, we used a nitrogen gun to blow off as much remailing electrolyte as possible and then rinsed the sample in 3 successive DI water baths. We then used a GD profiler 2 from Horriba Scientific with the RF plasma settings shown in

Table 4.1 to analyze the elemental content within the film. Using these settings, we completely etched through the polymer in 5-25 seconds.

Due to variation in the plasma etching, it is hard to directly compare elemental content between samples. To allow comparisons, we develop the following normalization procedure. First, we extract a baseline signal intensity for each element by averaging the signal over the final 30 seconds of etch when all polymer signal is gone. We then subtract this baseline from the raw signal. Next, we integrate the signal in time to get a total signal value. Since the only sulfur present in the samples is from the polymer backbone, the total sulfur signal should be constant for all samples. Therefore, by dividing the integrated ion signals (potassium and phosphorous) by the integrated sulfur signal we can correct for variations in etch rate and make comparisons of ion content between multiple samples.

Table 4.1: RF plasma settings

Pressure	400 Pa
Power	15 W
Frequency	1000 Hz
Duty Cycle	0.0625
Resulting Power	0.9375 W
Module	7 V
Phase	4 V

4.5 ACKNOWLEDGEMENTS

This paper is based primarily on work supported by a seed award from the University of Washington and Pacific Northwest National Laboratory's Northwest Institute for Materials Physics, Chemistry, and Technology (NW IMPACT). C. G. B. is a Washington Research

Foundation Postdoctoral Fellow. J.W.O. and C.K.L. thank NSF CBET 1922259 and NSF DMREF 1629369 for funding to synthesize the materials. We also gratefully acknowledge the Alvin L. and Verla R. Kwiram endowed fund at the University of Washington for supporting early stages of this research. Part of this work was conducted at the Molecular Analysis Facility, a National Nanotechnology Coordinated Infrastructure site at the University of Washington that is supported in part by the National Science Foundation (grant ECC-1542101), the University of Washington, the Molecular Engineering & Sciences Institute, the Clean Energy Institute and the National Institutes of Health.

4.6 REFERENCES

(1) Burgt, Y. van de; Lubberman, E.; Fuller, E. J.; Keene, S. T.; Faria, G. C.; Agarwal, S.; Marinella, M. J.; Talin, A. A.; Salleo, A. A Non-Volatile Organic Electrochemical Device as a Low-Voltage Artificial Synapse for Neuromorphic Computing. *Nat. Mater.* **2017**, *16*, 414–419. https://doi.org/10.1038/nmat4856.

(2) Keene, S. T.; Melianas, A.; Burgt, Y. Van De; Salleo, A. Mechanisms for Enhanced State Retention and Stability in Redox-Gated Organic Neuromorphic Devices. **2018**, *1800686*, 1–10. https://doi.org/10.1002/aelm.201800686.

(3) Yoeri van de Burgt, Armantas Melianas, Scott Tom Keene, G. M. & A. S. Organic Electronics for Neuromorphic Computing. *Nat. Electron.* **2018**, *1*, 386–397.

(4) Moia, D.; Giovannitti, A.; Szumska, A. A.; Maria, I. P.; Rezasoltani, E.; Sachs, M.; Schnurr, M.; Barnes, P. R. F.; McCulloch, I.; Nelson, J. Design and Evaluation of Conjugated Polymers with Polar Side Chains as Electrode Materials for Electrochemical Energy Storage in Aqueous Electrolytes. *Energy Environ. Sci.* **2019**, *12* (4), 1349–1357. https://doi.org/10.1039/c8ee03518k.

(5) Volkov, A. V.; Sun, H.; Kroon, R.; Ruoko, T.-P.; Che, C.; Edberg, J.; Müller, C.; Fabiano, S.; Crispin, X. Asymmetric Aqueous Supercapacitor Based on P- and n-Type Conducting Polymers. *ACS Appl. Energy Mater.* **2019**. https://doi.org/10.1021/acsaem.9b00853.

(6) Tan, E.; Pappa, A.; Pitsalidis, C.; Nightingale, J.; Wood, S.; Castro, F. A.; Owens, R. M.; Kim, J. A Highly Sensitive Molecular Structural Probe Applied to In-situ Biosensing of Metabolites Using PEDOT:PSS . *Biotechnol. Bioeng.* **2019**. https://doi.org/10.1002/bit.27187.

(7) Venkatraman, V.; Friedlein, J. T.; Giovannitti, A.; Maria, I. P.; McCulloch, I.; McLeod, R. R.; Rivnay, J. Subthreshold Operation of Organic Electrochemical Transistors for Biosignal Amplification. *Adv. Sci.* **2018**, *1800453*, 1800453. https://doi.org/10.1002/advs.201800453.

(8) Pappa, A. M.; Ohayon, D.; Giovannitti, A.; Maria, I. P.; Savva, A.; Uguz, I.; Rivnay, J.; McCulloch, I.; Owens, R. M.; Inal, S. Direct Metabolite Detection with an N-Type

Accumulation Mode Organic Electrochemical Transistor. *Sci. Adv.* **2018**, *4*, eaat0911. https://doi.org/10.1126/sciadv.aat0911.
(9) Proctor, C. M.; Uguz, I.; Slezia, A.; Curto, V.; Inal, S.; Williamson, A.; Malliaras, G. G. An Electrocorticography Device with an Integrated Microfluidic Ion Pump for Simultaneous Neural Recording and Electrophoretic Drug Delivery In Vivo. *Adv. Biosyst.* **2019**, *3* (2), 3–8. https://doi.org/10.1002/adbi.201800270.
(10) Wustoni, S.; Wang, S.; Alvarez, J. R.; Hidalgo, T. C.; Nunes, S. P.; Inal, S. An Organic Electrochemical Transistor Integrated with a Molecularly Selective Isoporous Membrane for Amyloid-β Detection. *Biosens. Bioelectron.* **2019**, *143* (May), 111561. https://doi.org/10.1016/j.bios.2019.111561.
(11) Kiefer, D.; Giovannitti, A.; Sun, H.; Biskup, T.; Hofmann, A.; Koopmans, M.; Cendra, C.; Weber, S.; Anton Koster, L. J.; Olsson, E.; et al. Enhanced N-Doping Efficiency of a Naphthalenediimide-Based Copolymer through Polar Side Chains for Organic Thermoelectrics. *ACS Energy Lett.* **2018**, *3* (2), 278–285. https://doi.org/10.1021/acsenergylett.7b01146.
(12) Li, Z.; Sun, H.; Hsiao, C. L.; Yao, Y.; Xiao, Y.; Shahi, M.; Jin, Y.; Cruce, A.; Liu, X.; Jiang, Y.; et al. A Free-Standing High-Output Power Density Thermoelectric Device Based on Structure-Ordered PEDOT:PSS. *Adv. Electron. Mater.* **2018**, *4* (2), 1–8. https://doi.org/10.1002/aelm.201700496.
(13) Paulsen, B. D.; Tybrandt, K.; Stavrinidou, E.; Rivnay, J. Organic Mixed Ionic–Electronic Conductors. *Nat. Mater.* **2019**. https://doi.org/10.1038/s41563-019-0435-z.
(14) Shiri, P.; Dacanay, E. J. S.; Hagen, B.; Kaake, L. G. Vogel–Tammann–Fulcher Model for Charging Dynamics in an Organic Electrochemical Transistor. *J. Mater. Chem. C* **2019**. https://doi.org/10.1039/c9tc02563d.
(15) Stavrinidou, E.; Leleux, P.; Rajaona, H.; Khodagholy, D.; Rivnay, J.; Lindau, M.; Sanaur, S.; Malliaras, G. G. Direct Measurement of Ion Mobility in a Conducting Polymer. *Adv. Mater.* **2013**, *25*, 4488–4493. https://doi.org/10.1002/adma.201301240.
(16) El Mahmoudy, M.; Inal, S.; Charrier, A.; Uguz, I.; Malliaras, G. G.; Sanaur, S. Tailoring the Electrochemical and Mechanical Properties of PEDOT:PSS Films for Bioelectronics. *Macromol. Mater. Eng.* **2017**, *302* (5), 1–8. https://doi.org/10.1002/mame.201600497.
(17) Inal, S.; Rivnay, J.; Hofmann, A. I.; Uguz, I.; Mumtaz, M.; Katsigiannopoulos, D.; Brochon, C.; Cloutet, E.; Hadziioannou, G.; Malliaras, G. G. Organic Electrochemical Transistors Based on PEDOT with Different Anionic Polyelectrolyte Dopants. *J. Polym. Sci. Part B Polym. Phys.* **2016**, *54* (2), 147–151. https://doi.org/10.1002/polb.23938.
(18) Bischak, C. G.; Flagg, L. Q.; Yan, K.; Li, C.-Z.; Ginger, D. S. Fullerene Active Layers for N-Type Organic Electrochemical Transistors. *ACS Appl. Mater. Interfaces* **2019**, *11*, 28138–28144. https://doi.org/10.1021/acsami.9b11370.
(19) Pacheco-Moreno, C. M.; Schreck, M.; Scaccabarozzi, A. D.; Bourgun, P.; Wantz, G.; Stevens, M. M.; Dautel, O. J.; Stingelin, N. The Importance of Materials Design to Make Ions Flow: Toward Novel Materials Platforms for Bioelectronics Applications. *Adv. Mater.* **2017**, *29*, 1604446. https://doi.org/10.1002/adma.201604446.
(20) Khau, B. V; Savagian, L. R.; Keersmaecker, M. De; Gonzalez, M. A.; Reichmanis, E. Carboxylic Acid Functionalization Yields Solvent-Resistant Organic Electrochemical Transistors. **2019**. https://doi.org/10.1021/acsmaterialslett.9b00373.
(21) Koltzenburg, S.; Maskos, M.; Nuyken, O. Conjugated Electrochromic Polymers with Amide-Containing Side Chains Enabling Aqueous Electrolyte Compatibility. *Polym.*

Chem. **2019**, 1–584. https://doi.org/10.1007/978-3-662-49279-6.
(22) Inal, S.; Rivnay, J.; Leleux, P.; Ferro, M.; Ramuz, M.; Brendel, J. C.; Schmidt, M. M.; Thelakkat, M.; Malliaras, G. G. A High Transconductance Accumulation Mode Electrochemical Transistor. *Adv. Mater.* **2014**, *26*, 7450–7455. https://doi.org/10.1002/adma.201403150.
(23) Schmode, P.; Ohayon, D.; Reichstein, P. M.; Savva, A.; Inal, S.; Thelakkat, M. High-Performance Organic Electrochemical Transistors Based on Conjugated Polyelectrolyte Copolymers. *Chem. Mater.* **2019**, *31* (14), 5286–5295. https://doi.org/10.1021/acs.chemmater.9b01722.
(24) Zeglio, E.; Eriksson, J.; Gabrielsson, R.; Solin, N.; Inganäs, O. Highly Stable Conjugated Polyelectrolytes for Water-Based Hybrid Mode Electrochemical Transistors. *Adv. Mater.* **2017**, *29* (19), 6–11. https://doi.org/10.1002/adma.201605787.
(25) Savagian, L. R.; Österholm, A. M.; Ponder, J. F.; Barth, K. J.; Rivnay, J.; Reynolds, J. R. Balancing Charge Storage and Mobility in an Oligo(Ether) Functionalized Dioxythiophene Copolymer for Organic- and Aqueous- Based Electrochemical Devices and Transistors. *Adv. Mater.* **2018**, *30*, 1804647. https://doi.org/10.1002/adma.201804647.
(26) Giovannitti, A.; Thorley, K. J.; Nielsen, C. B.; Li, J.; Donahue, M. J.; Malliaras, G. G.; Rivnay, J.; McCulloch, I. Redox-Stability of Alkoxy-BDT Copolymers and Their Use for Organic Bioelectronic Devices. *Adv. Funct. Mater.* **2018**, *28*, 1706325. https://doi.org/10.1002/adfm.201706325.
(27) Rivnay, J.; Inal, S.; Collins, B. A.; Sessolo, M.; Stavrinidou, E.; Strakosas, X.; Tassone, C.; Delongchamp, D. M.; Malliaras, G. G. Structural Control of Mixed Ionic and Electronic Transport in Conducting Polymers. *Nat. Commun.* **2016**, *7*, 11287. https://doi.org/10.1038/ncomms11287.
(28) Giovannitti, A.; Sbircea, D.-T.; Inal, S.; Nielsen, C. B.; Bandiello, E.; Hanifi, D. A.; Sessolo, M.; Malliaras, G. G.; McCulloch, I.; Rivnay, J. Controlling the Mode of Operation of Organic Transistors through Side-Chain Engineering. *Proc. Natl. Acad. Sci.* **2016**, *113*, 12017–12022. https://doi.org/10.1073/pnas.1608780113.
(29) Nielsen, C. B.; Giovannitti, A.; Sbircea, D.; Bandiello, E.; Niazi, M. R.; Hani, D. A.; Sessolo, M.; Amassian, A.; Malliaras, G. G.; Rivnay, J.; et al. Molecular Design of Semiconducting Polymers for High-Performance Organic Electrochemical Transistors. *J. Am. Chem. Soc.* **2016**, *138*, 10252–10259. https://doi.org/10.1021/jacs.6b05280.
(30) Giovannitti, A.; Maria, I. P.; Hanifi, D.; Donahue, M. J.; Bryant, D.; Barth, K. J.; Makdah, B. E.; Savva, A.; Moia, D.; Zetek, M.; et al. Role of the Side Chain on the Performance of N-Type Conjugated Polymers in Aqueous Electrolytes. *Chem. Mater.* **2018**, *30*, 2945–2953. https://doi.org/10.1021/acs.chemmater.8b00321.
(31) Giovannitti, A.; Nielsen, C. B.; Sbircea, D.-T.; Inal, S.; Donahue, M.; Niazi, M. R.; Hanifi, D. A.; Amassian, A.; Malliaras, G. G.; Rivnay, J.; et al. Erratum: N-Type Organic Electrochemical Transistors with Stability in Water. *Nat. Commun.* **2016**, *7*, 13955. https://doi.org/10.1038/ncomms13955.
(32) Roncali, J.; Shi, L. I. H.; Garreau, R.; Garnier, F.; Lemaire, M.; Er, C.; Dunant, H.; Organique, C.; Cnrs, U. A. Tuning of the Aqueous Electroactivity of Substituted Poly(Thiophene)s by Ether Groups. *Synthet* **1990**, *36*, 267–273.
(33) Rivnay, J.; Inal, S.; Salleo, A.; Owens, R. M.; Berggren, M.; Malliaras, G. G. Organic Electrochemical Transistors. *Nat. Rev. Mater.* **2018**, *3*, 17086. https://doi.org/10.1038/natrevmats.2017.86.

(34) Zeglio, E.; Inganäs, O. Active Materials for Organic Electrochemical Transistors. *Adv. Mater.* **2018**, *1800941*, 1800941. https://doi.org/10.1002/adma.201800941.
(35) Inal, S.; Malliaras, G. G.; Rivnay, J. Benchmarking Organic Mixed Conductors for Transistors. *Nat. Commun.* **2017**, *8*, 1767. https://doi.org/10.1038/s41467-017-01812-w.
(36) Inal, S.; Rivnay, J.; Suiu, A. O.; Malliaras, G. G.; McCulloch, I. Conjugated Polymers in Bioelectronics. *Acc. Chem. Res.* **2018**, *51*, 1368–1376. https://doi.org/10.1021/acs.accounts.7b00624.
(37) Moser, M.; Ponder, J. F.; Wadsworth, A.; Giovannitti, A.; McCulloch, I. Materials in Organic Electrochemical Transistors for Bioelectronic Applications: Past, Present, and Future. *Adv. Funct. Mater.* **2019**, *29* (21), 1–15. https://doi.org/10.1002/adfm.201807033.
(38) Borges-González, J.; Kousseff, C. J.; Nielsen, C. B. Organic Semiconductors for Biological Sensing. *J. Mater. Chem. C* **2019**, *7* (5), 1111–1130. https://doi.org/10.1039/c8tc05900d.
(39) Flagg, L. Q.; Bischak, C. G.; Onorato, J. W.; Rashid, R. B.; Luscombe, C. K.; Ginger, D. S. Polymer Crystallinity Controls Water Uptake in Glycol Side-Chain Polymer Organic Electrochemical Transistors. *J. Am. Chem. Soc.* **2019**, *141*, 4345–4354. https://doi.org/10.1021/jacs.8b12640.
(40) Gladisch, J.; Stavrinidou, E.; Ghosh, S.; Giovannitti, A.; Moser, M.; Zozoulenko, I.; Mcculloch, I.; Berggren, M. Reversible Electronic Solid – Gel Switching of a Conjugated Polymer. **2019**, *1901144*. https://doi.org/10.1002/advs.201901144.
(41) Wang, S.; Li, F.; Easley, A. D.; Lutkenhaus, J. L. Real-Time Insight into the Doping Mechanism of Redox-Active Organic Radical Polymers. *Nat. Mater.* **2018**, *18*, 69–76. https://doi.org/10.1038/s41563-018-0215-1.
(42) Zhou, Q. X.; Kolaskie, C. J.; Miller, L. L. The Incorporation of Electrolyte Cations into Polypyrrole and Poly-3-Methylthiophene during Electrochemical Reduction. *J. Electroanal. Chem.* **1987**, *223* (1–2), 283–286. https://doi.org/10.1016/0022-0728(87)85267-1.
(43) Reynolds, J. R.; Pyo, M.; Qiu, Y. J. Cation and Anion Dominated Ion Transport during Electrochemical Switching of Polypyrrole Controlled by Polymer-Ion Interactions. *Synth. Met.* **1993**, *55* (2–3), 1388–1395. https://doi.org/10.1016/0379-6779(93)90256-V.
(44) Qiu, Y.-J.; Reynolds, J. R. Dopant Anion Controleled Ion Transport Behavior of Polypyrrole. *Polym. Eng. Sci.* **1991**, *31*, 417–421.
(45) Chao, F.; Baudoin, J. L.; Costa, M.; Lang, P. The Ionic Mecanism of the Elctrochemical Doping of Poly (3-Methylthiophene) Studied by Secondary Ion Mass Spectroscopy (SIMS). *Die Makromol. Chemie, Macromol. Symp.* **1987**, *8*, 173–194.
(46) Sauerbrey, G. Verwendung von Schwingquarzen Zur Wägung Dünner Schichten Und Zur Mikrowägung. *Zeitschrift für Phys.* **1959**, *155*, 206–222.
(47) Flagg, L. Q.; Giridharagopal, R.; Guo, J.; Ginger, D. S. Anion-Dependent Doping and Charge Transport in Organic Electrochemical Transistors. *Chem. Mater.* **2018**, *30*, 5380–5389. https://doi.org/10.1021/acs.chemmater.8b02220.
(48) Cendra, C.; Giovannitti, A.; Savva, A.; Venkatraman, V.; McCulloch, I.; Salleo, A.; Inal, S.; Rivnay, J. Role of the Anion on the Transport and Structure of Organic Mixed Conductors. *Adv. Funct. Mater.* **2018**, *29*, 1807034. https://doi.org/10.1002/adfm.201807034.
(49) Orata, D.; Buttry, D. A. Determination of Ion Populations and Solvent Content as Functions of Redox State and PH in Polvaniline. *J. Am. Chem. Soc.* **1987**, *109* (12), 3574–

3581. https://doi.org/10.1021/ja00246a013.
(50) Woyski, M. M.; Shenk Jr., W. J.; Pellon, E. R. Hexafluorphosphates of Sodium, Ammonium, and Potassium. In *Inorganic Syntheses*; Audrieth, L. F., Ed.; McGraw-Hill Book Company, Inc., 1950; Vol. 3, pp 111–117. https://doi.org/10.1017/CBO9781107415324.004.
(51) Zhang, L.; Andrew, T. L. Deposition Dependent Ion Transport in Doped Conjugated Polymer Films: Insights for Creating High-Performance Electrochemical Devices. *Adv. Mater. Interfaces* **2017**, *4*, 1700873. https://doi.org/10.1002/admi.201700873.
(52) Hillman, A. R.; Daisley, S. J.; Bruckenstein, S. Kinetics and Mechanism of the Electrochemical P-Doping of PEDOT. *Electrochem. commun.* **2007**, *9*, 1316–1322. https://doi.org/10.1016/j.elecom.2007.01.009.
(53) Hillman, A.; Daisley, S. J. S.; Bruckenstein, S.; Robert Hillman, A.; Daisley, S. J. S.; Bruckenstein, S. Solvent Effects on the Electrochemical P-Doping of PEDOT. *Phys. Chem. Chem. Phys.* **2007**, *9*, 2379–2388. https://doi.org/10.1039/b618786b.
(54) Hillman, A. R.; Daisley, S. J.; Bruckenstein, S. Ion and Solvent Transfers and Trapping Phenomena during N-Doping of PEDOT Films. *Electrochim. Acta* **2008**, *53*, 3763–3771. https://doi.org/10.1016/j.electacta.2007.10.062.

Chapter 5. Conclusions and Future Directions

We have presented three investigations into what factors control ion injection into conjugated polymers, and how presence of ions affects the electronic carriers within a mixed ionic/electronic conductor. In each case, we try to isolate a specific aspect of the system in order to develop a deeper understanding of the mixed conduction processes. The design rules outline here are derived from organic electrochemical transistors, but we believe them to be universal to all applications utilizing mixed ionic/electronic conductors.

In chapter 2, we study the role of the anion in charge compensation and transport during the electrochemical oxidation of a model p-type polymer. We show that larger ions inject into the polymer matrix more easily and to a greater extent. After correcting for the number of ions injected, we show there is an anion dependence to the electronic mobility within the film. Additionally, we show that the kinetics of ion injection are much faster when using large ions as compared to smaller ions. We believe this can be attributed to the fact that that large ions enter polymers with very little hydration, as opposed to small ions which can enter with ~10 waters. Finally, we show that electrochemical strain microscopy is sensitive to the ion dependent injection that we observe in the bulk measurements.

In chapter 3, we a material with near record figures of merit for mixed ionic/electronic conduction. We first show that even in this good mixed conductor, larger ions are able to inject at a lower potential relative to small ions. Interestingly, the anion dependence of the kinetics is greatly reduced in this system compared to the poor mixed conductor studied in chapter 2. We attribute this to differences in hydration of the polymer lattice due to the hydrophilic side chain on the good conductor. Finally, we explore how the polymer crystallinity affects OECT operation. Surprisingly we find that thermal annealing increases the performance of dry field effect transistors but is

detrimental to OECT performance. We attribute this to heterogenous ion uptake in the annealed film leading to disruption of electronic conduction within the film.

In chapter 4, we specifically investigate the role of the cation in electrochemical doping of a highly hydrated conjugated polymer. We find that when the anion is small and does not enter the film, the cation is uninvolved in the doping process. However, when the anion is large and easily enters the film, the cation also enters the film and is an active participant in the charge compensation process associated with electrochemical oxidation. We provide direct evidence for p-type doping by cation expulsion. We speculate that this doping mechanism has strong impact on the kinetics and stability of the doped state.

Mixed ionic/electronic conductors represent an exciting class of new materials with the potential to address many pressing societal issues. The potential for improvement of these materials is dramatic. The highest mobility demonstrated by today's mixed conductors is approximately 10 $cm^2\ V^{-1}\ s^{-1}$ and the highest volumetric capacitance is on the order of 1000 F/cm^3. Combining these properties into one material would yield a material with a μC* value of 10,000 $F\ cm^{-1}\ V^{-1}\ s^{-1}$, a 30x increase over the record materials today. Such improvement would bring conjugated polymers to the point of commercialization for many of the previously mentioned applications.

However, optimizing for both good electronic mobility and high volumetric capacitance is difficult. In fact, researchers often observe a tradeoff between these two properties. In order to guide synthetic efforts, device processing optimization, and device design aspects for mixed conductor applications universal structure-function relationships are needed. Given the state of the understanding of mixed conductors much of the research included here utilized bulk techniques. However, as the major design rules become clear, the need for nanoscale structure function relations will become even more pressing. Such relations will require the continued development

of techniques that can resolve ionic and electronic transport with high spatial and temporal resolution, especially *in situ* given the important role of the solvent in mixed conductor system.

Additionally, n-type mixed conductors today trail behind p-type mixed conductors by an order of magnitude. In order to realize commercial versions of some mixed conductor technologies, especially asymmetric super capacitors and OECT logic gates, researchers need n-type materials on par with record p-type materials. This is especially problematic due to the fact that the doped state for many n-type mixed conductors is unstable in air. This precludes the use of *ex situ* diagnostic techniques, and points to the pressing need for *in situ* techniques for examining the polymer microstructure, ion transport, ionic-to-electronic coupling, and electronic transport in this class of materials.

Overall, the understanding of mixed conductors has increased dramatically in the past 5 years. Further development will allow even more applications and has the potential to improve device performance by more than an order of magnitude. If such progress can be made, I fully expect to see commercial applications of mixed conductors in a wide variety of applications including neuromorphic computing, energy storage, and biosensing.

APPENDIX A.

Appendix A accompanies Chapter 2: Anion-Dependent Doping and Charge Transport in Organic Electrochemical Transistors

Anion	Ionic Radius (Å)	Anhydrous Volume* ($Å^3$)	Hydration # in bulk water	Polarizability α_0 ($Å^3$)
F^-	1.26[1]	8.4	6.7[2]	1.144[3]
Cl^-	1.68[1]	19.9	6.4[2]	3.253[3]
Br^-	1.90[1]	28.7	5.9[2]	4.748[3]
ClO_4^-	2.25[1]	47.7	3.8,[4] 4.6[5]	4.825[3]
PF_6^-	2.52[1]	68.6	1.7[6]	
$TFSI^-$	3.27[7]	146.5	~0[8,9]	6.402[3]**

Table A.1 Anion Properties Tabulated properties of the anions used in this study. As a general trend the larger ionic radius and greater the polarizability result in lower hydration numbers.

* assuming spherical anion (TFSI is a significant deviation from this)
** Value for triflate ($CFSO_3^-$), not TFSI

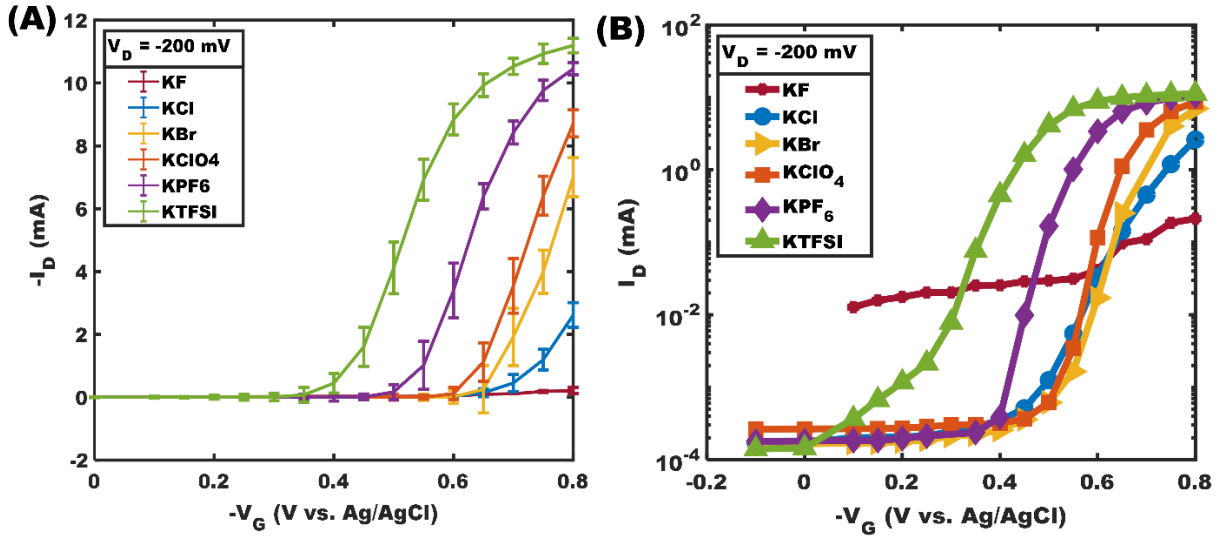

Figure A.1 Transfer curves (A) I_D vs V_G with V_D = -200 mV in 6 different electrolytes where the error bars are the standard deviation of the mean from at least 5 different transistors. (B) Transfer curve on a semi-log axis.

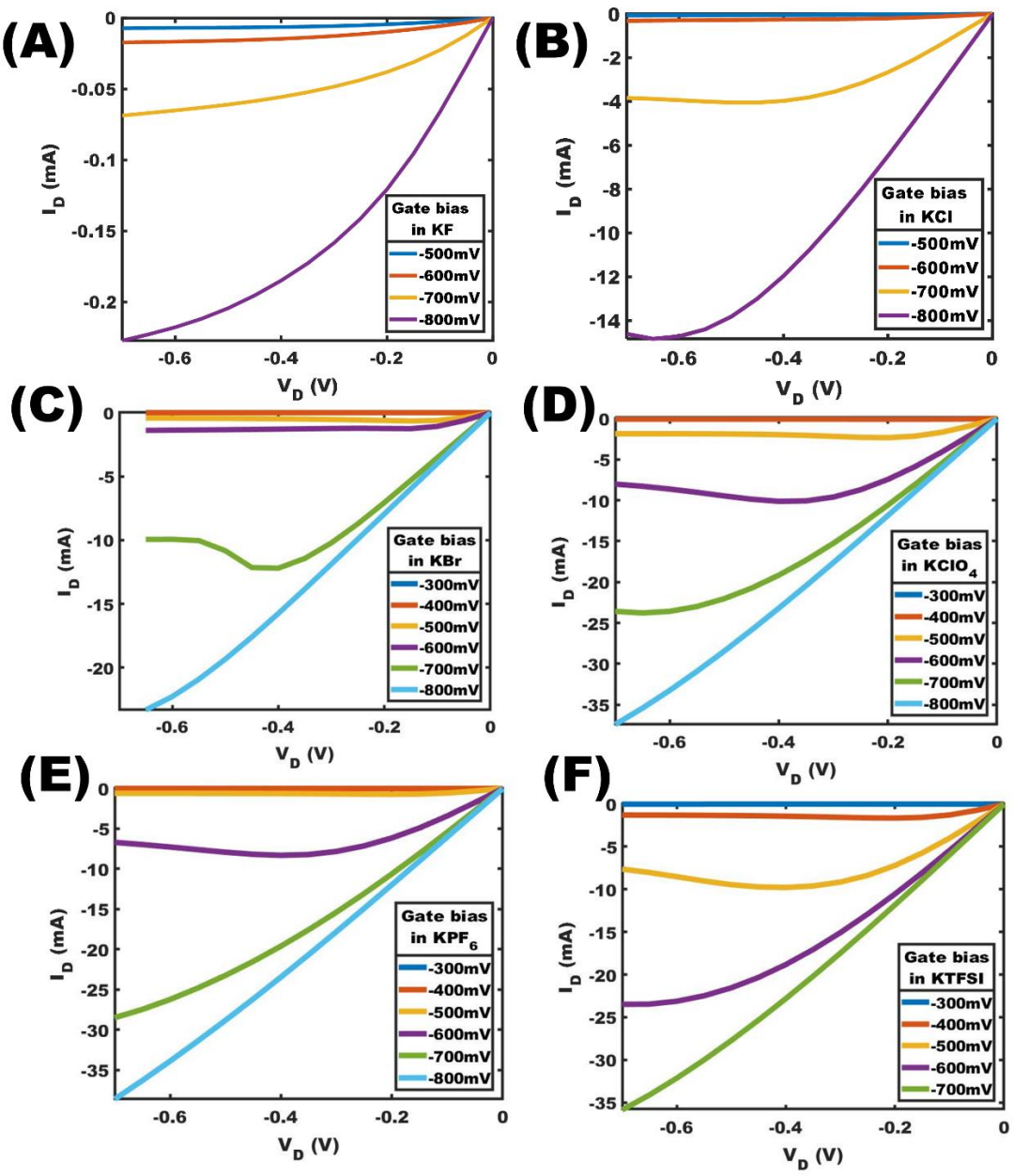

Figure A.2 Representative output curves I_D vs V_D at a series of increasing gate biases relative to Ag/AgCl in each electrolyte. The electrolyte for (A), (B), (C), (D), (E),(F) is KF, KCl, KBr, $KClO_4$, KPF_6, and KTFSI respectively.

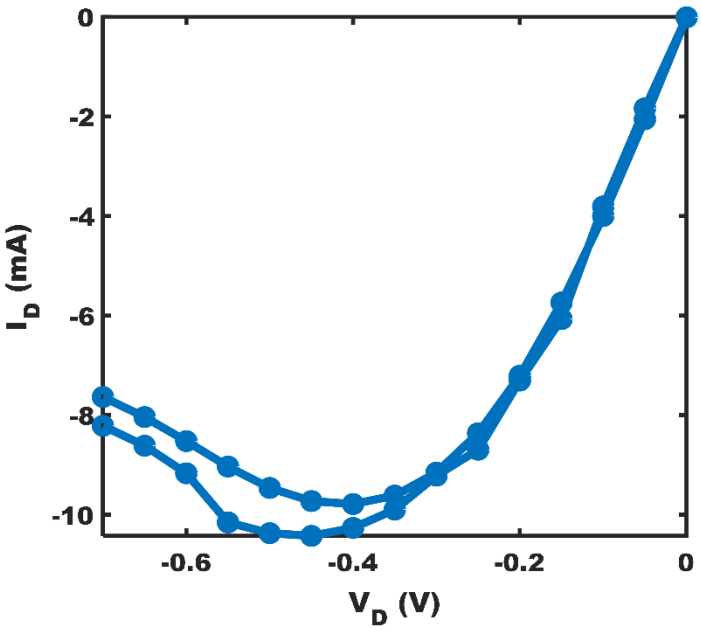

Figure A.3 Discussion of output curve shape. Forward and reverse scans at V_G = -500 mV in 20 mM KTFSI. The bate bias was applied for 500 seconds before the output curve was taken and V_D is scanned at a rate of 10 mV/s to minimize hysteresis. The non-ideal shape of the output curve is observed on both the trace and retrace.

This curvature in the output curve at certain gate voltages is something often seen in OECT literature, although not frequently discussed. Surveying the literature, this feature appears to be especially prevalent in hydrophobic materials with alkyl side chains[10–12] such as P3HT, but is also observed in the commonly used OECT material PEDOT:PSS[13] (though it isn't clear if this effect is just under-reported because it appears non ideal). We therefore speculate that this effect can be attributed to the devices operating in a mixed OECT/OFET regime. One possible explanation for this could be a spatially non-uniform hole mobility throughout the volume of the channel with regards to the transistor pinch-off. In a mixed OECT/OFET operation regime pinch off still likely occurs adjacent to the drain, but a large portion of the film is still doped electrochemically. Under certain conditions, the current could begin passing through the lower mobility regions, leading to a slight decrease in I_D with increasing V_D. Other potential explanations for the deviation from ideal saturation behavior include reaching the carrier saturation velocity of the doped polymer at high V_D or carrier repulsion at high carrier densities. We rule out the possibility that the decrease in current is due to polymer degradation because a similar shape is seen in the reverse sweep. Additionally, we do not believe this to be a kinetic effect due to the very slow scan rates used herein.

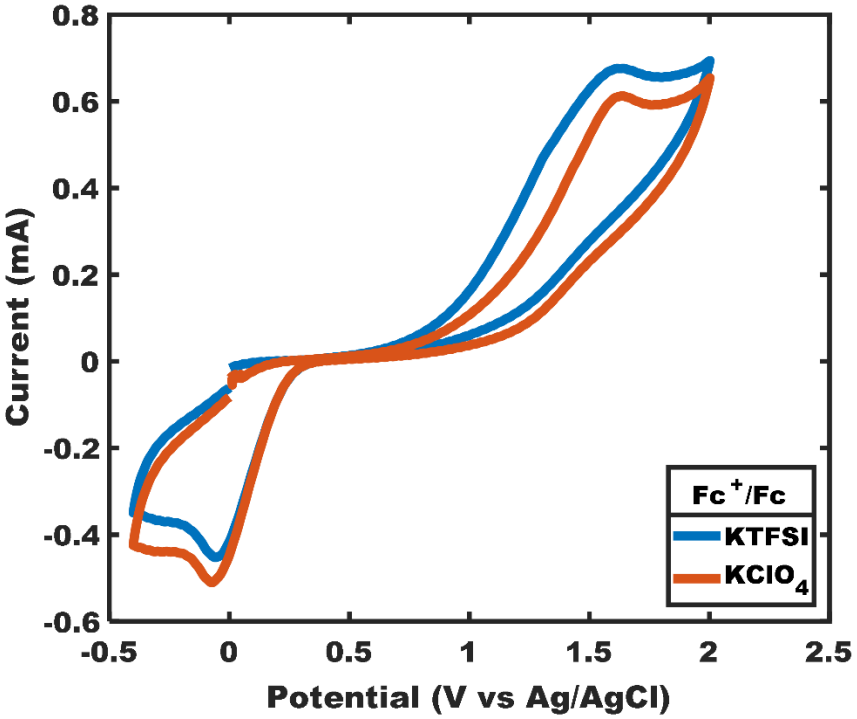

Figure A.4 Ferrocene/Ferrocenium redox couple Current as a function of potential in 20 mM KTFSI and KClO4 in acetonitrile showing the oxidation peak of ferrocene does not drift relative to the potential of the Ag/AgCl reference electrode in the different electrolytes. P3HT coated FTO is used as the working electrode and a platinum wire is used as the counter electrode. Scans are performed at a rate of 50 mV/s.

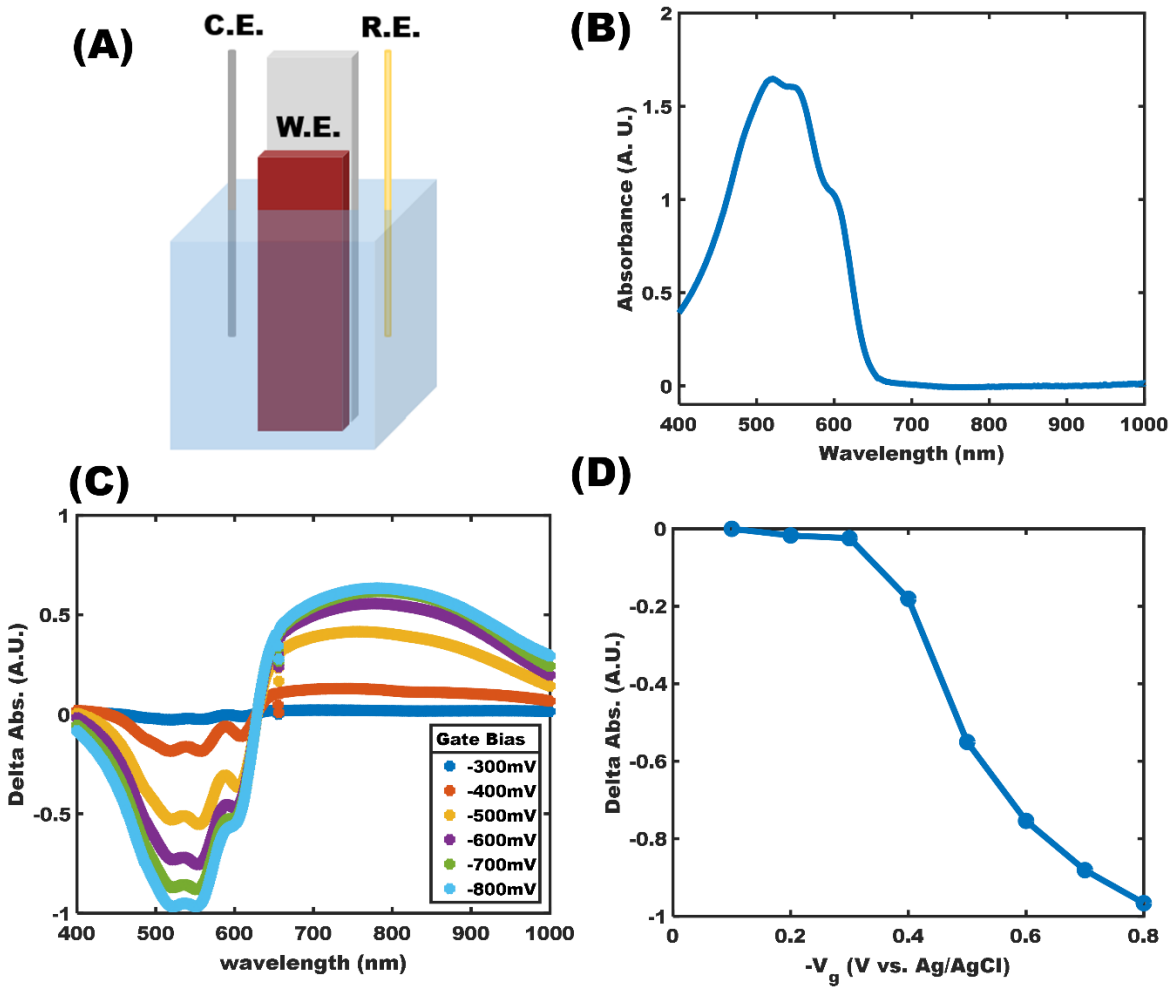

Figure A.5 Determining doping level by spectroelectrochemistry. (A) Experiment schematic, where polymer coated FTO is used as the working electrode in a 3 electrode electrochemical cell. (B) Absorbance as a function of wavelength for the as cast P3HT film. (C) Representative change in absorption relative to the undoped state as a function of wavelength in KTFSI for a range of gate biases. (D) Change in absorption at the polymer peak (552 nm) as a function of gate bias extracted from Figure A.4C.

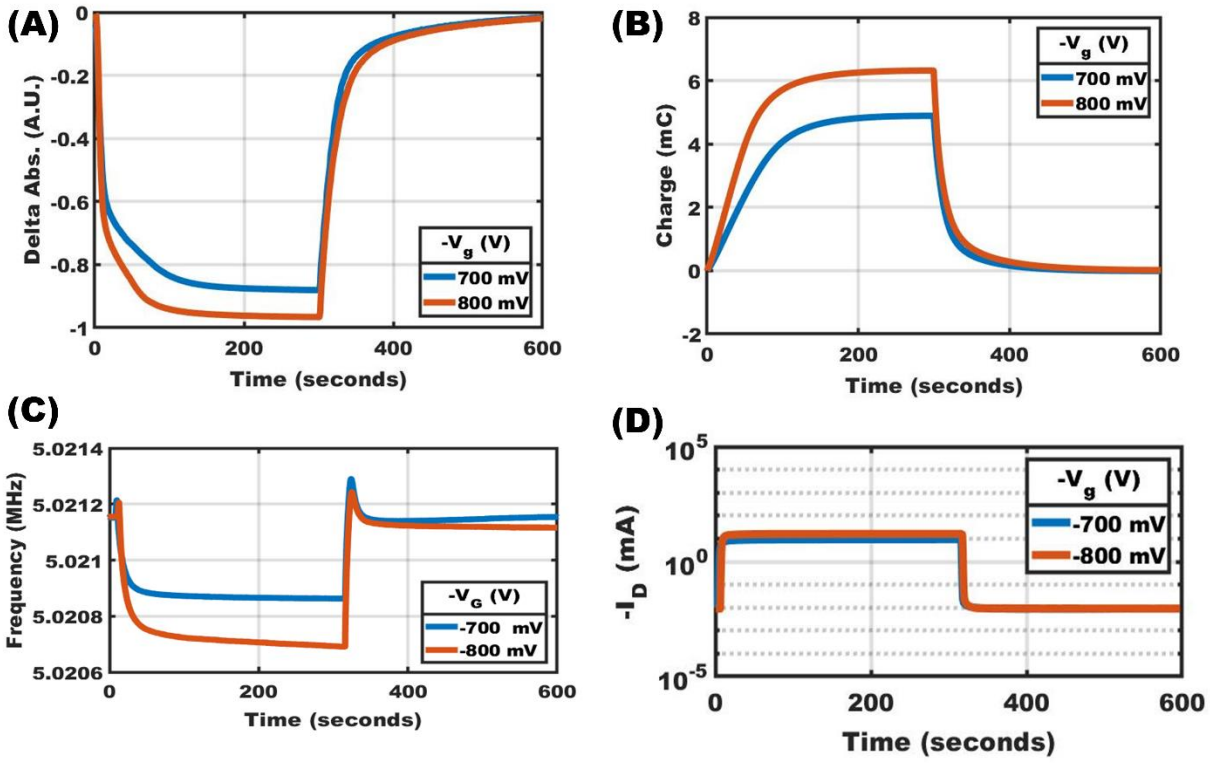

Figure A.6 Reversibility of doping (A) Shows the polymer absorption at 552 nm over time where a doping bias is applied for the first 300 seconds and a dedoping bias (V_G = +0.4) for the remaining 300 seconds showing that the absorption fully recovers to its initial value. (B) Shows the charge consumed by the oxidation/reduction of the film. The amount of charge into the film during oxidation matches the charge that leaves the film during reduction. (C) QCM frequency in response to a doping and dedoping bias, showing the oscillator frequency returns to its original state when dedoped. (D) Transistor current in response to a doping, then dedoping bias. The transistor current after dedoing matches the initial current before doping. These measurements together give us confidence in the reversibility of the doping/dedoping processes within the bias range we use.

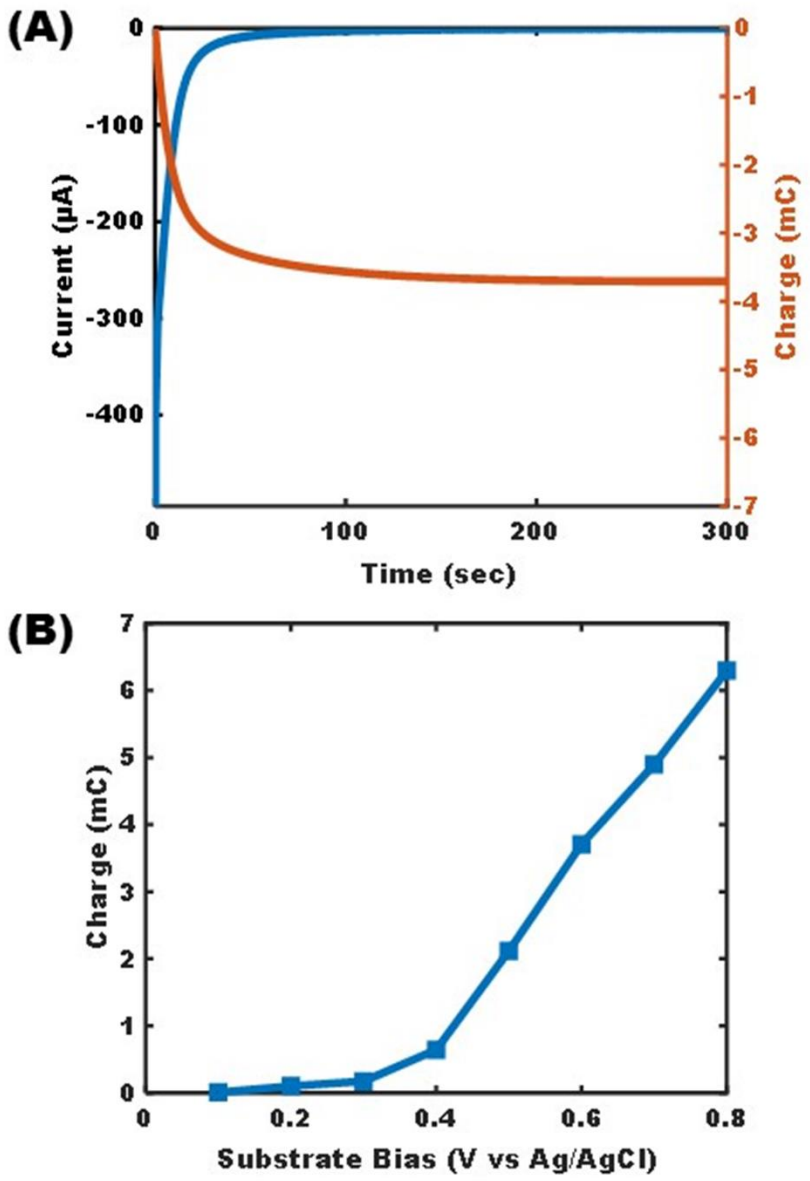

Figure A.7 Determination of doping by coulometry (A) The blue line shows the current over time as the film is reduced. Integrating the current over time allows us to calculate the charge consumed (orange line) by oxidation/reduction of the film at a given gate bias step. (B) Charge consumed by the oxidation/reduction of the films at a series of gate biases, created by performing the measurement showing in Figure A.6A and taking the steady state charge at a series of doping steps.

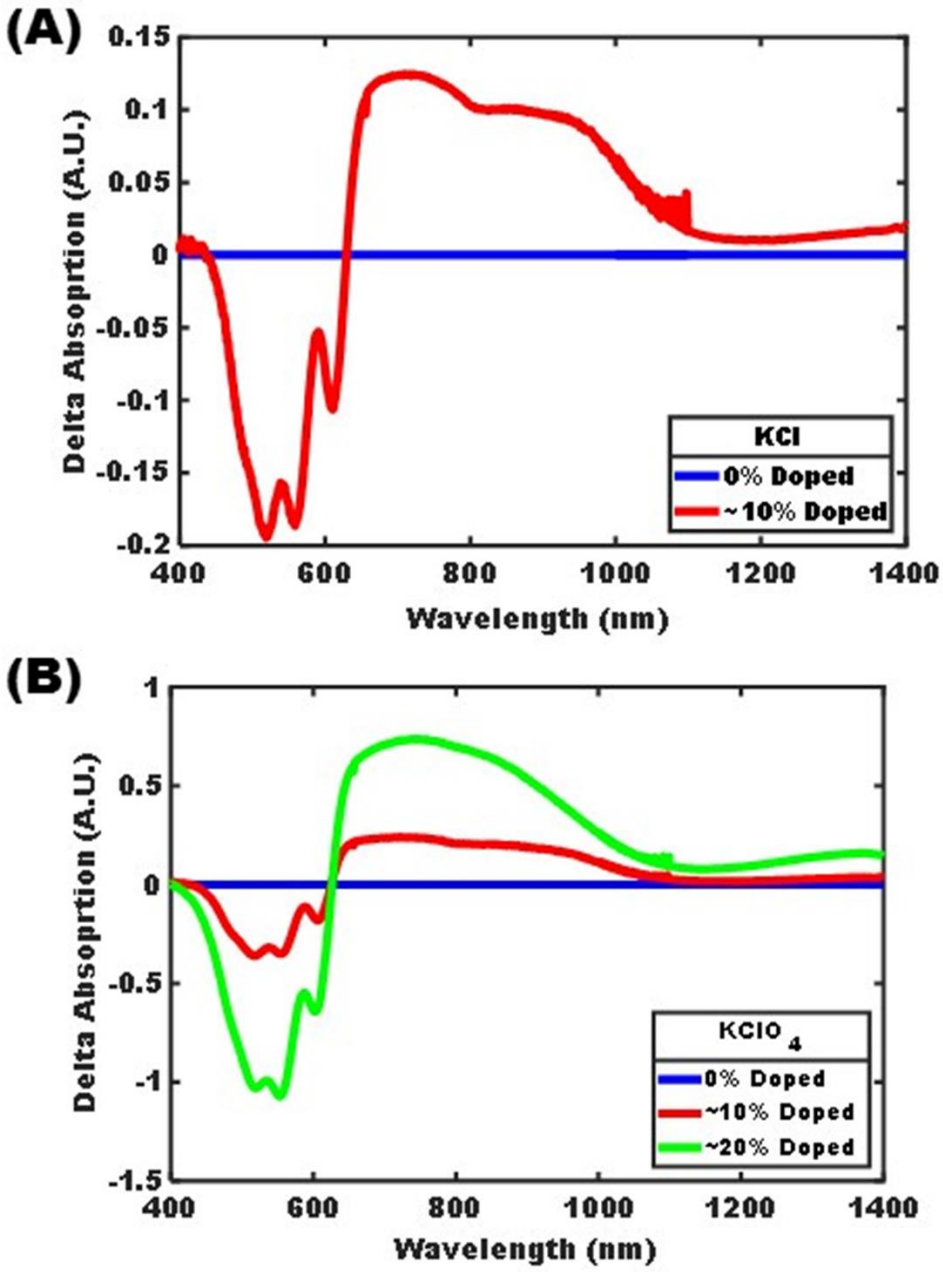

Figure A.8 Bipolaron Spectra (A) Shows the change in absorption relative to the dedoped state in KCl over a wide wavelength range, where the bipolaron feature is apparent as a broad absorption feature at 1400 nm. (B) Shows change in absorption in $KClO_4$, where at 20 % doping there is a substantial bipolaron feature apparent from 1200-1400 nm.

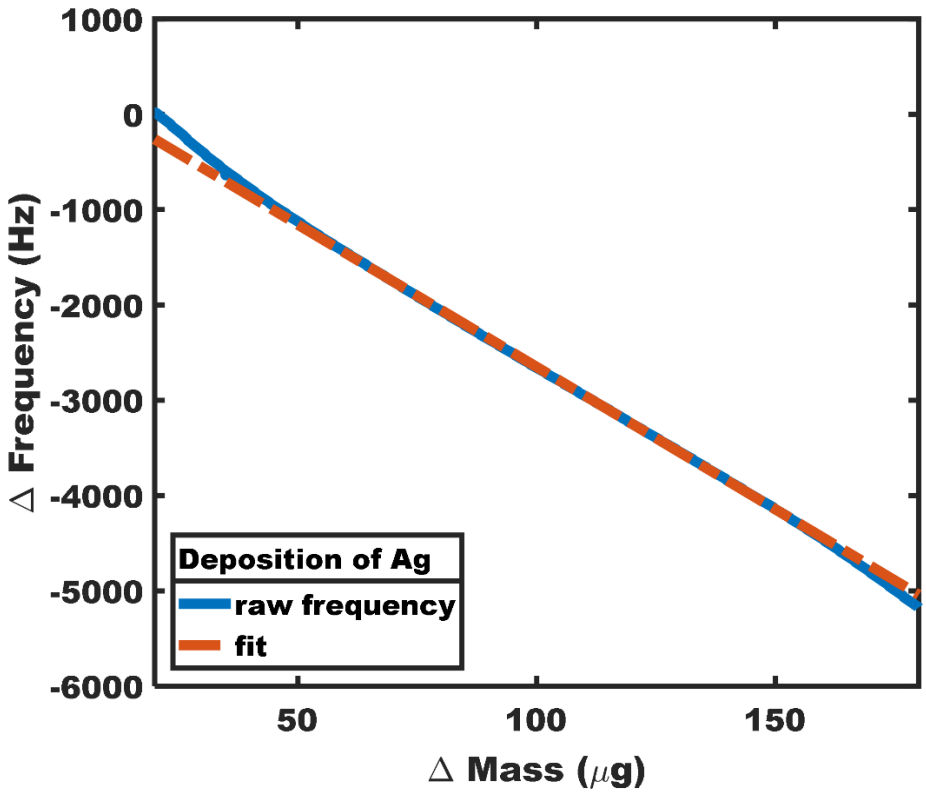

Figure A.9 Calibration of QCM sensitivity factor Change in frequency (blue) in response to the change of mass due to electrochemical deposition of silver from $AgNO_3/HNO_3$ solution at 200 uA constant current and the fit (orange) used to extract the sensitivity factor.

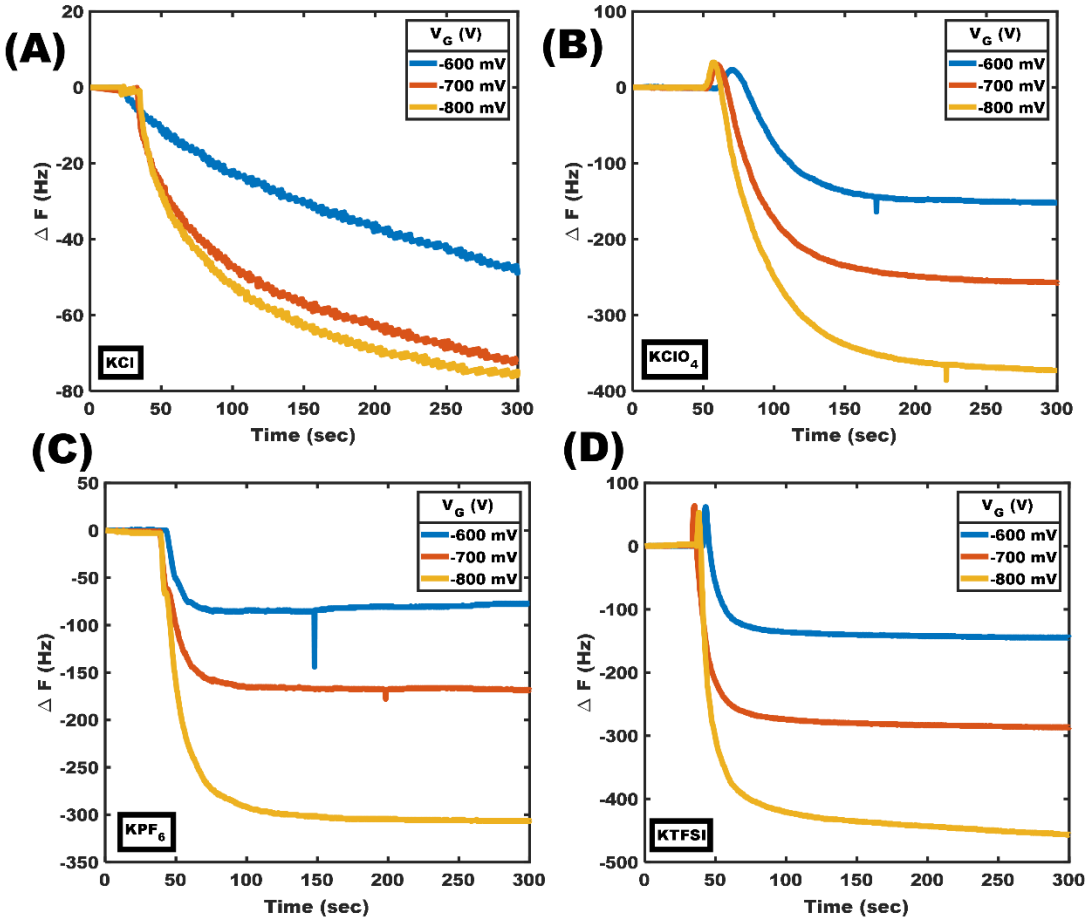

Figure A.10 QCM potential step data (A) Change in frequency over time for a P3HT coated QCM crystal in 20 mM KCl for gate biases of -0.6 V (blue), -0.7 V (orange), and -0.8 V (yellow) relative to Ag/AgCl. (B) Similar data taken in $KClO_4$. (C) Similar data taken in KPF_6. (D) Similar data taken in KTFSI.

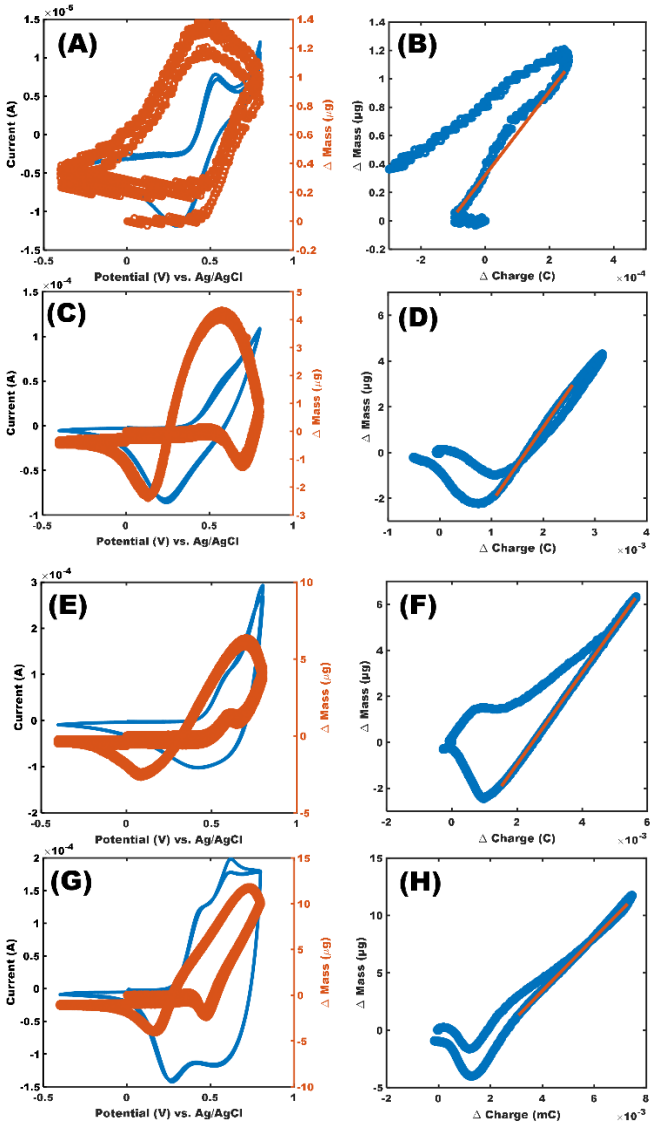

Figure A.11 Cyclic voltammetry method of dopant mass determination (A)(C)(E)(G) show cyclic voltammetry trace (blue) with a simultaneous massogram (orange) taken at 10 mV/s in KCl, $KClO_4$, KPF_6, and KTFSI respectively. (B)(D)(F)(H) show change in mass as a function of charge consumed (blue) with the fit (orange) to the linear region of the curve for KCl, $KClO_4$, KPF_6, and KTFSI respectively.

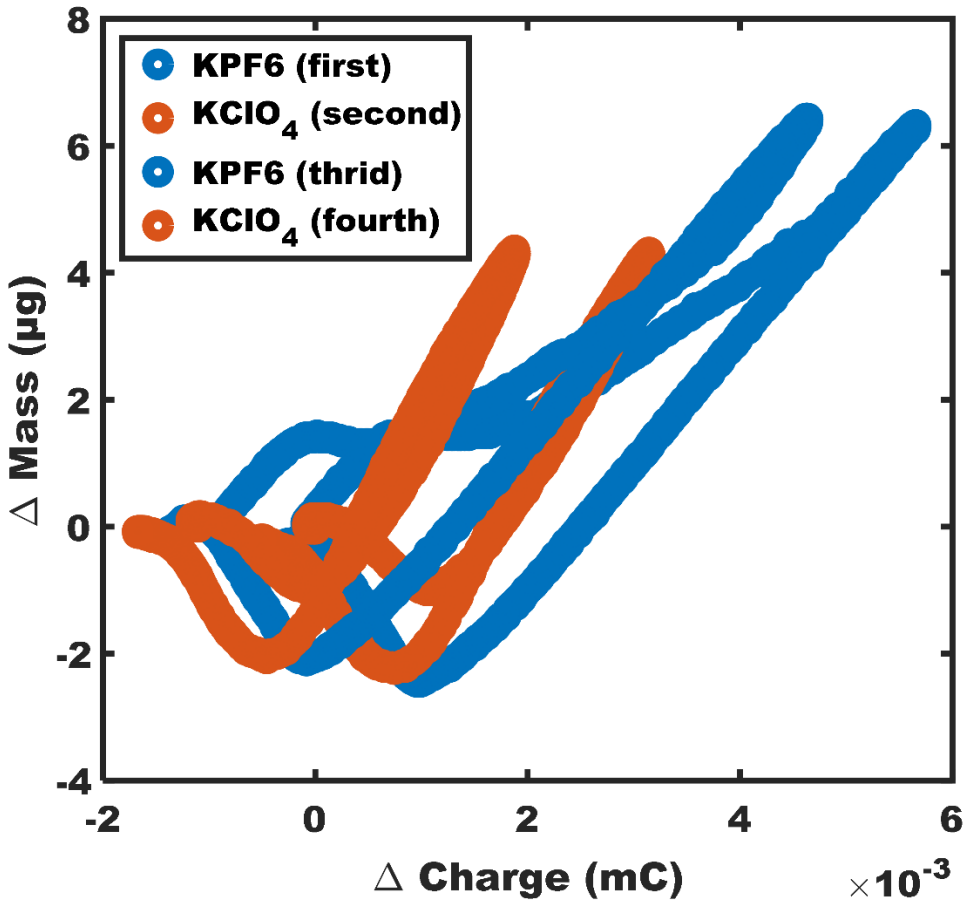

Figure A.12 Reversibility of dopant mass determination Shows the change in mass as a function of charge consumed for one sample first measured in KPF6, then KClO4, then back in KPF6, and finally back in KClO4. The slope of the linear region (proportional to the dopant molar mass) is the repeatable for both anions regardless of order the film is tested in. This suggests that the film is permselective and we are not observing the molar mass of K^+ ions moving into the film.

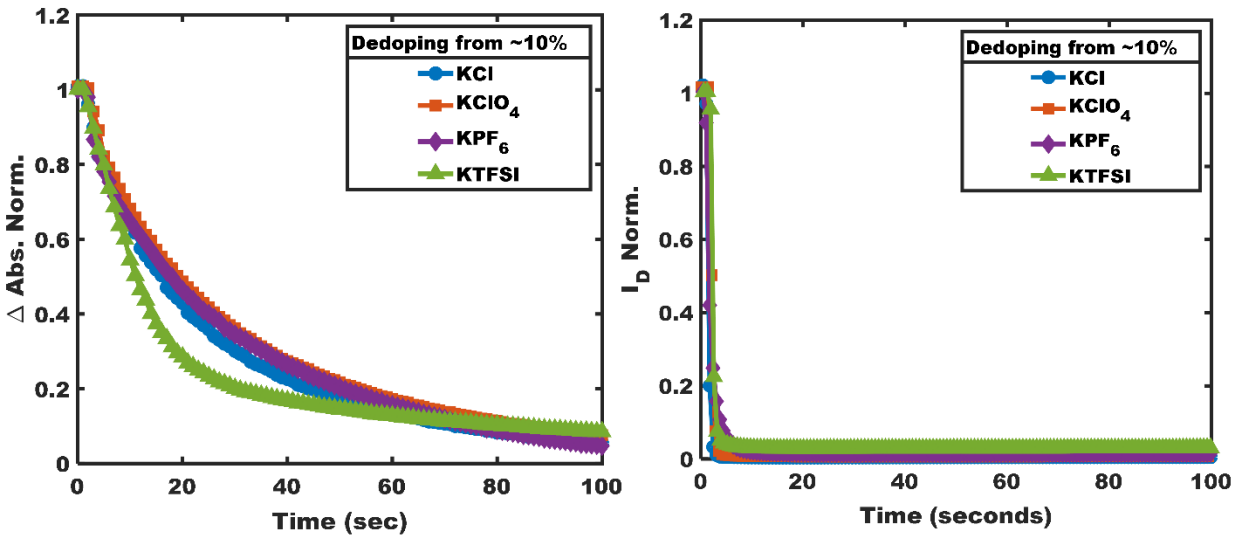

Figure A.13 Dedoping kinetics (A) Change in absorption over time in response to a reducing (dedoping) bias of +0.4 V. The dedoping is significantly faster than the doping process (Figure 2.4) and the anion dependence is greatly reduced. (B) Transistor current over time with the application of a reducing (dedoping) bias of 0.4 V. The transistor turns off in the first few seconds after the bias is applied, significantly faster than the absorption recovers.

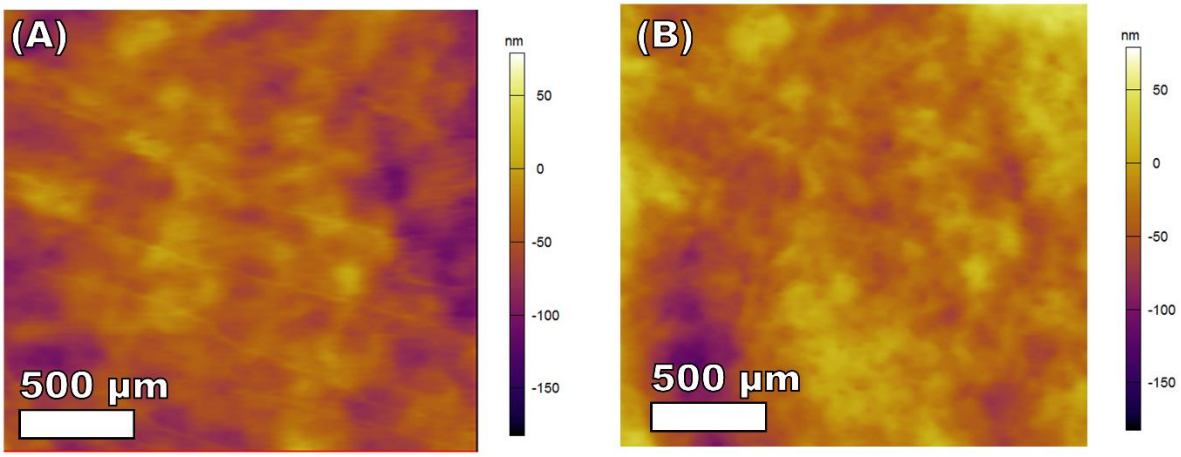

Figure A.14 Topography for ESM images (A) Topography of the film taken simultaneously with the ESM measurement taken in Figure 2.5A. (B) Topography of the film in the same area as (A) taken during the ESM measurement in Figure 2.5B.

Anion	Threshold Voltage (V)	Doping at 800 mV (carriers cm^{-3})	Mobility onset (charge /thiophene)	Hydration Number	Hydrated Volume ($Å^3$)*	Doping Kinetics	ESM Amplitude (nm)
Cl	-0.65	4.1×10^{20}	.001	10.5	135	Slow	0.5
ClO_4	-0.60	6.2×10^{20}	0.003	12.8	197	Slow	2.1
PF_6	-0.47	7.9×10^{20}	0.02	2.1	91	Fast	2.4
TFSI	-0.35	9.0×10^{20}	0.01	0.5	152	Fast	3.0

Table A.2 Summary of measured properties

The kinetics do not appear to track with hydrated volume, KCl is the 2nd smallest by volume but the slowest kinetically. $KClO_4$ is the largest ion, but is also slow kinetically.

Mobility increase onset appears to be inversely related to the hydrated volume. ClO_4^- has the largest hydrated volume and the mobility begins increasing at the lowest doping level. PF_6 has the smallest hydrated volume and causes the hole mobility to begin increasing at the highest doping density.

* anhydrous volume + (measured hydration #) x (volume of water)

Electrolyte	Concentration (mM)
KF	19.40 ± 1.02
KCl	19.61 ± 1.07
KBr	19.71 ± 1.50
$KClO_4$	19.96 ± 1.41
KPF_6	19.77 ± 1.31
KTFSI	19.70 ± 1.46

Table A.3 Confirmation of Solution Concentration Inductively Coupled Plasma- Optical Emission Spectrophotometer measurements confirming that solutions used in this work are in fact 20 mM.

REFERENCES

(1) Roobottom, H. K.; Jenkins, H. D. B.; Passmore, J.; Glasser, L. Thermochemical Radii of Complex Ions. *J. Chem. Educ.* **1999**, *76*, 1570.

(2) Soper, A. K.; Weckström, K. Ion Solvation and Water Structure in Potassium Halide Aqueous Solutions. *Biophys. Chem.* **2006**, *124*, 180–191.

(3) Li, M.; Zhuang, B.; Lu, Y.; Wang, Z. G.; An, L. Accurate Determination of Ion Polarizabilities in Aqueous Solutions. *J. Phys. Chem. B* **2017**, *121*, 6416–6424.

(4) Bergstroem, P. A.; Lindgren, J.; Kristiansson, O. An IR Study of the Hydration of Perchlorate, Nitrate, Iodide, Bromide, Chloride and Sulfate Anions in Aqueous Solution. *J. Phys. Chem.* **1991**, *95*, 8575–8580.

(5) Kristiansson, O.; Lindgren, J.; De Villepin, J. A Quantitative Infrared Spectroscopic Method for the Study of the Hydration of Ions in Aqueous Solutions. *J. Phys. Chem.* **1988**, *92*, 2680–2685.

(6) Śmiechowski, M.; Gojlo, E.; Stangret, J. Ionic Hydration in $LiPF_6$, NaPF6, and KPF6 Aqueous Solutions Derived from Infrared HDO Spectra. *J. Phys. Chem. B* **2004**, *108*, 15938–15943.

(7) Tominaga, Y.; Yamazaki, K.; Nanthana, V. Effect of Anions on Lithium Ion Conduction in Poly(Ethylene Carbonate)-Based Polymer Electrolytes. *J. Electrochem. Soc.* **2015**, *162*, A3133–A3136.

(8) Orädd, G.; Edman, L.; Ferry, A. Diffusion: A Comparison between Liquid and Solid Polymer LiTFSI Electrolytes. *Solid State Ionics* **2002**, *152–153*, 131–136.

(9) Johansson, P.; Gejji, S. P.; Tegenfeldt, J.; Lindgren, J. The Imide Ion: Potential Energy Surface and Geometries. *Electrochim. Acta* **1998**, *43*, 1375–1379.

(10) Pappa, A.-M.; Ohayon, D.; Giovannitti, A.; Maria, I.; Savva, A.; Uguz, I.; Rivnay, J.; McCulloch, I.; Owens, R.; Inal, S. Direct Metabolite Detection with an N-Type Accumulation Mode Organic Electrochemical Transistor. *Sci. Adv.* **2018**, *4*, eaat0911.

(11) Giovannitti, A.; Sbircea, D.-T.; Inal, S.; Nielsen, C. B.; Bandiello, E.; Hanifi, D. A.; Sessolo, M.; Malliaras, G. G.; McCulloch, I.; Rivnay, J. Controlling the Mode of Operation of Organic Transistors through Side-Chain Engineering. *Proc. Natl. Acad. Sci.* **2016**, *113*, 12017–12022.

(12) Giovannitti, A.; Thorley, K. J.; Nielsen, C. B.; Li, J.; Donahue, M. J.; Malliaras, G. G.; Rivnay, J.; McCulloch, I. Redox-Stability of Alkoxy-BDT Copolymers and Their Use for Organic Bioelectronic Devices. *Adv. Funct. Mater.* **2018**, *28*, 1706325.

(13) Nilsson, D.; Kugler, T.; Svensson, P. O.; Berggren, M. An All-Organic Sensor-Transistor Based on a Novel Electrochemical Transducer Concept Printed Electrochemical Sensors on Paper. *Sensors Actuators, B Chem.* **2002**, *86*, 193–197.

APPENDIX B.

Appendix B accompanies Chapter 3: Polymer Crystallinity Controls Water Uptake in Glycol Side Chain Polymer Organic Electrochemical Transistors

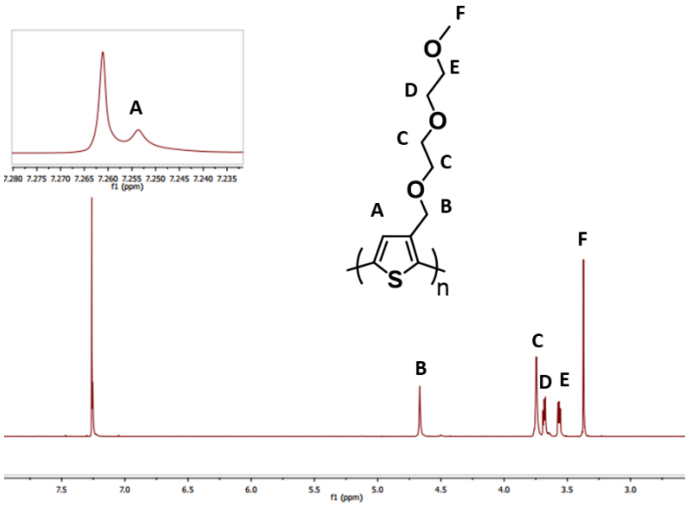

Figure B.1: ^{1}H NMR of P3MEEMT, with polymer backbone peak labels. The inset shows the aromatic proton, labelled "A", which overlaps with the residual $CHCl_3$ peak.

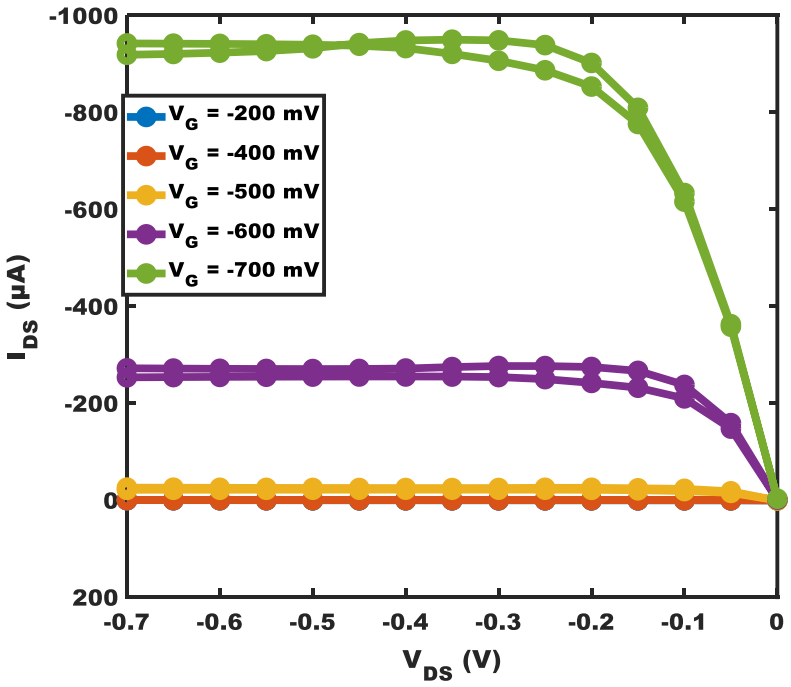

Figure B.2: Output curves for P3MEEMT in 100 mM KCl.

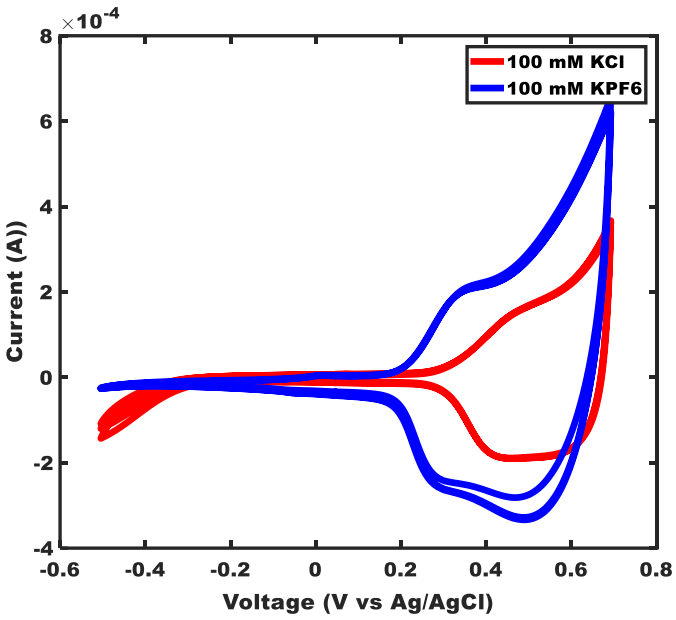

Figure B.3: Cyclic voltammetry (CV) curves for P3MEEMT with 100 mM KCl and 100 mM KPF_6 taken at 50 mV/s with an Ag/AgCl reference electrode and a platinum counter electrode. We note that CVs show an increase in current at lower potential than the threshold voltage for device measurements due to the low mobility of charges at low dopant concentration.

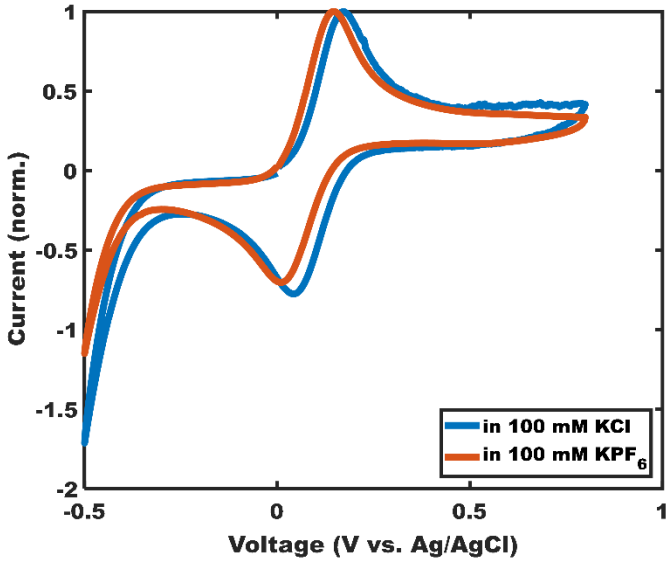

Figure B.4: Cyclic voltammetry of ferrocene in the two different electrolytes used in this study (Ag/AgCl reference electrode, platinum mesh counter electrode, FTO working electrode, scan rate 0.1 V s^{-1}. The oxidation peak appears at 169 mV in 100 mM KCl and is shifted to 152 mV in 100 mM KPF_6. This difference is small compared to the observed threshold voltage shift (126 mV).

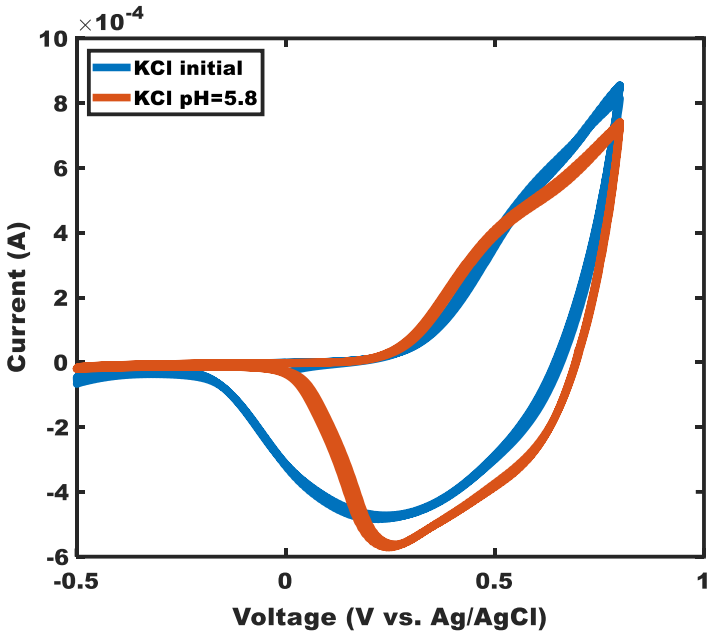

Figure B.5: Cyclic voltammetry of P3MEEMT (Ag/AgCl reference electrode, platinum mesh counter electrode, FTO working electrode, scan rate 0.1 V s^{-1}) in neutral KCl solution and pH adjusted KCl solution. We measure a pH of 5.8 for 100 mM KPF_6 solution. We then adjust the pH of 100 mM KCl solution to 5.8 by addition of HCl. By comparing the CV curve of the neutral KCl and the pH adjusted KCl we see that the onset of oxidation does not shift significantly, and therefore conclude the difference in pH does not play a large role in the observed differences between the two electrolytes.

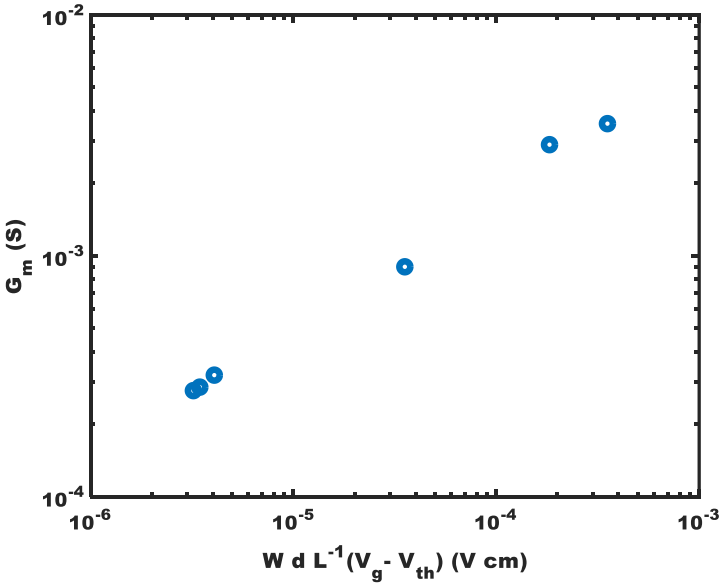

Figure B.6: µC* determination of P3HT from OECT measurements

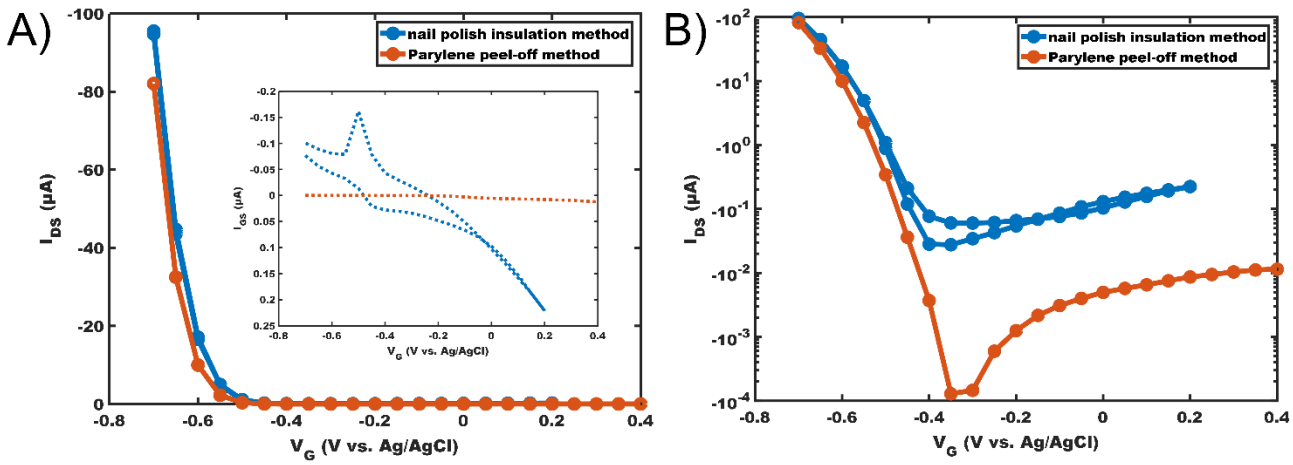

Figure B.7: Comparison of devices with our nail polish isolation method (20 µm by 200 µm dimensions) and the previously reported parylene peel-off method.[3] (10 µm by 100 µm dimensions) (A) Transfer curves of the nail polish insulation method and parylene peel-off methods of P3MEEMT of the same thickness in 100 mM KCl. The inset shows the leakage current. (B) Device data on a semilog scale showing that at high doping levels the 2 isolation methods display nearly identical current and transconductance, but the nail polish isolation results in a significantly higher leak current. For measuring µC*, the nail polish insulation method devices work well. However, for improved on-off ratio or reduced leak current, phototopographically defined active areas are important.

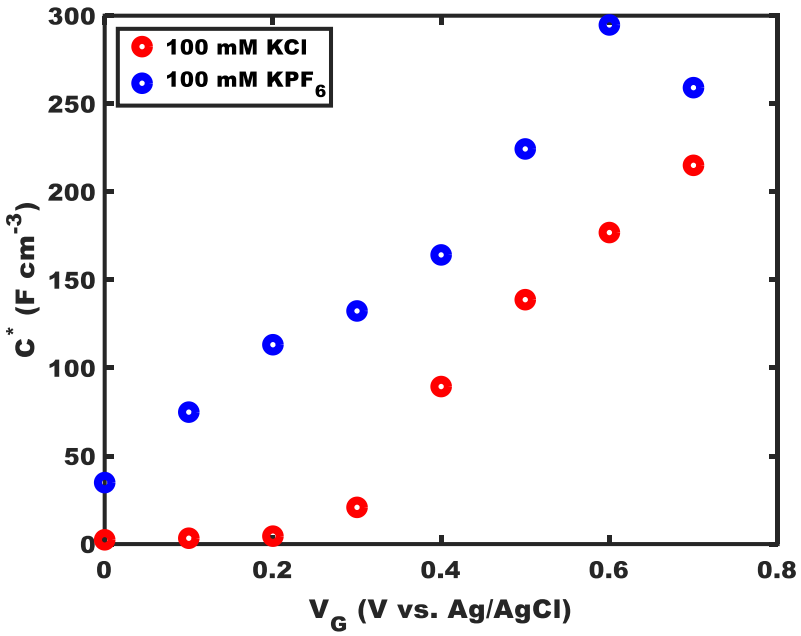

Figure B.8: Comparison of the volumetric capacitance of P3MEEMT films in 100 mM KCl and 100 mM KPF_6 electrolyte by electrochemical impedance spectroscopy (EIS).

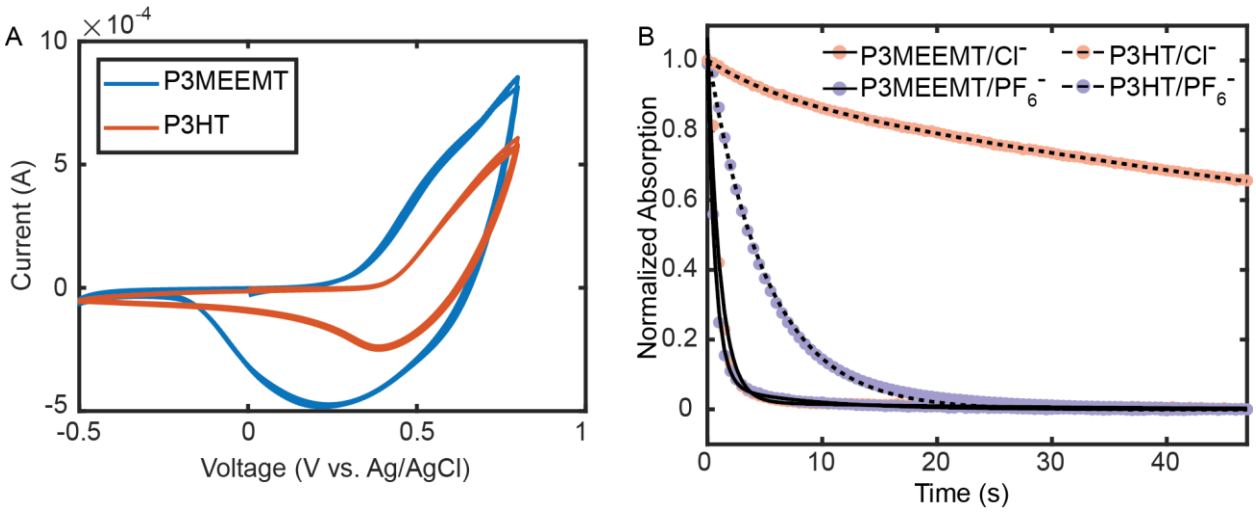

Figure B.9: (A) CV of P3MEEMT and P3HT in 100 mM KCl. We observe a ~200 mV shift in the onset of oxidation between the two polymers. (B) UV-Vis kinetics upon electrochemical doping for P3HT (0.5 V vs Ag/AgCl) and P3MEEMT (0.7 V vs Ag/AgCl) in 100 mM KCl and 100 mM KPF_6 with the corresponding biexponential fits. After correcting for the shift in the onset of the onset of oxidation for P3MEEMT and P3HT, the clear differences in ion injection kinetics between the two polymers are retained.

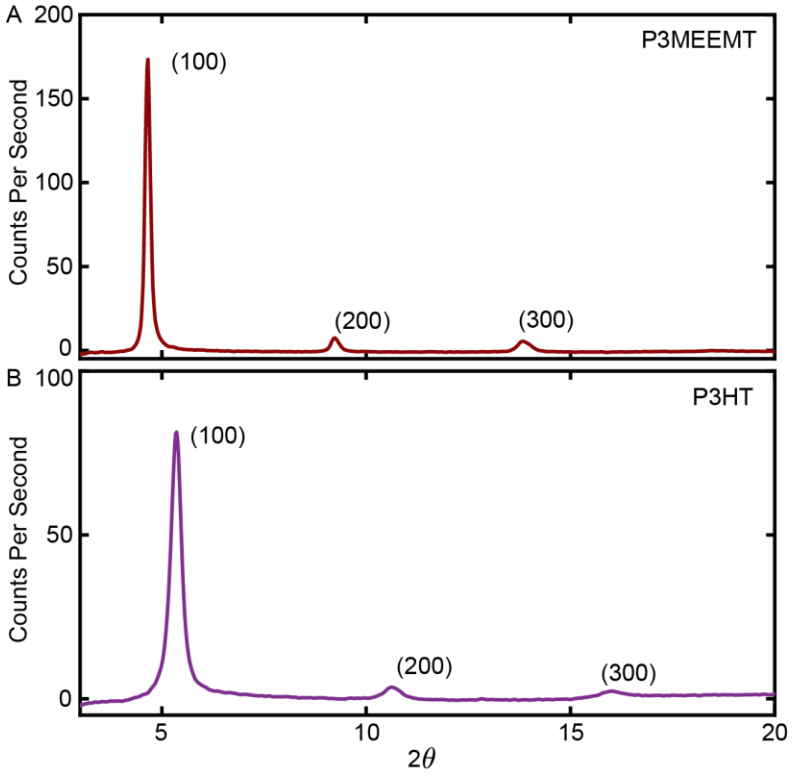

Figure B.10: GIXRD pattern of (A) P3MEEMT and (B) P3HT drop cast samples annealed at 160 °C on glass.

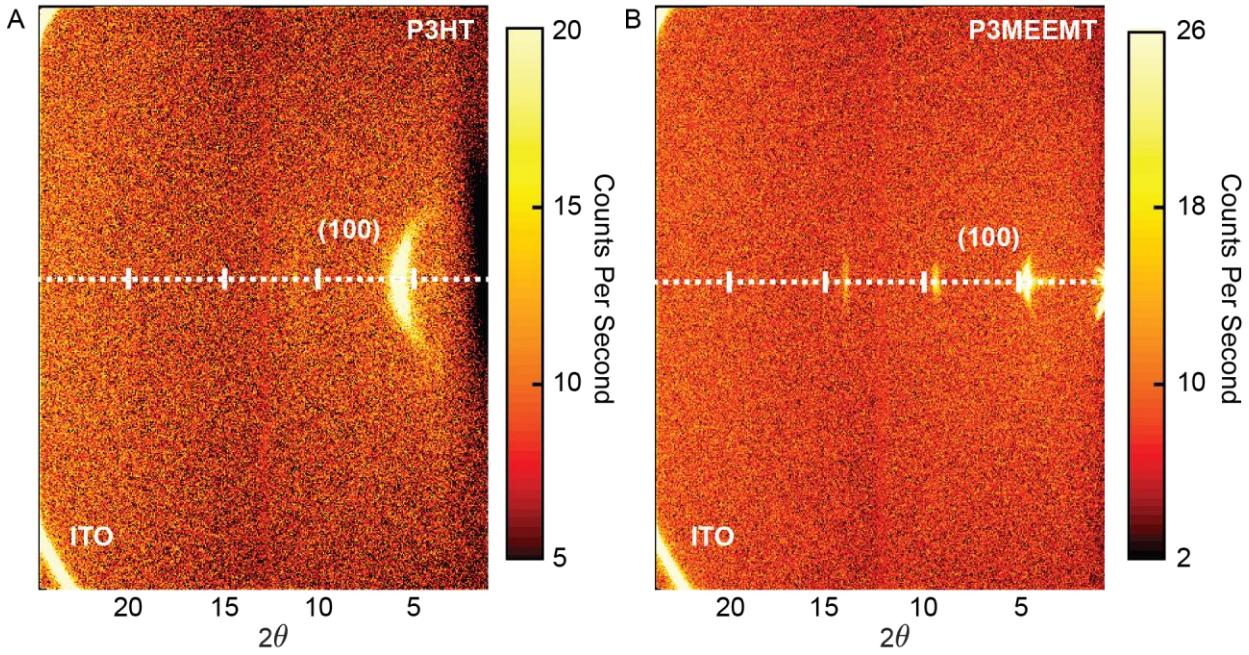

Figure B.11: 2D XRD patterns of (A) P3HT and (B) P3MEEMT thin films showing preferential orientation of the lamellar stacking.

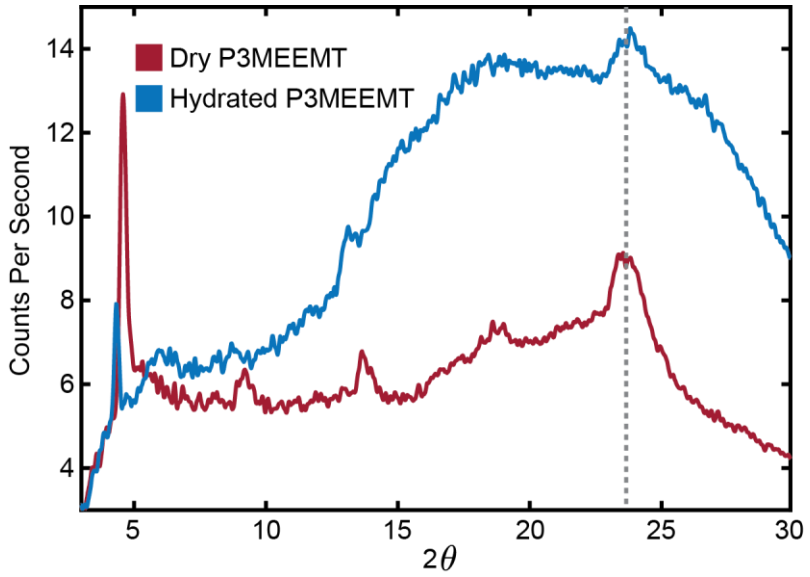

Figure B.12: GIXRD in-plane π-π stacking peak of annealed P3MEEMT dry and hydrated, which was dropcast on an Si substrate. The large background in the trace for the hydrated P3MEEMT is from water and polyimide.

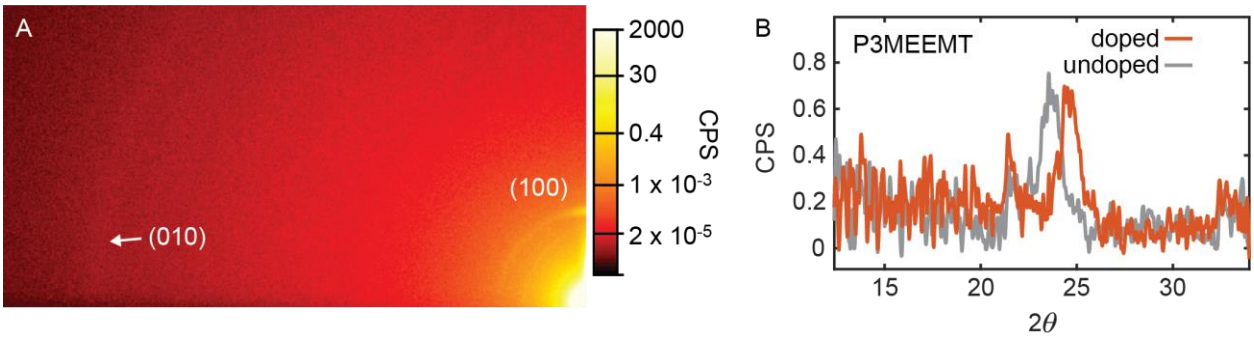

Figure B.13: Comparing the position of the pi-pi stacking peak in undoped and doped P3MEEMT. (A) 2D GIXRD of a doped drop cast P3MEEMT film. (B) Polar integration of the (010) peak corresponding to the pi-pi stacking distance with the undoped P3MEEMT pi-pi stacking peak shown in grey for reference. The pi-pi stacking distance decreases from 3.76 Å to 3.63 Å upon doping at 0.7 V in 100 mM KPF_6.

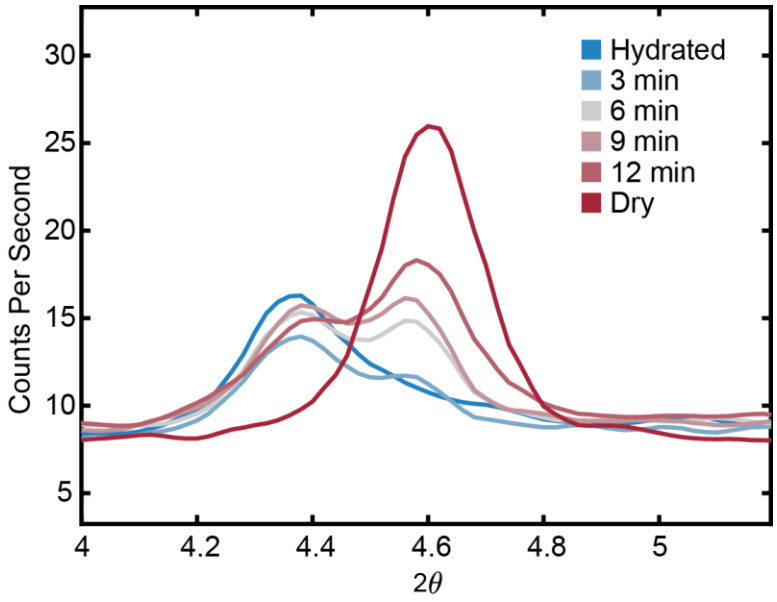

Figure B.14: Reversibility of the shift in the (100) GIXRD peak of P3MEEMT upon film drying

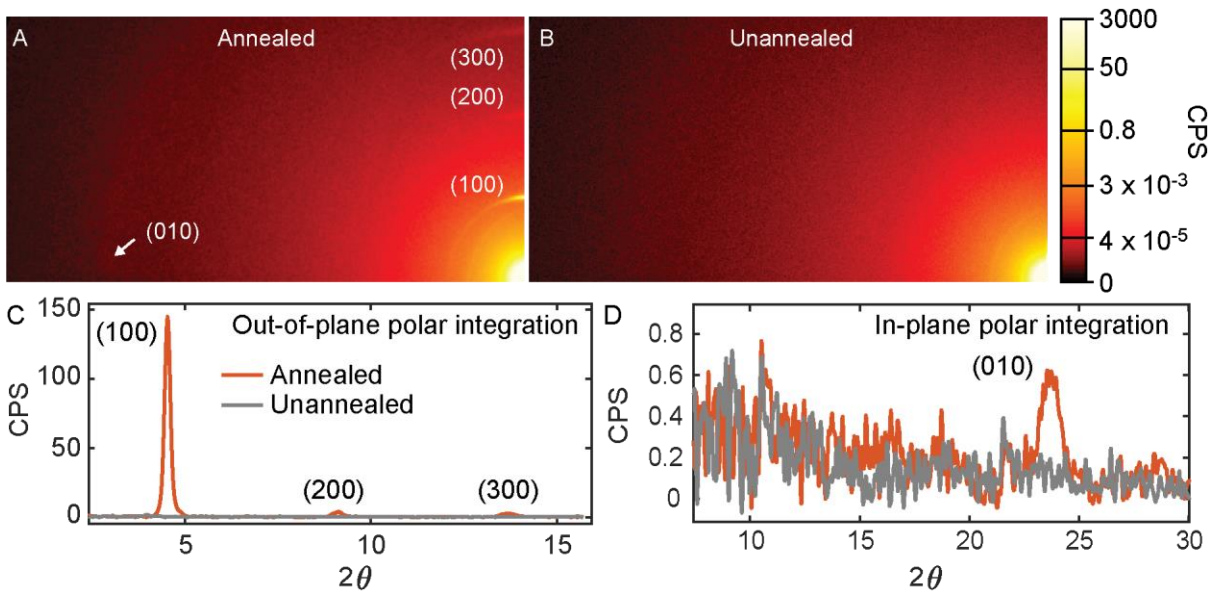

Figure B.15: 2D GIXRD and associated polar integration showing the out-of-plane and in-plane directions of a drop cast film of P3MEEMT. (A) 2D GIXRD of annealed P3MEEMT. (B) 2D GIXRD of unannealed P3MEEMT. Polar integration of both annealed and unannealed P3MEEMT in the (C) in-plane and (D) out-of-plane directions. Peaks corresponding to the lamellar spacing and the pi-pi stacking direction are observed for annealed P3MEEMT, but no peaks are observed for unannealed P3MEEMT.

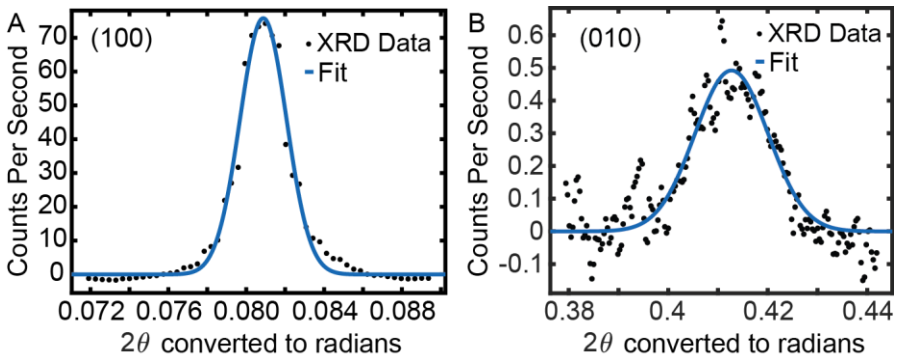

Figure B.16: Scherrer analysis of the (A) lamellar (100) and (B) π-π stacking (010) peaks and Gaussian fits of annealed P3MEEMT.

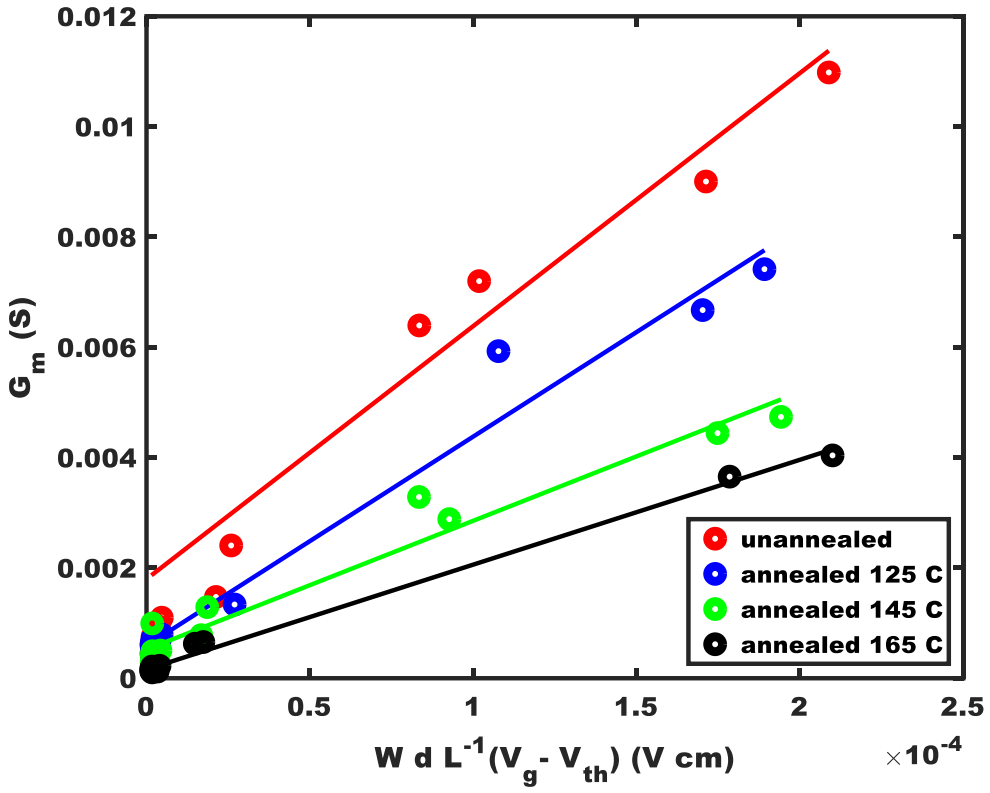

Figure B.17: Determination of μC* for each annealing temperature of P3MEEMT.

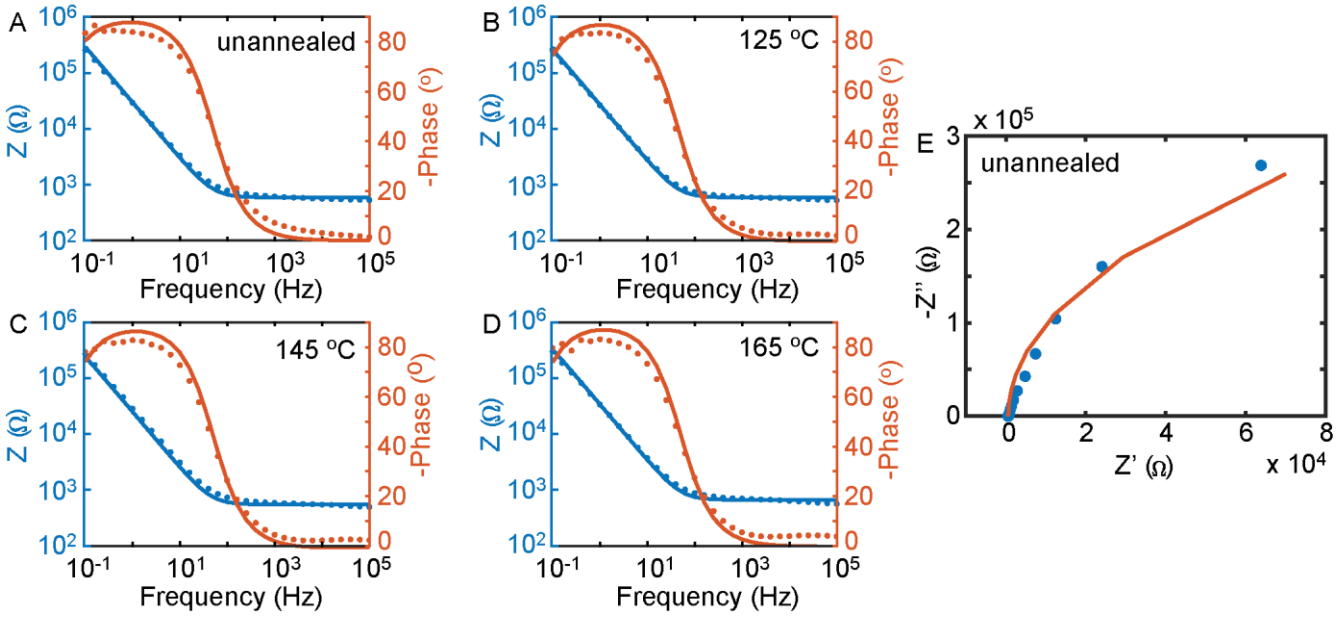

Figure B.18: Determination of C* of P3MEEMT for each annealing temperature. Bode plots of (A) unannealed, (B) 125 °C, (C) 145 °C, and (D) 165 °C, using electrochemical impedance spectroscopy (EIS). (E) Example Nyquist plot and fit for unannealed P3MEEMT.

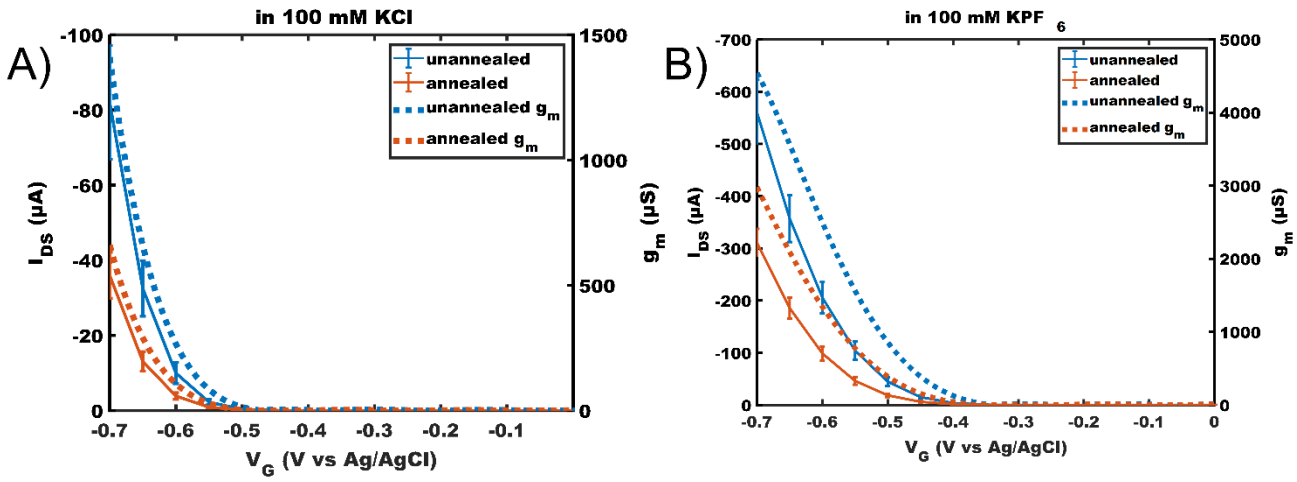

Figure B.19: Comparison of unannealed and annealed films on glass substrates (A) in 100 mM KCl showing that the current and transconductance (g_m) decrease with annealing on glass substrates in both electrolytes. (B) Comparison of unannealed and annealed films on glass substrates in 100 mM KPF_6 showing the trend of lower current and g_m in the annealed film. Error bars are one standard deviation of 6 devices.

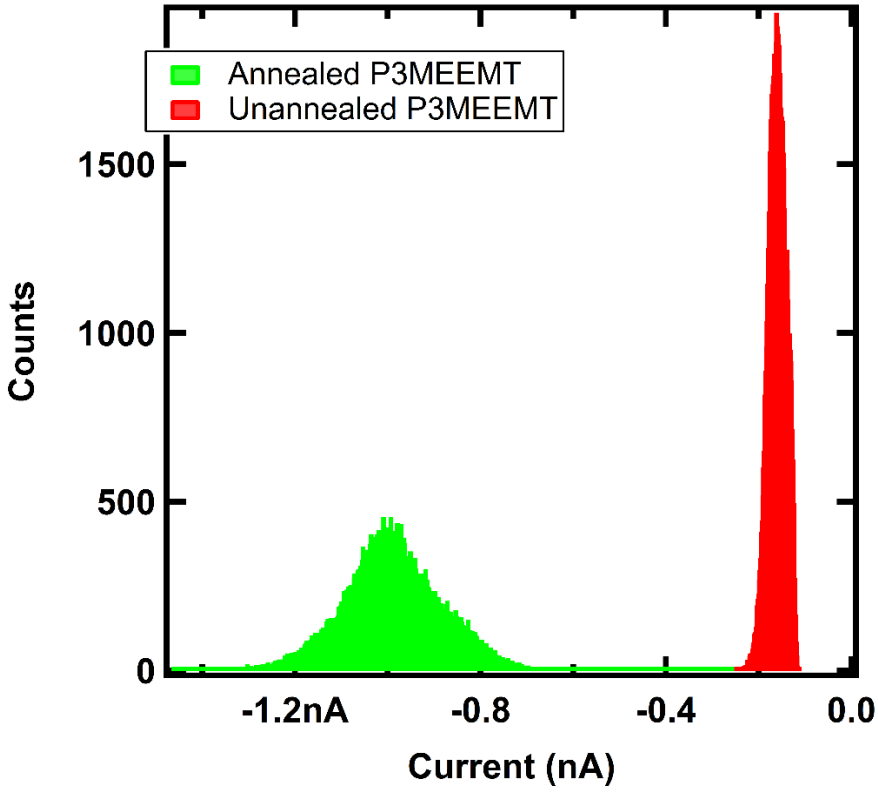

Figure B.20: Histogram of conductive AFM scans of a 2 x 2 µm area with -500 mV applied to the tip on an unannealed (red) and an annealed (green) P3MEEMT film showing higher conductivity in the annealed film.

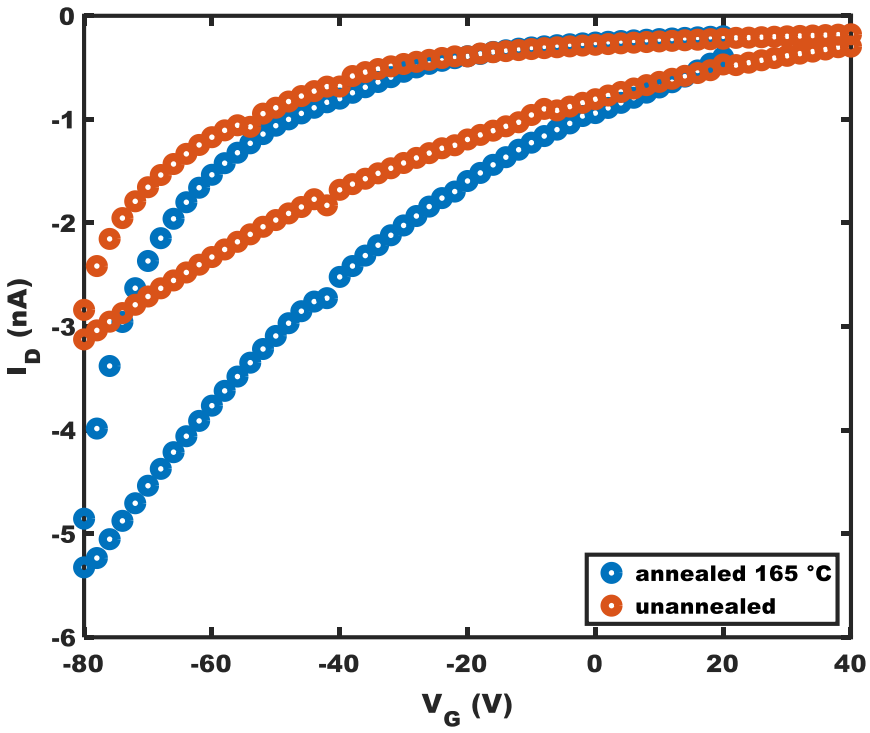

Figure B.21: Organic field effect transistor (OFET) measurements of P3MEEMT-based OFETs annealed and unannealed showing increased current and transconductance in the annealed film.

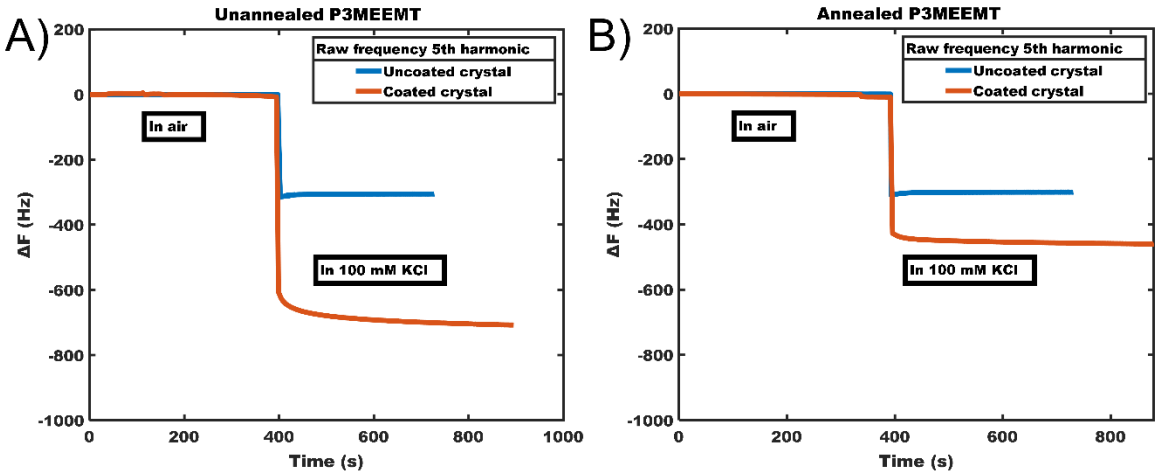

Figure B.22: A) QCM-D data showing the frequency of the bare crystal and the polymer coated crystal in air and submerged in 100 mM KCl. B) The same data for the annealed film showing significantly less water uptake in than in the unannealed case.

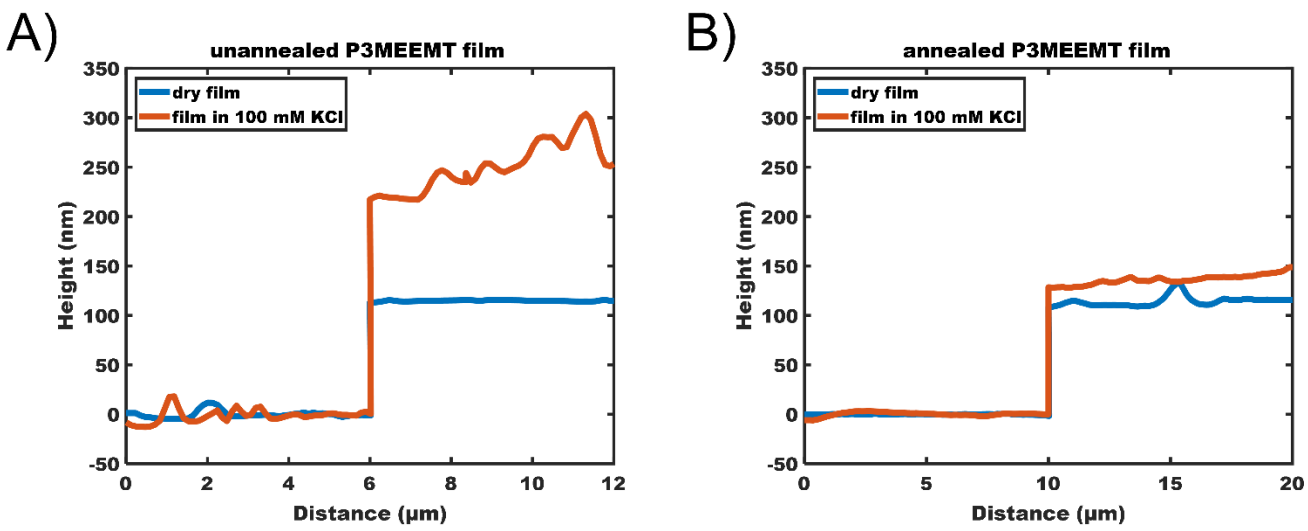

Figure B.23: Representative atomic force microscopy (AFM) profiles of (a) unannealed P3MEEMT dry and hydrated in 100 mM KCl. Averages over 6 samples show an average swelling of 105% ± 30%. (B) Representative AFM profiles of a P3MEEMT film annealed at 165 °C for 20 minutes dry and hydrated in 100 mM KCl. Averages over 6 samples show an average swelling of 22% ± 13 %.

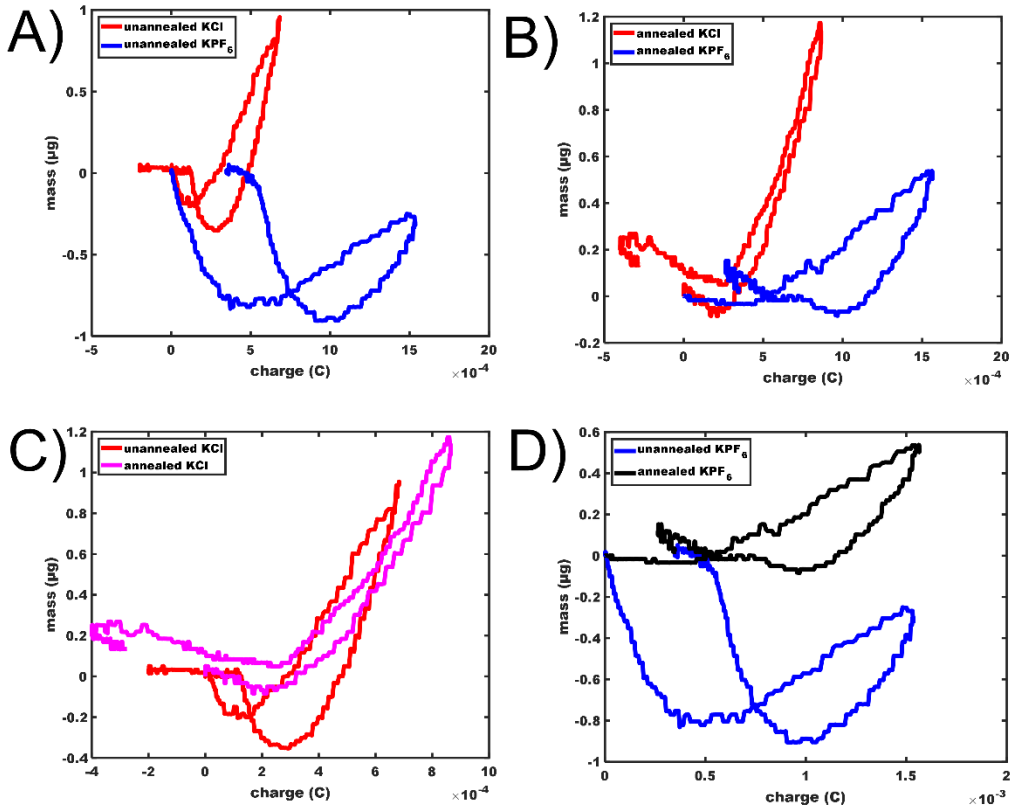

	Apparent Mass of Dopant (g/mol)	Hydration shell (# of waters)
Unannealed film KCl	223.2 ± 13.4	10.4 ± 0.7
Annealed film KCl	231.3 ± 12.1	10.9 ± 0.7
Unannealed film KFP_6	63.5 ± 3.2	- 4.5 ± 0.2
Annealed film in KFP_6	56.0 ± 3.8	- 4.9 ± 0.2

Figure B.24: Mass versus Q plots used to find the molecular mass of the injected ion as previously described.[4] Comparison of the KCl and KPF_6 in the unannealed (A) and annealed (B) film showing a heavier molar mass of the dopant in KCl than in KPF_6. (C) Comparison of the annealed and unannealed film in KCl showing similar slope in the mass gain region but significantly more water expulsion in the unannealed case. (D) Same data taken in KPF_6, showing much more water expulsion from the unannealed film than the annealed film. (E) Summary table where the apparent molar mass of the dopant is extracted from the slope in the mass increase region and the error bars are the standard deviation of the slope of 9 cycles.

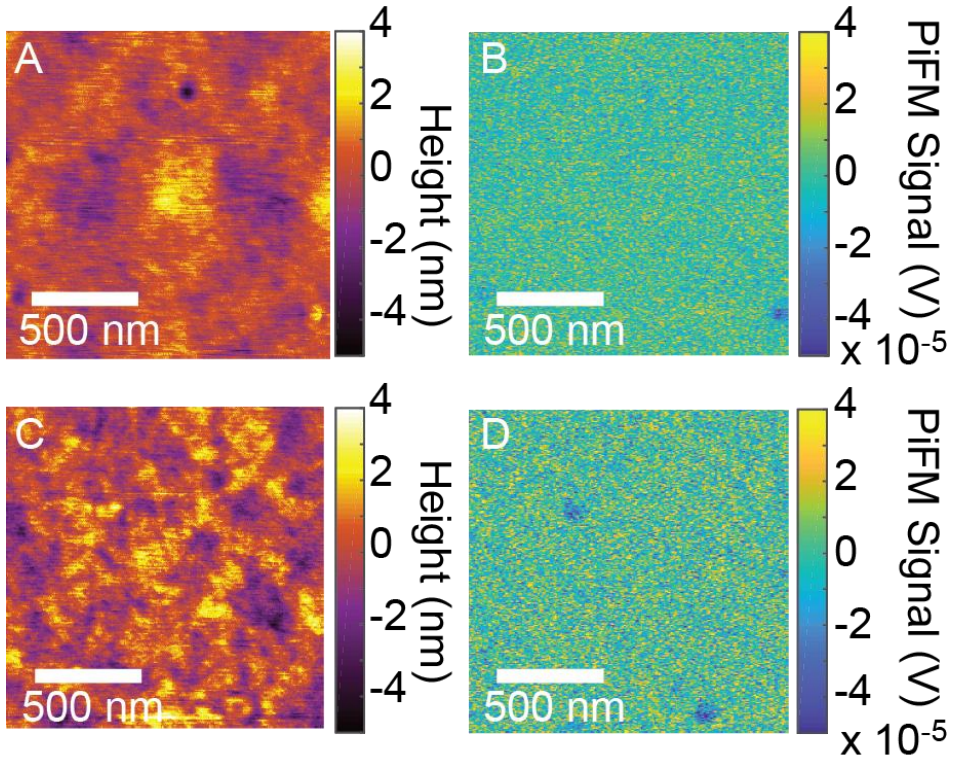

Figure B.25: PiFM image of an undoped region of P3MEEMT and corresponding topography image. (A) Topography of unannealed P3MEEMT. (B) Flattened PiFM image of unannealed P3MEEMT. (C) Topography of annealed P3MEEMT. (D) Flattened PiFM image of unannealed P3MEEMT.

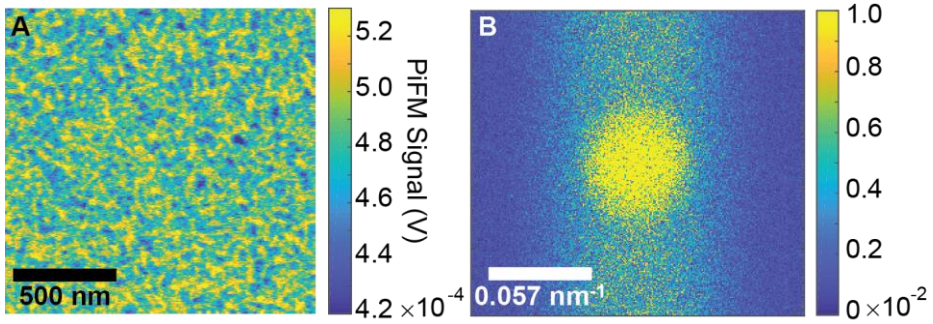

Figure B.26: (A) Original PiFM image of P3MEEMT doped with PF_6^- collected at 843 cm^{-1}. (B) Fourier analysis of the PiFM image showing characteristic length scale of anion heterogeneity of ~40 nm.

References:

(1) Lee, E.; Hammer, B.; Kim, J.-K.; Page, Z.; Emrick, T.; Haywar, R. C. Hierarchical Helical Assembly of Conjugated Poly(3-Hexylthiophene)- Block-Poly(3-Triethylene Glycol Thiophene) Diblock Copolymers. *J. Am. Chem. Soc.* **2011**, *133*, 10390–10393.

(2) Rivnay, J.; Ramuz, M.; Leleux, P.; Hama, A.; Huerta, M.; Owens, R. M. Organic Electrochemical Transistors for Cell-Based Impedance Sensing. *Appl. Phys. Lett.* **2015**, *106*.

(3) Rivnay, J.; Inal, S.; Collins, B. A.; Sessolo, M.; Stavrinidou, E.; Strakosas, X.; Tassone, C.; Delongchamp, D. M.; Malliaras, G. G. Structural Control of Mixed Ionic and Electronic Transport in Conducting Polymers. *Nat. Commun.* **2016**, *7*, 11287.

(4) Zhang, L.; Andrew, T. L. Deposition Dependent Ion Transport in Doped Conjugated Polymer Films: Insights for Creating High-Performance Electrochemical Devices. *Adv. Mater. Interfaces* **2017**, *4*, 1700873.

APPENDIX C.

Appendix C accompanies Chapter 4: P-Type Electrochemical Doping Can Occur by Cation Expulsion in a High Performing Polymer for Organic Electrochemical Transistors

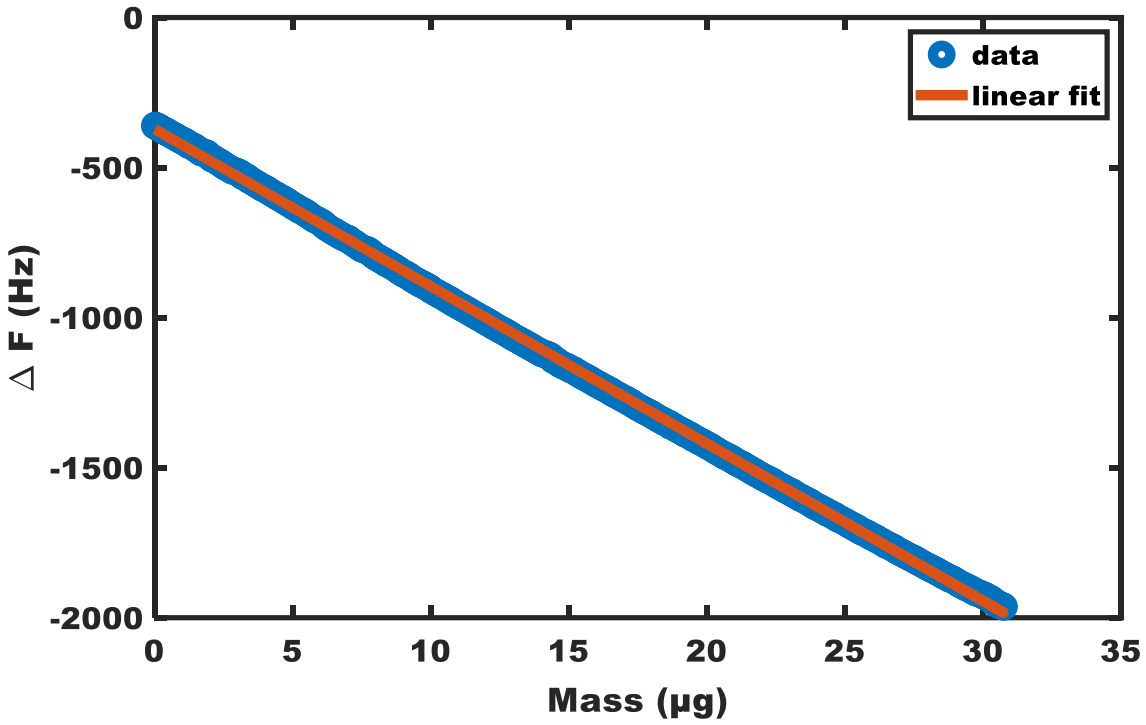

Figure C.1: EQCM calibration. We use the electrodeposition of Ag (50 mM $AgNO_3$ in 0.5 M HNO_3) at a constant current of 40 μA to calibrate the sensitivity factor (C_f) and active area of the EQCM as described in the literature.[6]

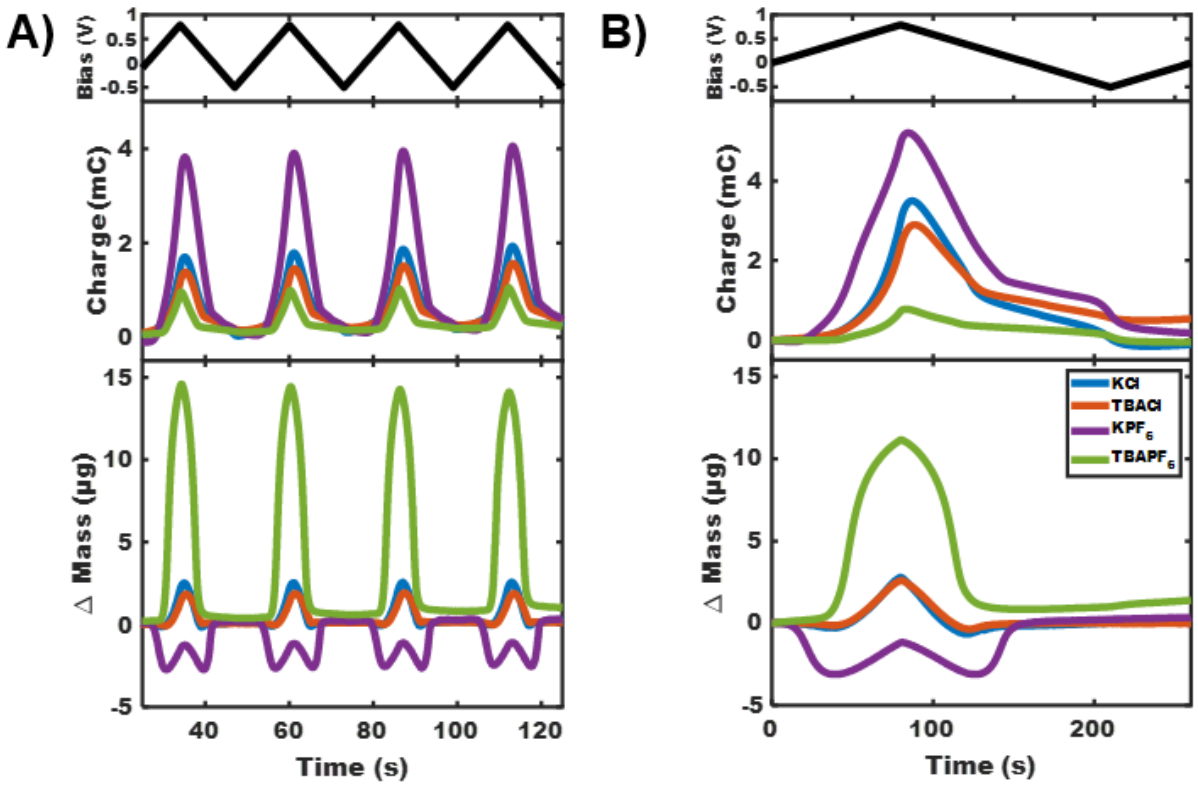

Figure C.2: Repeated scans at different bias sweep rates in 4 different electrolytes. A) Shows the bias, charge, and change in mass as a function of time over 4 cycles at a bias sweep rate of 100 mV/s. The oxidation/reduction cycle is reversible in all electrolytes shown. B) Shows the bias, charge, and change in mass in 4 different salts data during a 10 mV/s scan.

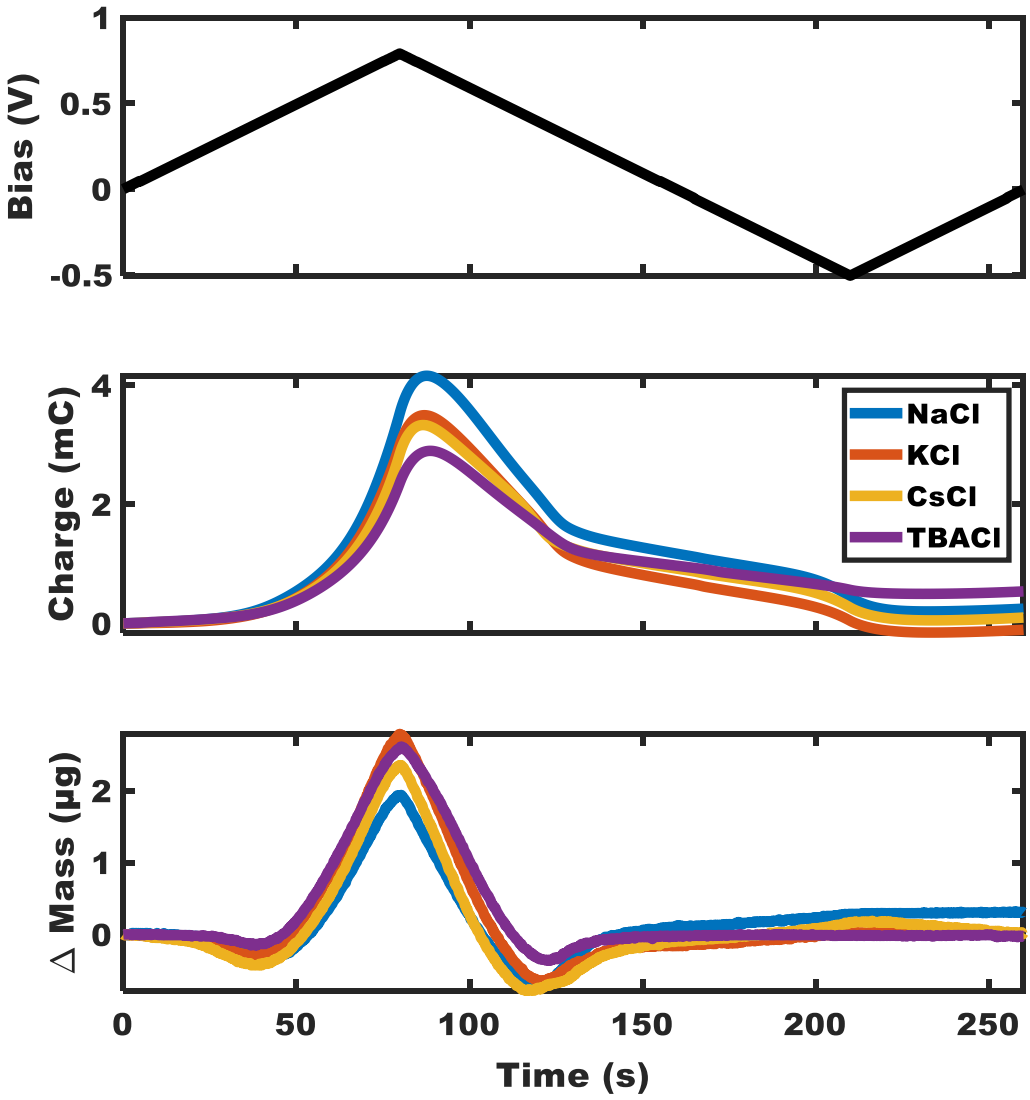

Figure C.3: EQCM data including two additional chloride salts (NaCl and CsCl) showing qualitative agreement between all 4 chloride salts tested.

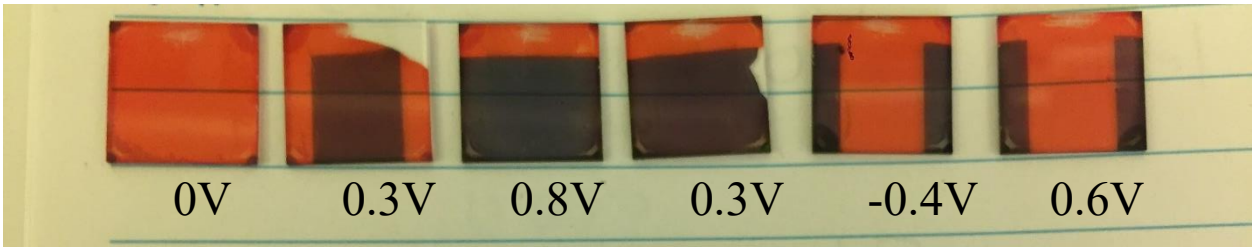

Figure C.4: Optical images of a series of polymer films on patterned ITO substrates removed from the electrolyte at different stages of oxidation and rinsed.

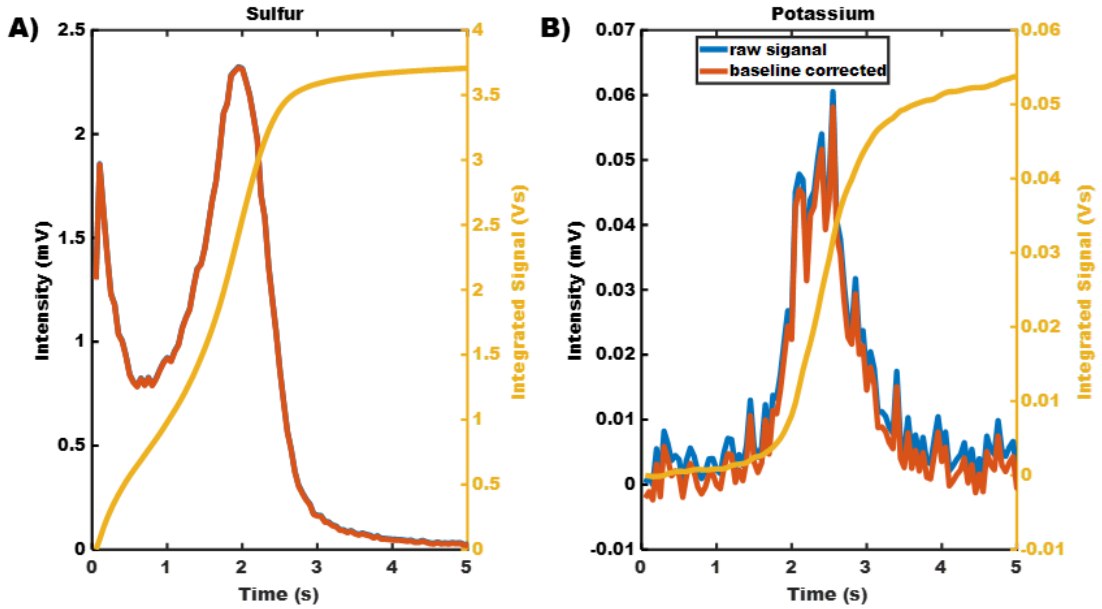

Figure C.5: Illustration of the normalization procedure used. A) Shows an example of the raw sulfur signal (blue) and the baseline corrected signal in orange on the left axis. The right axis shows the total integrated signal (yellow). B) Shows an example of the raw potassium signal (blue), the baseline corrected signal (orange), and the total integrated signal on the right axis (yellow).

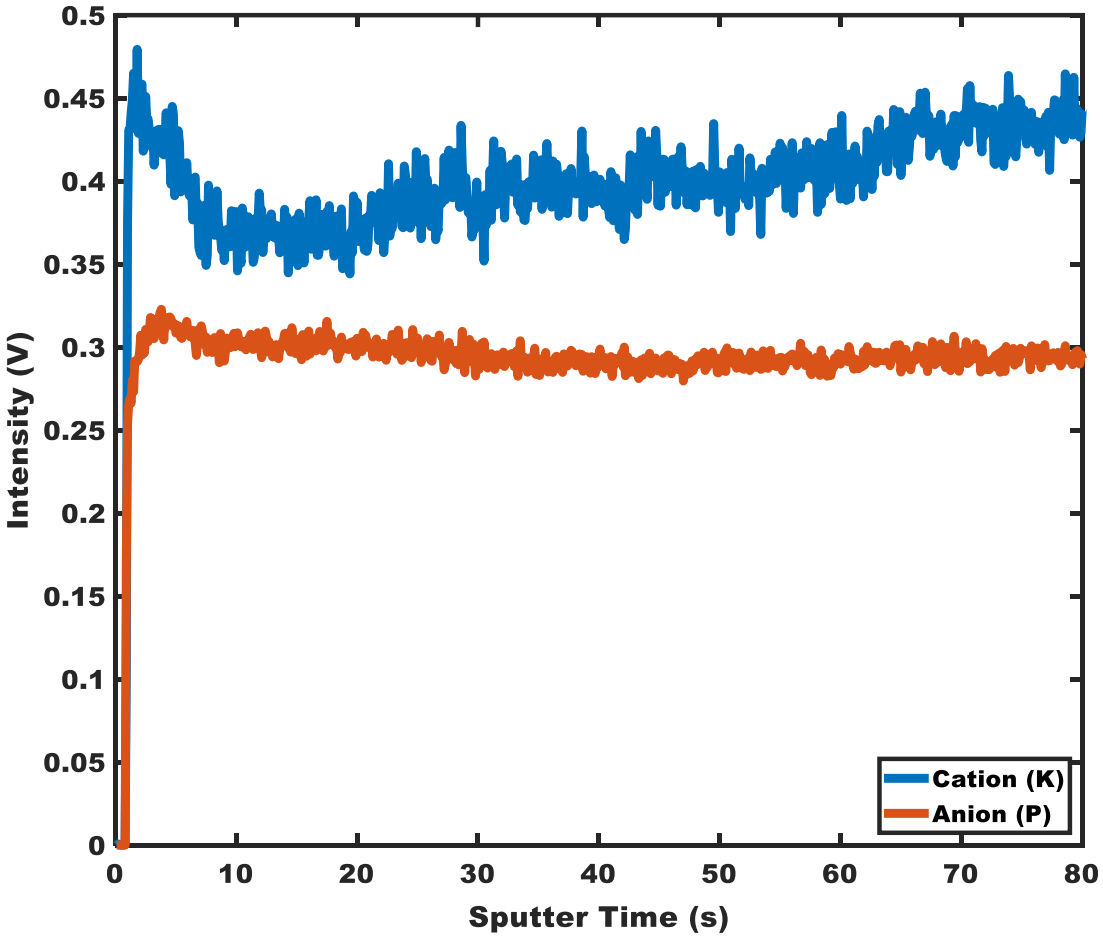

Figure C.6: Calibration of the GDOES signal. We dry 100 mM KPF_6 salt on a glass substrate which presumably results in a 1:1 ratio of potassium to phosphorus. The data shows that the potassium signal is stronger than the phosphorus signal when there are equal amounts of each element. This difference in instrumental sensitivity to the potassium and phosphorus signals indicates that only relative changes are meaningful.

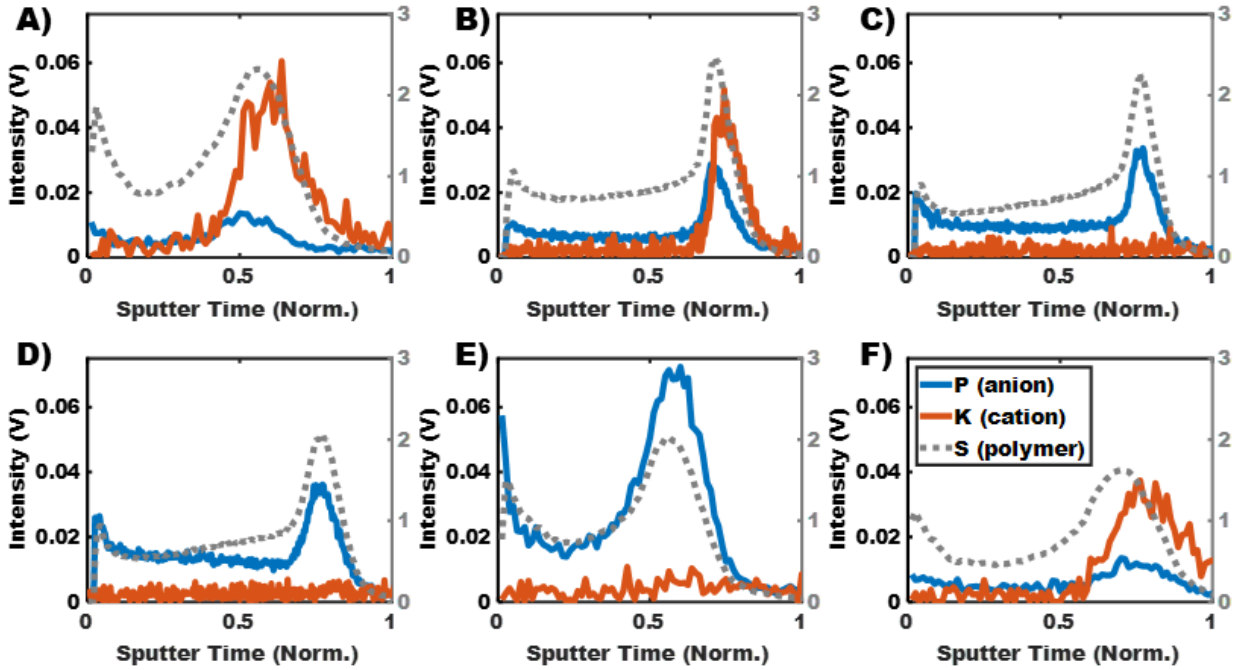

Figure C.7: Raw GDOES Spectra at 6 different oxidation states**.** For all spectra the phosphorus (anion) signal is plotted in blue and the potassium signal (cation) is plotted in orange against the left axis. On the right axis is gray is the sulfur content provided as a reference for the variation in etch rate. A) shows the GDOES spectra at 0 V after the sample is submerged in KPF_6 for 30 seconds. B) shows the GDOES spectra of a sample doped at 300 mV. C) shows the GDOES spectra of a sample doped t 400 mV. D) shows the GDOES spectra of a sample doped at 500 mV. E) shows the GDOES spectra of a sample doped at 700 mV. F) shows the GDEOS spectra at 0 V after completing one full bias cycle.

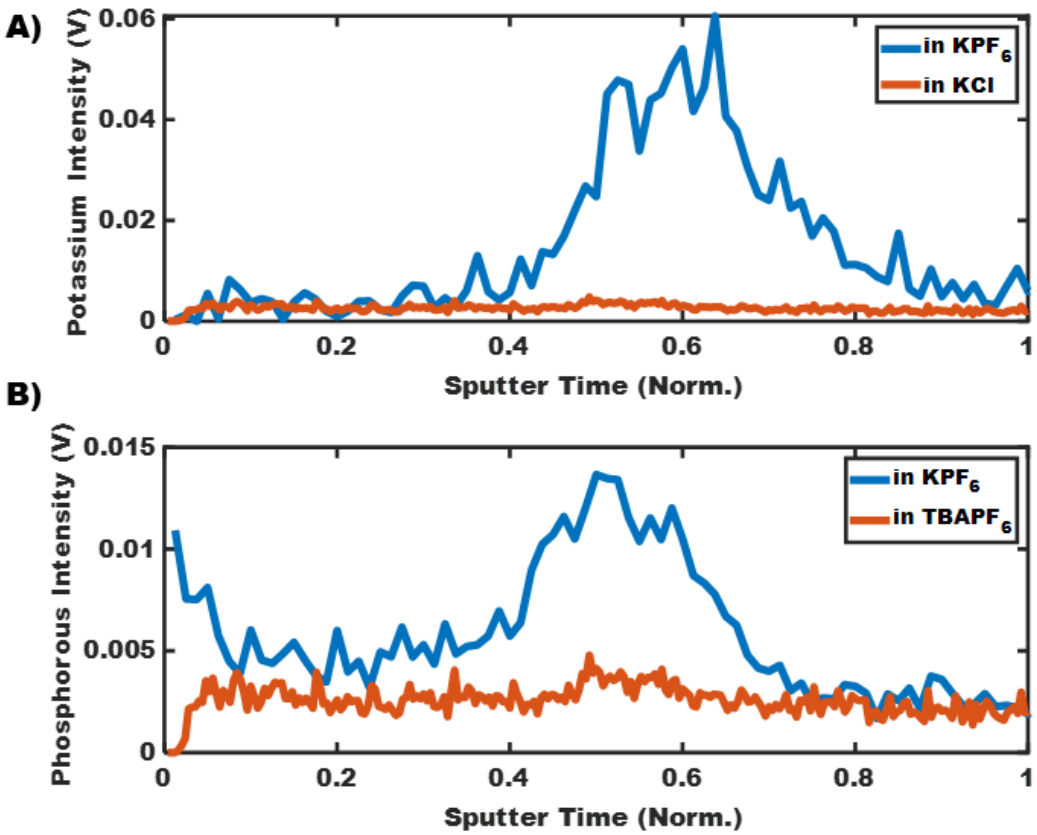

Figure C.8: GDOES in other salts. A) Shows the potassium signal of a film dipped in KPF_6 (blue) and in KCl (orange). The orange trace shows that when chloride is the anion we do not detect any cation in the film. B) Shows the phosphorous signal of a film dipped in KPF_6 (blue) and $TBAPF_6$ (orange). The orange trace shows that when TBA is the cation, we do not detect any anion within the film.

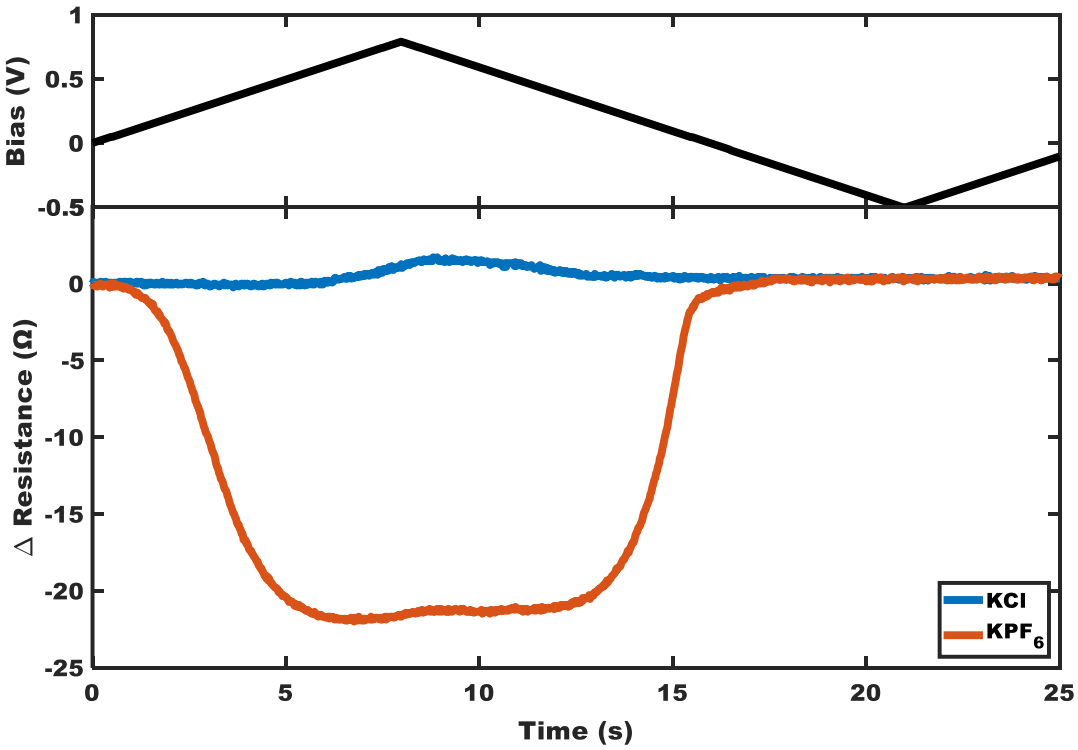

Figure C.9: Change in film stiffness. Here we plot the series resonance resistance of the quartz oscillator during a cyclic voltammetry scan in KCl (blue) and in KPF_6 (orange). An increase in the resistance corresponds to a softer film and a decrease indicates the film is getting stiffer. When doped in KCl the film gets softer by 2 Ω, likely due to the inclusion of water.[7] When the film is oxidized in KPF_6, the film gets stiffer by 22 Ω, suggesting the expulsion of water.

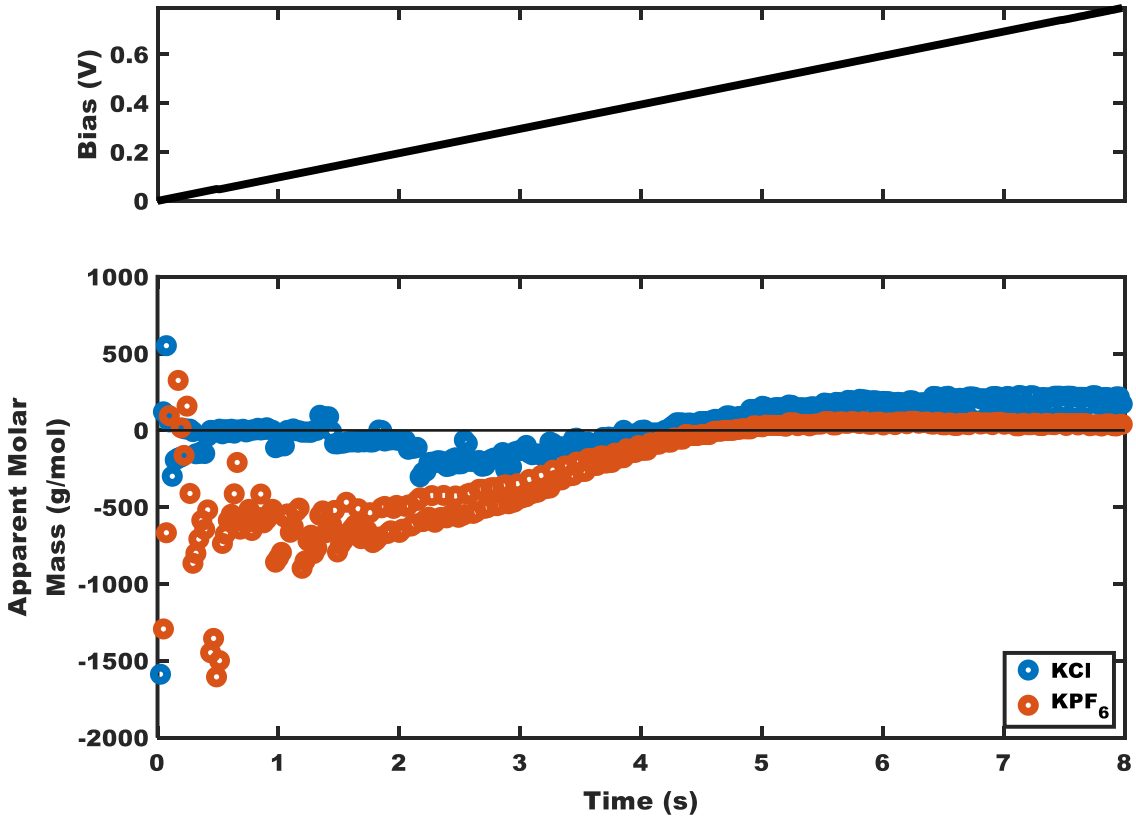

Figure C.10: Molar mass per injected charge. At the low doping levels, the magnitude of the apparent molar mass of the dopant species is significantly greater in KPF_6 (orange) than in KCl (blue) implying that there is more solvent expulsion occurring in the KPF_6 electrolyte.

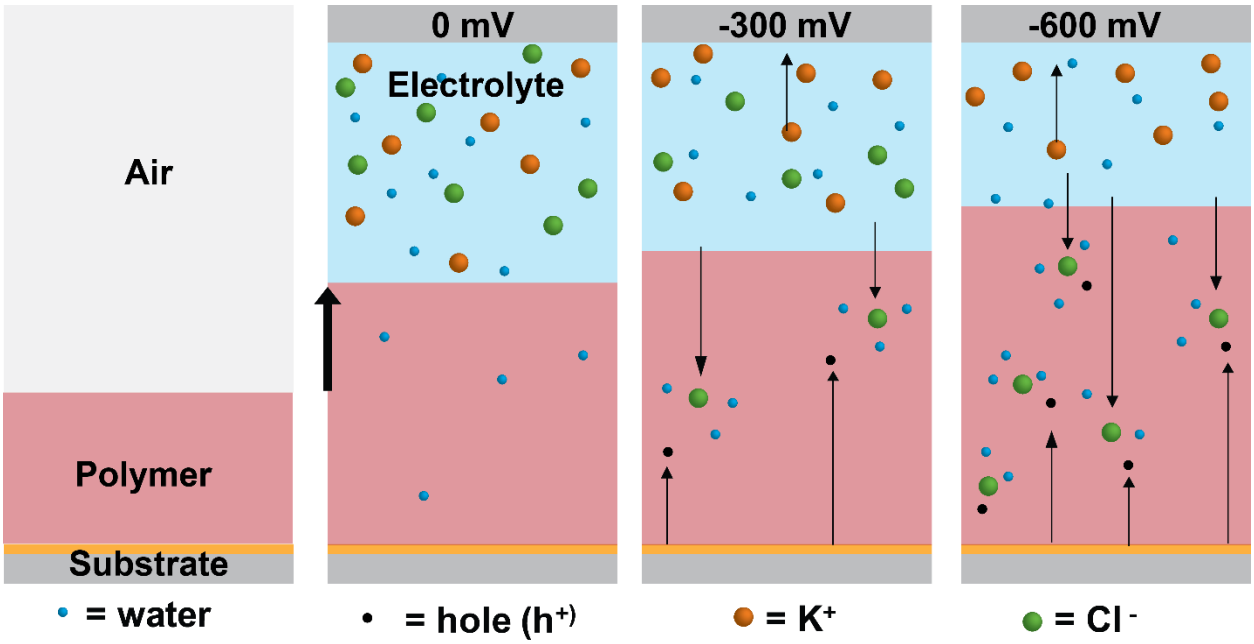

Figure C.11: Schematic of doping in KCl. In KCl we believe there is very little cation/anion content in the film prior to bias. Therefore, all levels of oxidation result in anion injection into the film.

References:

(1) Lee, E.; Hammer, B.; Kim, J.-K.; Page, Z.; Emrick, T.; Haywar, R. C. Hierarchical Helical Assembly of Conjugated Poly(3-Hexylthiophene)- Block-Poly(3-Triethylene Glycol Thiophene) Diblock Copolymers. *J. Am. Chem. Soc.* **2011**, *133*, 10390–10393.

(2) Zhang, L.; Andrew, T. L. Deposition Dependent Ion Transport in Doped Conjugated Polymer Films: Insights for Creating High-Performance Electrochemical Devices. *Adv. Mater. Interfaces* **2017**, *4*, 1700873.

(3) Hillman, A.; Daisley, S. J. S.; Bruckenstein, S.; Robert Hillman, A.; Daisley, S. J. S.; Bruckenstein, S. Solvent Effects on the Electrochemical P-Doping of PEDOT. *Phys. Chem. Chem. Phys.* **2007**, *9*, 2379–2388.

(4) Hillman, A. R.; Daisley, S. J.; Bruckenstein, S. Kinetics and Mechanism of the Electrochemical P-Doping of PEDOT. *Electrochem. commun.* **2007**, *9*, 1316–1322.

(5) Hillman, A. R.; Daisley, S. J.; Bruckenstein, S. Ion and Solvent Transfers and Trapping Phenomena during N-Doping of PEDOT Films. *Electrochim. Acta* **2008**, *53*, 3763–3771.

(6) Gabrielli, C. Calibration of the Electrochemical Quartz Crystal Microbalance. *J. Electrochem. Soc.* **1991**, *138*, 2657.

(7) Flagg, L. Q.; Bischak, C. G.; Onorato, J. W.; Rashid, R. B.; Luscombe, C. K.; Ginger, D. S. Polymer Crystallinity Controls Water Uptake in Glycol Side-Chain Polymer Organic Electrochemical Transistors. *J. Am. Chem. Soc.* **2019**, *141*, 4345–4354.

VITA

EDUCATION

2019 Ph.D. Chemistry – University of Washington

Advisor: Prof. David S. Ginger

2014 B.S. Engineering Physics/Chemistry – Santa Clara University

Advisor: Prof. John T. Birmingham

PUBLICATIONS

10) **L. Q. Flagg,** C. G. Bischak, J. W. Onorato, R. B. Rashid, C. K. Luscombe, D. S. Ginger. Electrochemical Doping Occurs by Cation Expulsion in a High Performing Polymer for Organic Electrochemical Transistors. Submitted.

9) C. G. Bischak, **L. Q. Flagg,** K. Yan, T. Rehman, R. J. Quezada, J. W. Onorato, C. K. Luscombe, Y. Diao, C. Z. Li, D. S. Ginger. "A Reversible Structural Phase Transition By Electrochemical Ion Injection into a Conjugated Polymer." Submitted. (Preprint arXiv:1910.06440v1)

8) C. G. Bischak, **L. Q. Flagg,** D. S. Ginger. "Ion Exchange Gels Enhance Organic Electrochemical Transistor Performance in Aqueous Solution." Submitted. (Preprint arXiv:1909.13397)

7) C. G. Bischak, **L. Q. Flagg,** K. Yan, C. Z. Li, D. S. Ginger. Fullerene Active Layers for N-Type Organic Electrochemical Transistors. *ACS Applied Materials & Interfaces*. (2019) 11, 28138-28144. DOI: 10.1021/acsami.9b11370

6) W. Tatum, A. Resing, **L. Q. Flagg,** D. S. Ginger, C. K. Luscombe. Defect Tolerance of π-Conjugated Polymer Crystal Lattices and Their Relevance to Optoelectronic Applications. *ACS Applied Polymer Materials*. (2019) 1, 1466-1475. DOI:10.1021/acsapm.9b00223

5) **L. Q. Flagg,** C. G. Bischak, J. W. Onorato, R. B. Rashid, C. K. Luscombe, D. S. Ginger. Polymer Crystallinity Controls Water Uptake in Glycol Side-Chain Polymer Organic Electrochemical Transistors. *Journal of the American Chemical Society.* (2019) 141, 4345–4354. DOI:10.1021/jacs.8b12640

4) **L. Q. Flagg**, R. Giridharagopal, J. Guo, D. S. Ginger. Anion-Dependent Doping and Charge Transport in Organic Electrochemical Transistors. *Chemistry of Materials.* (2018) 30, 5380-5389. DOI:10.1021/acs.chemmater.8b02220

3) R. Giridharagopal, **L. Q. Flagg,** J. S. Harrison, M. E. Ziffer, J. W. Onorato, C. K. Luscombe, D. S. Ginger. Electrochemical Strain Microscopy Probes Morphology-Induced Variations in Ion Uptake and Performance in Organic Electrochemical Transistors. *Nature Materials.* (2017) 16, 737−742. DOI:10.1038/NMAT4918

2) P. A. Cox, **L. Q. Flagg,** R. Giridharagopal, D. S. Ginger. Cantilever Ringdown Dissipation Imaging for the Study of Loss Processes in Polymer/Fullerene Solar Cells. *The Journal of Physical Chemistry C.* (2016) 120, 12369– 12376. DOI:10.1021/acs.jpcc.6b03160

1) B. N. Ralston, **L. Q. Flagg,** E. Faggin, J. T. Birmingham. Incorporating Spike-Rate Adaptation into a Rate Code in Mathematical and Biological Neurons. *Journal of Neurophysiology*. (2016) 115, 2501-2518. DOI:10.1152/jn.00993.2015

AWARDS AND HONORS

NIST NRC Postdoctoral Research Associateship	2019
Travel Award, Clean Energy Institute	2019
Nominee, 2019 Schmidt Science Fellowship	2019
Best Poster Presentation at Asilomar Bioelectronics Symposia	2018
Travel Award, Clean Energy Institute	2018
Torrance Tech Due Diligence Fellow	2017
Clean Energy Institute Graduate Fellow	2016
ACS Award in Inorganic Chemistry	2014
Inducted into the National Physics Honors Society, Sigma Pi Sigma	2014
Santa Clara University Hayes Fellowship	2012
Presidential Merit Scholarship for academic performances Santa Clara University	2010